

מכון ויצמן למדע

WEIZMANN INSTITUTE OF SCIENCE



## Multiscale representation of very large environments in the hippocampus of flying bats

### Document Version:

Accepted author manuscript (peer-reviewed)

### Citation for published version:

Eliav, T, Maimon, SR, Aljadeff, J, Tsodyks, M, Ginosar, G, Las, L & Ulanovsky, N 2021, 'Multiscale representation of very large environments in the hippocampus of flying bats', *Science (American Association for the Advancement of Science)*, vol. 372, no. 6545, eabg4020.  
<<https://10.1126/science.abg4020>>

Total number of authors:

7

### Published In:

Science (American Association for the Advancement of Science)

### License:

Other

### General rights

@ 2020 This manuscript version is made available under the above license via The Weizmann Institute of Science Open Access Collection is retained by the author(s) and / or other copyright owners and it is a condition of accessing these publications that users recognize and abide by the legal requirements associated with these rights.

### How does open access to this work benefit you?

Let us know @ [library@weizmann.ac.il](mailto:library@weizmann.ac.il)

### Take down policy

The Weizmann Institute of Science has made every reasonable effort to ensure that Weizmann Institute of Science content complies with copyright restrictions. If you believe that the public display of this file breaches copyright please contact [library@weizmann.ac.il](mailto:library@weizmann.ac.il) providing details, and we will remove access to the work immediately and investigate your claim.

**Multi-scale representation of very large environments  
in the hippocampus of flying bats**

Tamir Eliav<sup>1\*</sup>, Shir R. Maimon<sup>1\*</sup>, Johnatan Aljadeff<sup>ff1,2</sup>, Misha Tsodyks<sup>1,3</sup>, Gily Ginosar<sup>1</sup>, Liora Las<sup>1</sup>,  
Nachum Ulanovsky<sup>1†</sup>

1. Department of Neurobiology, Weizmann Institute of Science, Rehovot 76100, Israel
2. Section of Neurobiology, Division of Biological Sciences, University of California San Diego, CA 92093, USA
3. The Simons Center for Systems Biology, Institute for Advanced Study, Princeton, New Jersey 08540, USA

**One-sentence summary:** We recorded hippocampal CA1 place-cells from bats flying in a very large-scale environment (200 meters), and found a multi-scale representation of this space – whereby neurons exhibited multiple fields, and the fields of the *same* neuron differed by up to 20-fold in size; a theoretical analysis showed that such multi-scale coding increases the capacity of the system to represent large spaces and reduces the decoding errors.

\* These authors contributed equally to this work

† Corresponding author. Email: nachum.ulanovsky@weizmann.ac.il

Hippocampal place-cells encode the animal's location. **Place-cells were traditionally studied in small environments**, and nothing is known about **large** ethologically-relevant spatial scales. We wirelessly recorded **from** hippocampal dorsal-CA1 neurons of wild-born bats flying in a long tunnel (200-meters). The size of place-fields ranged from 0.6-m to 32-m. **Individual place-cells** exhibited multiple fields, and a multi-scale representation: place-fields of the *same* neuron differed up to 20-fold in size. This multi-scale coding was observed from the first **exposure-day** to the environment, **and also** in lab-born bats that never experienced large environments. Theoretical decoding-analysis showed that the multi-scale code allows representing very large environments with much higher precision than other codes. **Together, by increasing the spatial-scale we discovered a neural code that is radically different from classical place-codes.**

Navigation and spatial memory are crucial for the survival of animals in the wild. The hippocampal formation contains several types of spatial neurons whose activity represents the animal's position and direction in space (1-10). One of these spatial cell types are 'place cells' – hippocampal neurons that increase their spiking activity when the animal passes through a specific region of space – called the neuron's 'place field' (1, 2, 11-15). Individual place-cells typically have only one (or two) place-fields in a small environment (2, 11, 16), while multiple place-fields are found in dentate-gyrus neurons upstream (16). Nearly all the research on spatial representations in the mammalian brain has focused on rats and mice as animal models, and used small laboratory environments as experimental setups – usually small boxes or short linear tracks ~1–2 m in size. Consequently, almost all current knowledge on spatial neurons in the hippocampal formation is based on data from animals moving in small laboratory environments. Two studies of place cells examined larger spatial scales (17, 18). However, these studies used either a zig-zagging track composed of ~1 m segments, or a track that passed through several small rooms: thus, the largest single-compartment environment in which place-cells were recorded to date was < 10 m in size.

By contrast, outdoor navigation of all mammals occurs in natural environments that span spatial scales much larger than 10 m: For example, wild rats were shown to navigate outdoors >1 km per night (19, 20). Navigation over such distances requires spatial representation of very large environments, on the scale of hundreds of meters or kilometers (21). Egyptian fruit bats fly every night distances of up to ~30 km to their favorite fruit trees, with flyways spanning ~2 km width and 0.5 km height (21, 22). A simple calculation shows that tiling this space with typical place-fields as measured in the laboratory (~10–20 cm diameter, single field per-neuron) would require ~10<sup>13</sup> neurons. This is ~10<sup>8</sup> times more neurons than the number of cells in the entire dorsal hippocampal area CA1 (3) – suggesting that it is simply not feasible to represent such large



spatial scales with laboratory-sized place fields. Thus, there is a fundamental gap between the neurobiology of navigation as studied in the lab, and kilometer-scale natural navigation outdoors.

### **Neural recordings in bats flying in a 200 m environment**

We studied *wild*-born Egyptian fruit bats, a **mammal** which has rodent-like hippocampal spatial representations in small laboratory environments (23-26). We developed a miniaturized wireless neural-logging system that stores all the data on-board (Fig. 1A). This system enabled neural recordings to be conducted over great distances in freely-behaving animals – with uninterrupted experiments lasting up to ~3 hours (27). Using this system, we conducted tetrode recordings from dorsal CA1, in flight (Fig. 1B-D and fig. S1). We built a 200 meter long flight tunnel (Fig. 1E), composed of a long arm and a shorter arm, with landmarks dispersed along it (fig. S2). We employed a medium light level (5 lux), allowing these bats – **which have excellent vision (21)** – to see several distal landmarks from each location in the tunnel (fig. S2B). We used a radio-frequency-based localization system, **with a small mobile tag placed on the bat**, which measured the bat's distances to a ground-based antenna array (Fig. 1F). This system yielded a high spatial localization accuracy of ~9 cm (Fig. 1G) – along with a high temporal resolution (27). We **harnessed the natural behavioral tendency of bats to fly long distances in straight trajectories (22)**, and trained them to fly in the tunnel between two landing-balls that were placed at the two ends of the tunnel, on which food was given. The bats flew continuously back-and-forth between the landing-balls (fig. S3A). Flight trajectories were rather stereotyped, with bats flying at the center-top portion of the tunnel, with only very small deviations perpendicular to the flight direction (Fig. 1H and fig. S3B-C). Thus, the bats exhibited nearly-perfect one-dimensional (1D) back-and-forth trajectories. Hence, in all subsequent analyses we projected the behavioral data onto the main axis of the tunnel, and included only long unidirectional

flights with >100 m length (27). We note that this 1D tunnel bears similarities to bats' natural behaviors – as these bats navigate underground in 1D cave-tunnels, and also their flight trajectories outdoors are largely 1D (22). Flight-speed was high and showed very little variation across different locations (Fig. 1I,J). Bats flew dozens of flights per direction in each recording session (Fig. 1K), covering on average 14.1 km per session, and up to 22.5 km in a single session (Fig. 1L).

### **Hippocampal place-cells exhibit a multi-field multi-scale spatial code**

We recorded 235 well-isolated putative pyramidal cells from dorsal CA1 of 5 bats; all 235 neurons were active in-flight, and 83.4% of them ( $n=196$ ) were place-cells, showing significant spatial tuning with distinct and stable place-fields (Fig. 2A, and figs. S4 and S5; see Table S1 for the numbers of place-cells in individual bats) (27). By contrast, in both rodents and bats, the reported percentage of place-cells in small environments is typically 30–40% of all the recorded cells, while the remaining cells are virtually silent during behavior (11, 23, 24, 28). Place cells in the 200-m tunnel exhibited strong spatial tuning (Fig. 2B-D) – and the spatial tuning was stable across flights (Fig. 2E). The place-cells fired differently in different flight directions (Fig. 2A, compare red and blue raster-plots; and see Fig. 2F for map correlations between directions) – similar to the directionality shown previously for place-cells in rats and bats in small 1D environments (29, 30). However, we found several surprising characteristics of place-cell firing in our 200 m environment. First, unlike the typical single place-field reported for CA1 neurons in small environments (11), we found that many cells exhibited multiple place-fields (Fig. 2A and fig. S5 – examples; Fig. 2G – population). The mean number of fields per direction was 4.9, and some neurons had more than 10 fields in each flight-direction (Fig. 2G). This result extends similar findings in enlarged environments in rodents, which showed several fields per neuron (18,

31, 32). The fields were strongly tuned and contained the large majority of the neuron's spikes, i.e. the background firing was relatively low (fig. S6A-B). Second, many cells had very large place-fields, often > 10 m in size, and up to 32 m (Fig. 2A cells 1 and 5 – examples; Fig. 2H – population; see also figs. S5 and S7A). On the other hand, some cells had very small place-fields < 1 m in size, and down to 0.6 m (Fig. 2A cells 3 and 7, see zoom-in; and Fig. 2H, leftmost bar). The distribution of field sizes was skewed (Fig. 2H) and was well-fitted by a log-normal distribution (fig. S8) (33). Third, and most surprisingly, many place-cells showed highly variable fields sizes, with up to 20-fold ratio between the size of the largest/smallest field for the *same* neuron (Fig. 2A cells 1–7 – examples; and Fig. 2I,J – population; mean ratio: 4.4). This multi-field multi-scale code was found in all the 5 individual animals (fig. S9). Although most cells showed heterogeneous field sizes, some neurons also exhibited a more uniform scale across their place-fields (Fig. 2A, cell 8), and a small minority of neurons had a single place-field (Fig. 2A, cell 9; only 12.2% of the neurons had one field overall, **with average field-size of  $5.9 \pm 3.5$  m; mean  $\pm$  s.d.**). Individual neurons exhibited similar multi-scale firing properties in both flight-directions: a similar number of fields per direction, similar median field-size, and similar field size ratios (fig. S10); **this suggests a characteristic firing-propensity per neuron (34) – while still exhibiting widely-varying field sizes.** Taken together, most neurons exhibited these two key properties: many fields per neuron (Fig. 2G), and a multi-scale mixture of small fields and large fields for the *same* neuron (Fig. 2J).

We next examined several possible alternative explanations for the multi-scale code that we observed. First, the multi-scale property could not be explained as arising from variations in flight-speed – **e.g. larger fields at high flight-speeds** – because the flight-speed was in fact highly-consistent along the entire tunnel (Fig. 1I,J). Further, the field-size ratio (largest/smallest fields

per neuron) was not correlated with the speed ratio at the locations of the largest and smallest fields (Fig. 2K: Spearman  $\rho=0.03$ ,  $df=170$ ,  $P=0.67$ ). Moreover, the speed ratio was narrowly distributed around 1, indicating that the speed was similar at large and small fields (Fig. 2K;  $t$ -test of speed ratio versus 1:  $t=0.83$ ,  $df=171$ ,  $P=0.41$ ; s.d. of the speed ratio was 0.10; see also Fig. 1J). Second, the multi-scale property could also not be explained by systematic differences in field-sizes in the long versus short arms of the tunnel, because we found no significant difference in field-sizes between the two arms (Kolmogorov-Smirnov test comparing field-sizes in the long versus short arm:  $P = 0.60$  and  $0.12$  for the two flight-directions [ $D_{KS\ 586,180} = 0.06$  and  $D_{KS\ 628,235} = 0.09$ ]); and, there was no significant difference in field-sizes between the long arm and the full tunnel (fig. S7A; Kolmogorov-Smirnov test:  $P=0.96$  [ $D_{KS\ 1214,1629} = 0.02$ ]). We also found multi-scale coding when restricting the analysis only to the long arm (fig. S7B). Third, the multi-scale property did not stem from an unusual recording-location within CA1. All the recordings were done in the dorsal part of the hippocampus and spanned rather central proximo-distal locations in CA1 (fig. S1A-B): these are the classical recording-locations used in rodents and bats in small laboratory setups. Fourth, the multi-scale property of CA1 neurons could not be explained by spike-sorting quality (fig. S11). Fifth and finally, the results were robust to the detailed criteria of field-detection (fig. S12).

We then looked for possible contributions of landmarks to the multi-scale code. First, we considered several landmark-based compartmentalization models of the environment, whereby the tunnel is assumed to be segmented into smaller portions at the landmark locations, allowing fields to merge at the segment-borders (27). These models could *not* explain the wide distribution of place-field sizes **observed in the data** (fig. S13). Second, we examined the possibility that the multi-scale code could be explained by an over-representation (concentration) of place-fields near the landmarks, and in

particular small place-fields. However, the cumulative distribution of field locations was linear as a function of position along the tunnel (Fig. 3A), with no apparent over-representation near landmarks (but with an over-representation of fields at the two ends of the tunnel, in the reward areas: see fig. S14). We computed the distance of each field's peak to its nearest landmark, and compared the distribution of these distances to the distribution of distances for shuffled place-field locations (27): we found no significant difference between the two (Fig. 3B; Kolmogorov-Smirnov test,  $P \geq 0.18$  for both directions) – **indicating place-fields did not concentrate near landmarks, but were distributed rather uniformly along the tunnel**. This uniform distribution was supported also by an analysis of the gaps between fields, which showed an exponential distribution (Fig. 3C) – indicating lack of structure in the spatial arrangement of place-fields. Additionally, the entire range of field-sizes was represented rather uniformly along the tunnel, with no prominent concentration of small (or large) fields near landmarks (Fig. 3D-E, and fig. S15) – **likely because of the low saliency of these landmarks for the bats** – except a few landmarks which possibly showed slight concentration of fields (Fig. 3D). Further, there was no strong relation between the inter-landmark distance and the field-size (fig. S15B; however, this does not rule out that very large fields would be found in extremely impoverished large regions of space, where absolute spatial information is not available over long distances). **Together, these analyses suggest that the multi-scale statistics were not driven by landmarks.**

### **Comparison between large and small environments**

To examine whether multi-scale coding may be found also in small environments, we recorded from dorsal CA1 of additional 3 bats flying in a short 6-m segment of the tunnel, **which we blocked-off** (see Table S1, dataset 2) (Fig. 4A). This allowed testing directly the effect of environment-size on the spatial coding of neurons in dorsal-CA1 of bats, using the same experimental design. The

percentage of neurons that were active during flight in the short 6-m tunnel (36/67 cells, 53.7%) was much smaller than in the full 200-m tunnel (235/235 cells, 100%) (Table S1) (27). The majority of the active cells were significant place-cells (30/36, 83.3%); thus, almost half of the neurons recorded in the 6-m tunnel were significant place-cells (30/67 cells, 44.8%). Next, we systematically compared the spatial tuning properties of cells in the large versus small environments (Fig. 4B-G). In the 6-m small environment, dorsal CA1 place-cells showed only one or two place-fields (Fig. 4A and Fig. 4B-bottom) – in contrast to the high number of place-fields observed in the large 200-m environment (Fig. 4B-top and Fig. 4E). Across cells, the place-field sizes in the small environment were much smaller than in the large environment (Fig. 4C and Fig. 4F). At the single-cell level, neurons in the small environment had a significantly lower ratio between their largest and smallest fields as compared to the large environment (Fig. 4D and Fig. 4G). **Thus, neurons in the small environment showed virtually no multi-scale coding.**

### **Multi-scale coding of space is independent of both early and recent experience**

Does multi-scale coding of large environments emerge over time, as a function of experience?

First, we asked whether prior experience in the long tunnel is needed for the multi-scale code. We conducted recordings of place-cells from the first exposure to the novel large environment. We recorded 125 place-cells from two bats flying in a 130-meter portion that was blocked out of the 200-meter tunnel, with neural recordings commencing from the very first day in the tunnel (day 1) and continuing over several weeks (with new cells being recorded every day; see Table S1, dataset 3). Cells were spatially tuned already in the first sessions and exhibited many place-fields with different sizes (Fig. 5A). The multi-field multi-scale properties were seen from day 1, and were stable across several weeks of recordings, showing no significant trend in the number of fields (Fig.

5B), field sizes (Fig. 5C), or field-size ratio (Fig. 5D) (overall, place fields in the 130-m tunnel exhibited somewhat smaller numbers of fields, field-sizes and field-size ratios as compared to the 200-m tunnel: see Figs 5B,C,D, bars on the right). **This suggests that the multi-scale coding does not require substantial recent experience with the long tunnel.** While the general multi-scale properties were stable over days (Fig. 5B-D), the cells occasionally exhibited within-day dynamics in the form of fields appearing and disappearing (Fig. 5E). **Interestingly,** the rate of within-day changes was larger during the first two days of the bat in the tunnel (Fig. 5F; two-proportion z-test:  $P < 0.001$ ), but also occurred many days after the first exposure (Fig. 5E, cells 7 and 8; and Fig. 5F) – consistent with previous findings in mice of ongoing changes in the tuning of place-cells (35, 36).

Second, we asked whether laboratory-born bats that were never exposed to large environments would lack a multi-scale code. We recorded from additional 3 adult bats that were born in the lab and grew up in an enriched environment, but have never experienced during development any large-scale environments bigger than a few meters (see Table 1, dataset 4; and fig. S16) (27) – **in contrast to the wild-caught bats that navigated long distances outdoors during development (37).** The lab-born bats were trained to fly in the 200 m tunnel for several weeks and were thus familiar with the environment prior to the neural recordings, similar to the wild-born bats (Fig. 6A). The lab-born bats were in good flight-shape and flew similar distances in the tunnel as the wild-born bats (fig. S16B). Thus the main difference between the lab-born and wild-born bats was their experience during development, with all other experimental conditions being kept identical (Fig. 6A) (27). We recorded 113 cells in dorsal CA1 of the lab-born bats, out of which 95 were place-cells (84.1%) – very similar to the percentage of place-cells in wild-born bats (83.4%). The place-cells of lab-born bats showed a multi-field multi-scale code, with individual neurons exhibiting many fields with varying sizes per-neuron (Fig. 6B, examples; Fig. 6C-E, population) –

similar to place cells recorded from the wild-born bats. We then compared the multi-scale properties between the two groups (Fig. 6C-H): (i) The number of fields per direction was not significantly different (Fig. 6C,F). (ii) Both groups exhibited wide distributions of place-field sizes, with wild-born bats having slightly larger fields (Fig. 6D,G; this difference was *not* due to differences in dorso-ventral recording positions along the longitudinal axis of CA1, which were in fact very similar in both groups [Fig. 6I], but could be **due to the slightly different recording positions** along the proximo-distal axis of CA1 [Fig. 6I]). (iii) The field-size ratio was not significantly different between the groups (Fig. 6E,H), despite the difference in field sizes – indicating a similar multi-scale code between lab-born and wild-born bats.

### **Theoretical decoding analysis showed that for large environments the multi-scale code yields substantial advantages**

We next turned to a theoretical analysis to understand the possible functional advantage of the multi-scale representation of large environments. We compared the performance of six spatial encoding schemes (Fig. 7A) (27): (1) A single small place-field per neuron; (2) A single large place-field per neuron; (3) A single place-field with a gradual increase in field-size across the population – mimicking the dorso-ventral anatomical gradient of field sizes in the hippocampus (17); (4) Multiple small fields per neuron, identical in size for all the neurons (ref. (18)); (5) Multiple fields per neuron, all with the same size for each neuron, but with different scales across different neurons; (6) Multiple fields with multi-scale coding per neuron – as in our data. The distribution of field sizes for schemes 5 and 6 was matched to our data (field-sizes were drawn from a gamma-distribution fitted to the data: fig. S8 (27); the field-size ratio for scheme 6 also closely matched the data – see fig. S17G; and see fig. S17 for variants of schemes 5 and 6 in which we matched also the total coverage of fields to the data). We utilized two types of decoders – a Bayesian Maximum-Likelihood decoder (Fig. 7) and a



Population-Vector decoder (fig. S18), and two integration time-windows –  $\Delta t = 500$  ms (Fig. 7) and  $\Delta t = 200$  ms (fig. S19) (27). We compared the decoding error of simulated data for each of these six encoding schemes, for progressively larger environments. For small environments, all six encoding schemes performed qualitatively equally well – but for very large environments (hundreds of meters), the experimentally-observed encoding scheme with multi-scale place-fields substantially outperformed the other schemes (Fig. 7B-E, fig. S18B-E). **Specifically**, for encoding-schemes with either a single field (schemes 1, 2, 3) or multiple fields of small size (scheme 4), the number of neurons required to accurately decode the animal’s position was extremely large for large environments (Figure 7B, left: note the red, green, pink and yellow lines go out of bounds). By contrast, the two schemes with multiple fields of varying sizes (schemes 5, 6) required only ~50 neurons for accurately decoding the bat’s position even in a very large environment of 1,000 m size (Fig. 7B, left; a 2-meter decoding accuracy). Furthermore, the mean decoding error for schemes 1 and 4 increased dramatically for large environments (Fig. 7C, red and green); but for schemes 5 and 6, the mean decoding error barely increased as a function of the environment-size (Fig. 7C-inset, blue and purple) – maintaining a small decoding error of 5–10 m for a 1,000-m environment, even for a very small ensemble of 50 neurons (Fig. 7C, inset). **We thus conclude that encoding schemes 1–4 are less suitable for very large environments.**

Next, we asked whether scheme 6 – which closely matches our experimental results – offers any functional advantage over scheme 5. We reasoned that scheme 5, where all the fields of the same neuron have the same field-size, is problematic – because when a neuron emits a spike, it could mean that the animal is located in *any* of the neuron’s fields; this creates large positional ambiguity. By contrast, scheme 6, where each neuron has multi-scale fields, alleviates this problem, because the neuron’s spike-count during an integration-time  $\Delta t$  differs between

different fields – i.e. the neuron produces many spikes in large fields but only a few spikes in small fields – and this variability serves to disambiguate which field the animal passed through; this, in turn, improves the decoding accuracy. Indeed, for large 1,000-m environments, the mean decoding error was substantially smaller for scheme 6 than for scheme 5 (Fig. 7C-inset, compare purple and blue lines). Moreover, scheme 6 led to much smaller and fewer catastrophic decoding errors (Fig. 7D-E – compare purple and blue lines: note the ~10-fold difference in the size of catastrophic decoding errors, defined as the 99<sup>th</sup> percentile of the decoding errors [Fig. 7D-inset]; and note also the ~2 or 3-fold difference in the probability of catastrophic errors, defined as the probability of decoding error larger than 5% of the environment size [Fig. 7E]). All these theoretical results were robust to the choice of decoder type (fig. S18), the choice of integration time-window of the decoder (fig. S19), and choice of the parameter that controls the scaling of encoding schemes with environment size (fig. S17H) (27). Together, this theoretical analysis suggested that for small environments, all the encoding schemes perform equally well (Fig. 7B-E: note that all the six lines meet at environment-size of 20 m); by contrast, for very large environments, of hundreds of meters or more, scheme no. 6 – **which matches the large-scale coding that we found in bat CA1** – outperforms all the other coding schemes.

Finally, we suggest that the absence of a multi-scale code in small environments might stem from energy considerations. We used published experimental estimates of the energy (ATP molecules) required to generate one action potential (27, 38), in order to approximate the energy required to represent environments of different sizes – for the various coding schemes (Fig. 7F). In small environments, classical single-field codes (schemes 1–3) were more energetically-efficient than our multi-scale code (scheme 6). Because all the codes exhibit a similar localization performance in small environments, the energetic consideration becomes more important, and

therefore the single-field codes are preferable for small environments. By contrast, in large environments our multi-scale code becomes energetically closer to the single-field codes, and even surpasses some of them in terms of energy consumption (Fig. 7F, compare scheme 6 to the other schemes). More importantly, the localization accuracy of classical single-field codes deteriorates so dramatically in large environments (Fig. 7C-E), that the energetic consideration become largely irrelevant – and the superior localization accuracy of the multi-scale code becomes the central consideration. Thus, we propose that this energetic consideration – and in particular the tradeoff between energy expenditure and coding performance – may explain why in small environments there is no multi-scale code. **Taken together, the theoretical decoding analyses suggest that the multi-scale code is better suited than classical place-codes for representing very large spaces – such as real-world natural environments.**

### **Neural network modeling of multi-scale codes: Attractor networks and feedforward models**

Classical models of hippocampal place-cells are characterized by a single spatial scale per neuron in a given environment (39-47). We investigated two types of models that might support multi-scale representations (figs. S20–S23; see Supplementary Text for further details). First, we employed a continuous attractor neural-network framework (40, 42-44, 47, 48) (fig. S20A-C). We generated a network with multiple interacting attractors at various scales, where each neuron could participate in any of the attractors at a random location (fig. S20A) (27). Network simulations showed coherent bumps of activity at each attractor, with different bump-widths (fig. S21A-B), and single neurons exhibited multi-field multi-scale coding (fig. S20B) – consistent with our experimental data. Second, we explored a set of feedforward models, where CA1 neurons received inputs from CA3 and medial entorhinal cortex (MEC) with diverse synaptic strengths (fig. S20D-J) (27). The

modeling suggested that the experimental data were inconsistent with a strong periodic grid input – and were most consistent with a model in which the major input into CA1 comes from CA3, wherein individual CA3 neurons exhibit a single place-field (Supplementary Text; and fig. S20J). We thus predict that in very large environments: (i) MEC neurons should not exhibit strong periodicity, and (ii) place-cells in CA3 (unlike those in CA1) should exhibit single place-fields.

## Discussion

We found here a multi-scale neural code for large environments: single hippocampal neurons in the dorsal-CA1 area of bats exhibited many fields, and the different fields of the same neuron varied dramatically in size – with up to 20-fold ratio in the size of different place-fields for the *same* neuron. This unknown coding scheme was revealed via the use of an extremely large environment. This **finding constitutes a fundamentally** different phenomenon from the well-known gradient of place-field sizes along the longitudinal anatomical axis of the hippocampus (14, 17, 49) – wherein each neuron has one characteristic spatial scale, and this scale changes between neurons based on anatomical position. Here, by contrast, all the recordings were conducted in the same anatomical position – **dorsal CA1 (fig. S1)** – and we found that individual neurons did not have a characteristic scale, but rather the spatial scale of the *same* neuron varied dramatically across the environment. Further, this neural code was observed from the first exposure-day to the environment, and was similar between lab-born and wild-born bats – suggesting that the multi-scale code is a very robust phenomenon, **which does not require substantial recent experience with the test-environment, nor early experience with large environments in general.**

Previous studies in rodents have reported multiple place-fields for individual CA1 neurons in (relatively) large environments (18, 31, 32) – although the number of fields per neuron was much

smaller than we found here – but no study to date has found the multi-scale property that we discovered here for individual neurons. Our theoretical decoding analysis provides a simple functional explanation for this multi-scale code: For very large environments, multi-scale coding outperforms all the other codes that we considered, in terms of reducing the number of required neurons and minimizing the decoding errors. We hypothesize that the reason why previous studies (18, 31, 32) did not find a multi-scale code was that they used much smaller environments, or concatenated small compartments – where such a code does not provide a functional advantage. Indeed, recordings from bats flying in a small environment did not show a multi-scale code (Fig. 4).

The absence of a multi-scale code in the small environment can be interpreted in two ways: (i) Neurons in small environments exhibit the classical place-code, and switch to a multi-scale code in large environments. (ii) Multi-scale coding is the underlying representation in all environmental scales – but the multi-scale nature of the code cannot be revealed in small environments, where the firing reflects a small ‘pinhole view’ of the larger multi-scale map, and therefore the largest fields are too big to be seen because they cover the entire space. However, option (ii) seems unlikely, because we would then expect to see in the 6-m setup many neurons that fire over the entire environment, thus reducing substantially the percentage of place-cells out of the neurons active in-flight – but in fact, these percentages were remarkably similar between the 6-m and 200-m environments (83.3% and 83.4%, respectively).

Our multi-scale findings open the way for numerous future questions on the neurobiology of large-scale navigation. For example: What are the mechanisms that underlie this multi-scale coding that we discovered? Our network modeling suggested that one possibility is a feedforward convergence of inputs from CA3, where each CA3 neuron has a single field (fig. S20D-left, and fig. S20J) – and it also predicted that MEC neurons should not exhibit spatial periodicity in large environments (fig. S20G-I).

Further: What is the biological decoder that may read this code downstream? How are such large spaces learned by the hippocampal system? Are there ultra-long compressed firing sequences during rest and sleep, similar to sequences observed in laboratory environments (50-52) – but now extending over hundreds of meters, or more? If so, what are the mechanisms that could create these sequences under this multi-scale code – where each neuron would participate multiple times in each sequence, each time with a different resolution? More broadly, these findings call for performing neurophysiological research in very-large-scale environments on all types of hippocampal and entorhinal spatial neurons. We posit that such research is crucial for understanding the brain’s ‘navigation circuit’, for two reasons: First, because most animals and humans evolved to navigate **in multi-compartment environments with different spatial scales, including very large scales** – so it is important to conduct neurobiological research on large scales. Second, studies in humans have emphasized that spatial scale is important for navigation: People navigate differently in large versus small environments, which calls for conducting navigation experiments in very large environments (53). Our study provides direct single-neuron evidence that the use of a real-world spatial scale can reveal a fundamentally new kind of spatial coding in the hippocampus. This work thus makes a step towards bridging the major gap between the neurobiological tradition of studying the brain’s navigation circuit in small-scale laboratory setups, and the ecological tradition of studying large-scale animal navigation outdoors.

## Materials and Methods Summary

We conducted tetrode-based recordings of single neurons in dorsal hippocampus area CA1 of Egyptian fruit bats (*Rousettus aegyptiacus*) – in both wild-born and lab-born bats – using a wireless electrophysiology system, while the bats were flying in a very large environment (200 m long tunnel), in either familiar or novel conditions. For comparison, we also recorded from bats flying in a 6 m segment of the tunnel. The experimental datasets are summarized in Table S1. We localized the bat's position in the tunnel using a radio-frequency based system yielding ~9 cm precision. We computed firing-rate maps separately for each flight direction, and used spatial information and a shuffling procedure to identify significant place-cells. Individual place-fields were detected as prominent, stable and significantly-tuned peaks in the firing-rate maps. To theoretically compare the observed spatial coding scheme to a set of five other coding schemes, we generated synthetic data for each coding scheme and then used maximum-likelihood and population-vector decoders to test their decoding performance. To theoretically explore the possible neural-network mechanisms underlying the observed coding, we considered both an attractor network model, based on multiple interacting attractors that randomly share neurons between them, as well as 4 feedforward models, based on inputs from MEC and CA3. Further details can be found in the online Materials and Methods.

## References and Notes

1. J. O'Keefe, J. Dostrovsky, *Brain Res.* **34**, 171-175 (1971).
2. J. O'Keefe, L. Nadel, *The Hippocampus as a Cognitive Map* (Oxford University Press, 1978).
3. P. Andersen, R.G.M. Morris, D.G. Amaral, T.V. Bliss, J. O'Keefe, Eds., *The Hippocampus Book* (Oxford University Press, 2007).
4. J.B. Ranck, Jr., *Soc. Neurosci. Abstr.* **10**, 599 (1984).
5. J.S. Taube, R.U. Muller, J.B. Ranck, Jr., *J. Neurosci.* **10**, 420-435 (1990).
6. T. Hafting, M. Fyhn, S. Molden, M.-B. Moser, E.I. Moser, *Nature* **436**, 801-806 (2005).
7. C. Barry, R. Hayman, N. Burgess, K.J. Jeffery, *Nat. Neurosci.* **10**, 682-684 (2007).
8. T. Solstad, C.N. Boccara, E. Kropff, M.-B. Moser, E.I. Moser, *Science* **322**, 1865-1868 (2008).
9. C. Lever, S. Burton, A. Jeewajee, J. O'Keefe, N. Burgess, *J. Neurosci.* **29**, 9771-9777 (2009).
10. E.I. Moser, M.-B. Moser, B.L. McNaughton, *Nat. Neurosci.* **20**, 1448-1464 (2017).
11. M.A. Wilson, B.L. McNaughton, *Science* **261**, 1055-1058 (1993).
12. S. Leutgeb *et al.*, *Science* **309**, 619-623 (2005).
13. C.D. Harvey, F. Collman, D.A. Dombeck, D.W. Tank, *Nature* **461**, 941-946 (2009).
14. S. Royer, A. Sirotta, J. Patel, G. Buzsáki, *J. Neurosci.* **30**, 1777-1787 (2010).
15. I. Lee, D. Yoganarasimha, G. Rao, J.J. Knierim, *Nature* **430**, 456-459 (2004).
16. J.K. Leutgeb, S. Leutgeb, M.-B. Moser, E.I. Moser, *Science* **315**, 961-966 (2007).
17. K.B. Kjelstrup *et al.*, *Science* **321**, 140-143 (2008).
18. P.D. Rich, H.P. Liaw, A.K. Lee, *Science* **345**, 814-817 (2014).
19. K.D. Taylor, *J. Appl. Ecol.* **15**, 663-677 (1978).
20. J.C. Russell, A.J.C. McMorland, J.W.B. MacKay, *Anim. Behav.* **79**, 159-164 (2010).
21. M. Geva-Sagiv, L. Las, Y. Yovel, N. Ulanovsky, *Nat. Rev. Neurosci.* **16**, 94-108 (2015).
22. A. Tsoar *et al.*, *Proc. Natl. Acad. Sci. USA* **108**, E718-724 (2011).
23. N. Ulanovsky, C.F. Moss, *Nat. Neurosci.* **10**, 224-233 (2007).
24. M.M. Yartsev, M.P. Witter, N. Ulanovsky, *Nature* **479**, 103-107 (2011).
25. M.M. Yartsev, N. Ulanovsky, *Science* **340**, 367-372 (2013).
26. A. Finkelstein *et al.*, *Nature* **517**, 159-164 (2015).
27. Materials and Methods are available as supporting material on *Science* online.
28. L.T. Thompson, P.J. Best, *J. Neurosci.* **9**, 2382-2390 (1989).
29. B.L. McNaughton, C.A. Barnes, J. O'Keefe, *Exp. Brain Res.* **52**, 41-49 (1983).
30. M. Geva-Sagiv, S. Romani, L. Las, N. Ulanovsky, *Nat. Neurosci.* **19**, 952-958 (2016).



31. A.A. Fenton *et al.*, *J. Neurosci.* **28**, 11250-11262 (2008).
32. E. Park, D. Dvorak, A.A. Fenton, *PLoS One* **6**, e22349 (2011).
33. G. Buzsáki, K. Mizuseki, *Nat. Rev. Neurosci.* **15**, 264-278 (2014).
34. J.S. Lee, J.J. Briguglio, J.D. Cohen, S. Romani, A.K. Lee, *Cell* **183**, 620-635 (2020).
35. Y. Ziv *et al.*, *Nat. Neurosci.* **16**, 264-266 (2013).
36. A. Rubin, N. Geva, L. Sheintuch, Y. Ziv, *eLife* **4**, e12247 (2015).
37. L. Harten, A. Katz, A. Goldshtein, M. Handel, Y. Yovel, *Science* **369**, 194-197 (2020).
38. S. Hallermann, C.P. de Kock, G.J. Stuart, M.H. Koe, *Nat. Neurosci.* **15**, 1007-1014 (2012).
39. D. Zipser, *Behav. Neurosci.* **99**, 1006-1018 (1985).
40. M. Tsodyks, T. Sejnowski, *Int. J. Neural Syst.* **6**, 81-86 (1995).
41. J. O'Keefe, N. Burgess, *Nature* **381**, 425-428 (1996).
42. A. Samsonovich, B.L. McNaughton, *J. Neurosci.* **17**, 5900-5920 (1997).
43. F.P. Battaglia, A. Treves, *Phys. Rev. E* **58**, 7738-7753 (1998).
44. M. Tsodyks, *Hippocampus* **9**, 481-489 (1999).
45. T. Hartley, N. Burgess, C. Lever, F. Cacucci, J. O'Keefe, *Hippocampus* **10**, 369-379 (2000).
46. T. Strössl, D. Sheynikhovich, R. Chavarriaga, W. Gerstner, *Neural Netw.* **18**, 1125-1140 (2005).
47. J.J. Knierim, K. Zhang, *Annu. Rev. Neurosci.* **35**, 267-285 (2012).
48. R. Ben-Yishai, R.L. Bar-Or, H. Sompolinsky, *Proc. Natl. Acad. Sci. USA* **92**, 3844-3848 (1995).
49. M.W. Jung, S.I. Wiener, B.L. McNaughton, *J. Neurosci.* **14**, 7347-7356 (1994).
50. D.J. Foster, M.A. Wilson, *Nature* **440**, 680-683 (2006).
51. K. Diba, G. Buzsáki, *Nat. Neurosci.* **10**, 1241-1242 (2007).
52. T.J. Davidson, F. Kloosterman, M.A. Wilson, *Neuron* **63**, 497-507 (2009).
53. T. Wolbers, J.M. Wiener, *Front. Hum. Neurosci.* **8**, 571 (2014).

## Acknowledgements

We thank K.D. Harris and A. Treves for suggestions; D. Omer, A. Rubin, T. Stolerio, M. Naim, A. Sarel, S. Palgi and S. Ray for comments on the manuscript; S. Futerman, I. Shulman, B. Pevzner, K. Dor, S. Kodenzik, E. Solomon, C. Cohen, A. Shalev, N. Raish and L. Hartman for help with bat training; G. Ankaoua and B. Pasmantirer for mechanical designs; A. Tuval for veterinary support; C. Ra'anan and R. Eilam for histology; and G. Brodsky for graphics. N.U. is the incumbent of the Barbara and Morris Levinson Professorial Chair in Brain Research. This study was supported by research grants to N.U. from the European Research Council (ERC-CoG – NATURAL\_BAT\_NAV), Deutsche Forschungsgemeinschaft (DFG – SFB 1372), and Yehuda and Judith Bronicki, and by the André Deloro Prize for Scientific Research and the Kimmel Award for Innovative Investigation to N.U. T.E. was supported by the Otto Schwarz Scholarship, the Horowitz KKL-JNF foundation, and by the Maccabim Foundation Excellence Fellowship for Ph.D students. **The data and code that support the conclusions of this study are available from the authors upon a reasonable request, and are also accessible online at Zenodo (DOI: 10.5281/zenodo.4646728).**

## Supplementary Materials

Materials and Methods

**Supplementary Text**

Figs. S1–**S23**

Table S1

Supplementary References

**Fig. 1. Neuronal and behavioral recordings from bats flying over large spatial scales.** (A) 16-channel wireless neural logger. (B) Neural traces from one tetrode, recorded in bat dorsal hippocampal area CA1, **showing spikes in-flight**. (C) Spike-sorting of one tetrode (data from full session: 108 min). Shown are spike-clusters from different neurons, with spike-amplitudes plotted for 3 of the tetrode's channels; well-isolated units are shown in different colors. Same session and tetrode as in B. (D) Histology of one recording-site in dorsal CA1. Red arrowhead, electrolytic lesion; Black lines, proximal and distal borders of CA1. (E) Aerial photograph showing top-view of the large-scale environment. The flight-tunnel was composed of long and short arms (27), which the bat traversed without slowing-down (see panel I). Vertical lines, location where neural data in B were recorded. (F) Localization system, showing positions of ground-based antennas (red dots), the tunnel (dark-gray thick line), snapshot of measured distances from each antenna to the localization-tag on the bat's head (large black circles; cropped for visualization purposes), and the bat's estimated location (blue dot: computed as the intersection of the black circles). (G) Precision of the localization system (27), showing localization error of  $\sigma=8.9$  cm along the tunnel's major axis. (H) Example session, showing the Y-Z positions of the bat's passages (blue dots) through a cross-section in the tunnel's mid-point (black outline). Note the relatively small deviations of the blue dots in the Y and Z axes – indicating the bat flew essentially in 1D trajectories (see also fig. S3B-C). (I) Example session showing speed-profiles along the tunnel, pooled over both flight-directions. Gray areas show locations of low flight-speeds, due to takeoff and landing, which were removed from further analysis of place-fields (27). (J) Distribution of the coefficient of variation (CV) of the flight-speed per session ( $n=60$  sessions; 5 bats). The CV was computed over the tunnel's high-speed portion (excluding the gray areas from I); **mean CV=0.042**. (K) Distribution of number of flights (laps) per direction per session; shown are only valid unidirectional long flights (27). Red and blue colors in K and J: the two flight directions (see arrows). (L) Distribution of total distance flown per-session, based on long flights only ( $n=60$  sessions; 5 bats).

**Fig. 2. Dorsal CA1 hippocampal neurons represented very large space using many fields with multi-scale coding.** (A) Examples of firing-rate maps and raster-plots for 9 cells. For each neuron: Top, firing-rate maps calculated separately for each flight-direction (red and blue, see arrows above cell 1); Bottom, raster plots of spike-positions ( $x$ -axis) for different flights, or laps ( $y$ -axis); the detected place-fields are marked by red- and blue-colored thick horizontal lines above the raster plots (fields inside the low-flight-speed zones [gray] were excluded (27)). In each example the smallest and largest field sizes are indicated (min, max), together with the ratio between them; the numbers of fields in each direction are indicated in blue and red on the right. For cells 3 and 7 shown are also zoom on their smallest field (cell 3: field size 1.0 m, cell 7: field size 0.9 m). (B–D) Distribution of spatial information (B), sparsity (C), and the total coverage of the environment by place-fields (D) – calculated for the firing-rate map in each flight-direction separately (i.e., ‘No. of cells’ here refers to significant cells  $\times$  directions;  $n=331$ ). In panel D: bottom  $x$ -axis, total coverage in meters; top  $x$ -axis, total coverage in percent of tunnel-length. (E) Distribution of firing-map correlations between odd and even flights ( $n=331$  cells  $\times$  directions), **showing high correlation values (median  $r=0.87$ )**. (F) Distribution of firing-map correlations between the two flight directions (gray;  $n=135$  cells, including only cells where both directions were significantly tuned) **was similar to cell-shuffled distribution (black) (Kolmogorov-Smirnov test:  $P=0.12$  [ $D_{KS\ 135,13566} = 0.10$ ])**. (G) Distribution of number of place-fields per neuron per flight-direction ( $n=331$  cells  $\times$  directions). Rightmost bar, cases with  $\geq 20$  fields per direction. **Mean number of fields per direction was 4.9**. (H) Distribution of place-field size ( $n=1,629$  fields). Note the field size ranged from sub-meter (leftmost bar of histogram) up to 32-m size. (I and J) Single cells exhibited multi-scale field sizes (plotted are  $n=172$  cells with  $\geq 2$  fields). (I) Distributions of smallest and largest field-sizes per neuron (shown cells with  $\geq 2$  fields). (J) Distribution of the ratio between largest and smallest field-sizes for each neuron. Note both axes here are in log-scale. (K) Lack of correlation between largest-to-smallest field size ratio and the speed-ratio at the locations of those fields (plotted are  $n=172$  cells with  $\geq 2$  fields). For all histograms in this figure, except panel F: red vertical line indicates mean of distribution, red dot with red horizontal line indicate median and interquartile range.

**Fig. 3. Place fields were distributed uniformly along the tunnel.** (A) Cumulative fraction of peak firing-rate locations for all the place-fields along the tunnel, pooled across all the 5 bats and 196 place-cells; plotted for each flight-direction separately (East direction, blue:  $n=863$  fields; West direction, red:  $n=766$  fields). Gray vertical lines, locations of landmarks (note we did not treat the landing-balls as ‘landmarks’). (B) Distributions of the distances of each field’s peak to its nearest landmark (blue and red, flight directions), were similar to shuffle distributions (black) (Kolmogorov Smirnov test:  $P=0.82$  [ $D_{KS} 782,7820000 = 0.02$ ] and  $P=0.18$  [ $D_{KS} 661,6610000 = 0.04$ ] for the two flight-directions). (C) Distribution of gaps between fields (gray bars), overlaid with exponential fit (black line), plotted on a logarithmic y-scale. **The good fit to the exponential distribution indicates lack of spatial structure in the field locations.** (D) Field size versus the location of field-peak, pooled across all bats and neurons. Gray vertical lines, locations of landmarks; open circles, fields larger than 20 m. Note the entire range of field-sizes was represented along the entire tunnel. (E) Distribution of field-size for the two directions (blue and red), plotted separately for fields located close to landmarks (thin line, fields  $< 5$  m from nearest landmark) or far from landmarks (thick line, fields  $\geq 5$  m from nearest landmark). **No significant differences in field-size were found between fields located close or far from a landmark** (Kolmogorov Smirnov test:  $P=0.80$  [ $D_{KS} 577,205 = 0.05$ ] and  $P=0.25$  [ $D_{KS} 469,192 = 0.09$ ] for the two flight-directions). In panels B and E we excluded fields whose peak occurred before the first landmark or after the last landmark in the tunnel, where the assignment of ‘nearest-landmark’ is one-sided and hence biased (the same was done for the shuffles in B).

**Fig. 4. No multi-scale coding was found in a small-scale environment.** Experiments were done in a small 6-meter segment of the long 200-meter tunnel, which we blocked with two curtains (Table S1: dataset 2). (A) Examples of firing-rate maps and raster-plots for dorsal-CA1 place cells recorded in this small-scale environment. Same graphical conventions as in Fig. 2A. **Note that most cells had a single field per direction, or two fields with a similar scale.** (B–D) Distributions of number of fields

(B), fields sizes (C) and field size ratio (D), for the two different dorsal-CA1 datasets: large-scale 200 m environment (top row) and small-scale 6 m environment (bottom row). Red vertical lines, mean of distribution; red horizontal lines and red dot, interquartile range and median. Inset in panel C-bottom shows zoom-in. Black bars in panel D show neurons with 1 field. (E–G) Comparison between the two datasets (large versus small environment), for the three quantities: number of fields (E), field sizes (F), and field size ratio (G; here we included only neurons with  $\geq 2$  fields). Error bars, mean  $\pm$  s.e.m. **There was a highly-significant difference in all these 3 quantities between large-scale and small-scale environments, indicating that the multi-field multi-scale coding is expressed most prominently in large-scale environments** (panel E: *t*-test with unequal variances,  $P=6.7\times 10^{-44}$ ,  $t=15.94$ ; Wilcoxon rank-sum test,  $P=1.5\times 10^{-15}$ ,  $z=7.89$ ; panel F: *t*-test with unequal variances,  $P=4.5\times 10^{-58}$ ,  $t=29.56$ ; Wilcoxon rank-sum test,  $P=3.9\times 10^{-26}$ ,  $z=10.51$ ; panel G: *t*-test with unequal variances,  $P=1.8\times 10^{-14}$ ,  $t=8.91$ ; Wilcoxon rank-sum test,  $P=4.6\times 10^{-5}$ ,  $z=3.91$ ; \*\*\*\*\* indicates  $P < 10^{-5}$  for the *t*-tests in panels E,F,G).

**Fig. 5. Multi-scale coding exists already from the first days of exposure to the tunnel.** Experiments from day 1 were conducted in a 130-m portion of the 200-m tunnel (Table S1: dataset 3). (A) Examples of firing-rate maps and raster-plots for 4 cells recorded in large-scale environment during the first days of exposure. Same graphical conventions as in Fig. 2A. The days since first exposure are indicated for each cell (day 1 is the very first day of exposure; day-count represents experimental days). (B–D) Population scatter plots of the number of fields per direction (B), field sizes (C) and field size ratio (D) as a function of days since first exposure. **Note the lack of trend across days (Spearman  $\rho$ ,  $P > 0.13$  for all three scatters), suggesting the multi-scale coding exists already from day 1.** For display purposes only, dots were jittered along the *x*-axis (uniform jitter of  $\pm 0.5$  days); in panel B dots were jittered also along the *y*-axis (uniform jitter of  $\pm 0.3$  fields); all correlations were computed without the jitter. Error bars in main plots, mean  $\pm$  s.d (using 5-day bins with no overlap). Insets (gray bars) show mean  $\pm$  s.e.m. for the three

tunnel lengths used in this study: 6 m, 130 m and 200 m. (E) Four examples of within-day dynamics in spatial tuning. Raster plots show spike positions in each flight (blue/red dots: flight directions), with the behavioral coverage shown with light gray lines. Arrowheads denote field appearance (filled arrowheads) or disappearance (empty arrowheads). **Note these dynamics occurred in both small and large fields, and happened both on the first days of exposure (cells 5 and 6) and after  $\geq 1$  month (cells 7 and 8).** (F) Probability of appearance and disappearance of fields (per-flight probability of change in any of the fields), grouped by the day from first exposure: days 1-2, days 3-4, days 5-6 and  $\geq 7$  days. Error bars, mean  $\pm$  standard error of the proportion (27). In the first two days after exposure, the cells exhibited a higher probability of appearance/disappearance of fields than on later days (two-proportion z-test:  $P < 0.001$  for all 6 tests comparing days 1-2 versus the other days). The probabilities for appearance and disappearance were similar over the entire course of exposure (compare black versus white bars; two-proportion z-test:  $P=0.64$ , pooled over all days) – **consistent with the overall stability over weeks in the number of fields per neuron (B).** \*\*\*\*\*  $P < 10^{-5}$ , \*\*\*\*  $P < 10^{-4}$ , \*\*\*  $P < 10^{-3}$ .

**Fig. 6. Multi-scale coding does not require early exposure to large-scale environments during development.** Comparison of multi-scale properties between lab-born bats that were raised in a 5-meter sized room (27) and have never experienced large-scale environments during development (green; Table S1: dataset 4), versus wild-born bats that were caught as adults outdoors (gray). Both groups of bats were tested under identical conditions **in the 200-meter tunnel**. (A) Schematic of experimental design. The only difference between lab-born and wild-born bats occurred during early life; subsequent stages were identical – both groups spent several months in the same colony-room prior to surgery, and then the training and recording procedures were identical for both groups. (B) Examples of firing-rate maps and raster-plots for six cells recorded from lab-born bats flying in the large-scale environment (200-m tunnel). Same graphical conventions as in Fig. 2A. (C–E) Distributions of number of fields per direction (C), field sizes (D) and field-size ratio (E), for lab-born bats (green) and wild-born bats (gray),

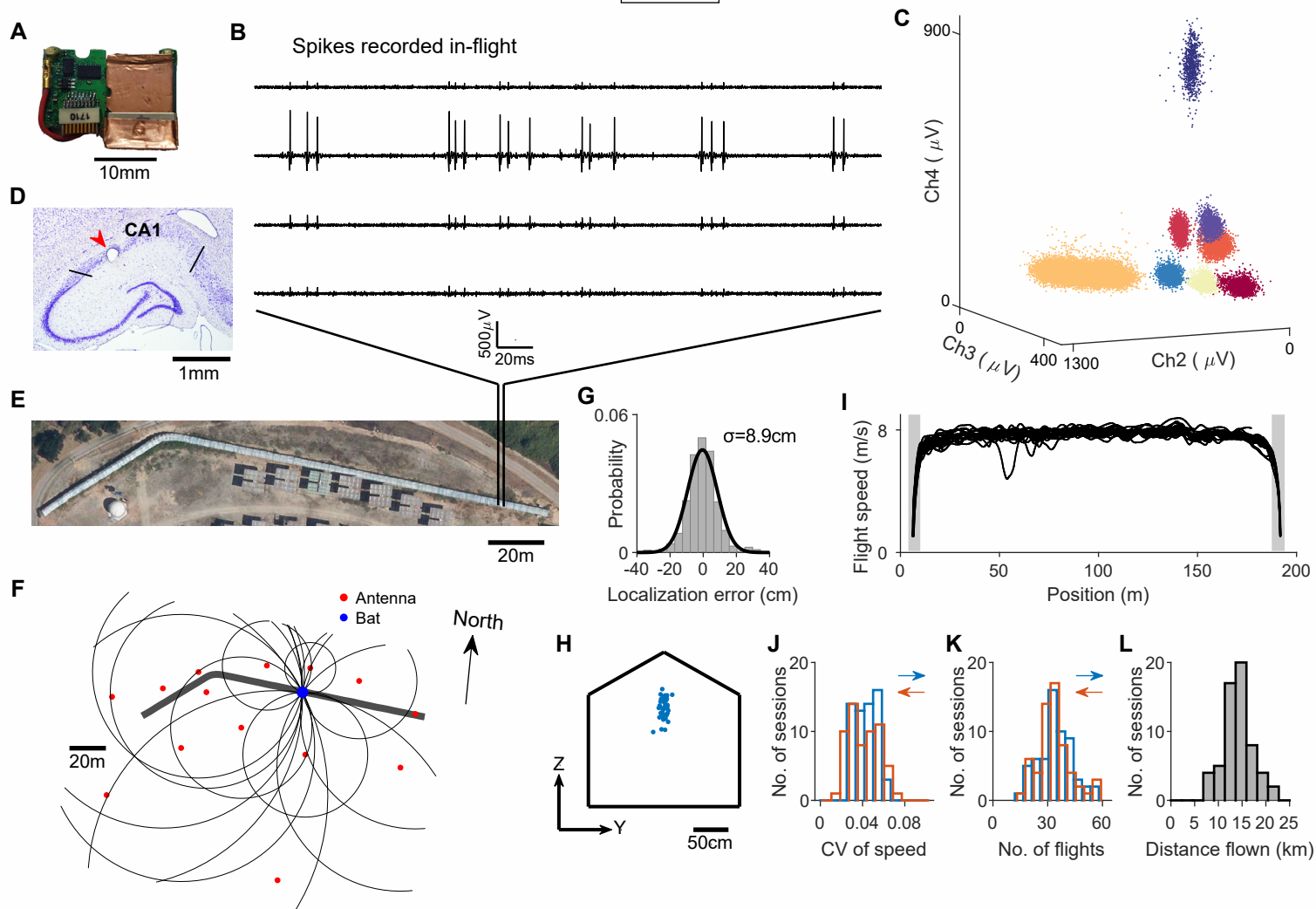
recorded in the same large-scale environment (panel C:  $n_{\text{lab}}=161$  cells  $\times$  directions,  $n_{\text{wild}}=331$ ; panel D:  $n_{\text{lab}}=649$  fields,  $n_{\text{wild}}=1,629$ ; panel E:  $n_{\text{lab}}=82$  cells,  $n_{\text{wild}}=172$  [only cells with  $\geq 2$  fields shown in E]). Main plots, y-axis in log scale; Insets, same histograms with y-axis in linear scale. (F–H) Population comparisons between lab-born and wild-born bats: number of fields per direction (F), field sizes (G) and field-size ratio (H). Boxplots denote the median (horizontal line), 25%–75% (box) and 10-90% (whiskers);  $P$ -values of Wilcoxon rank-sum tests are indicated (F:  $df=490$ ,  $z=-1.33$ ; G:  $df=2,276$ ,  $z=-8.92$ ; H:  $df=252$ ,  $z=-0.47$ ). Despite significant difference in the field-sizes distribution (panel G:  $P=5 \times 10^{-19}$ ), the field-size ratio distribution did not differ significantly (panel H:  $P=0.64$ ) – **indicating that the multi-scale code exists also in neurons recorded from lab-born bats.** (I) Anatomical positions of tetrodes along the CA1 longitudinal (dorso-ventral) axis and proximo-distal axis (0% longitudinal: dorsal [septal] pole of CA1; 0% proximo-distal: proximal border with CA2). **Tetrodes from both groups had similar longitudinal coordinates in dorsal CA1, but lab-born bats' tetrodes concentrated more proximally along the proximo-distal axis of CA1.**

**Fig. 7. Theoretical analysis showed that multi-scale coding decreases the decoding error for large environments.** Decoding accuracy analysis for simulations of six different models (encoding schemes), using Maximum Likelihood decoder and integration time-window of 500 ms (27). (A) We examined six different encoding schemes for spatial representations – shown here are 10 simulated example neurons for each scheme: (1) single field with small size; (2) single field with large size; (3) single field with gradually increasing field-size across neurons – mimicking the dorso-ventral anatomical gradient of field sizes; (4) multiple small fields (the distribution of field-propensity was taken from ref. (18)); (5) multiple fields with fixed size per neuron, but with variable sizes across the population; (6) multiple fields with multi-scale per neuron (as in the bat data). In schemes 5 and 6 we matched the distribution of field-sizes to our data (fig. S8). The mean coverage in schemes 2, 5, 6 was identical (27). (B) Left, minimal number of neurons required for reaching mean decoding error  $< 2$  m, plotted as a function of

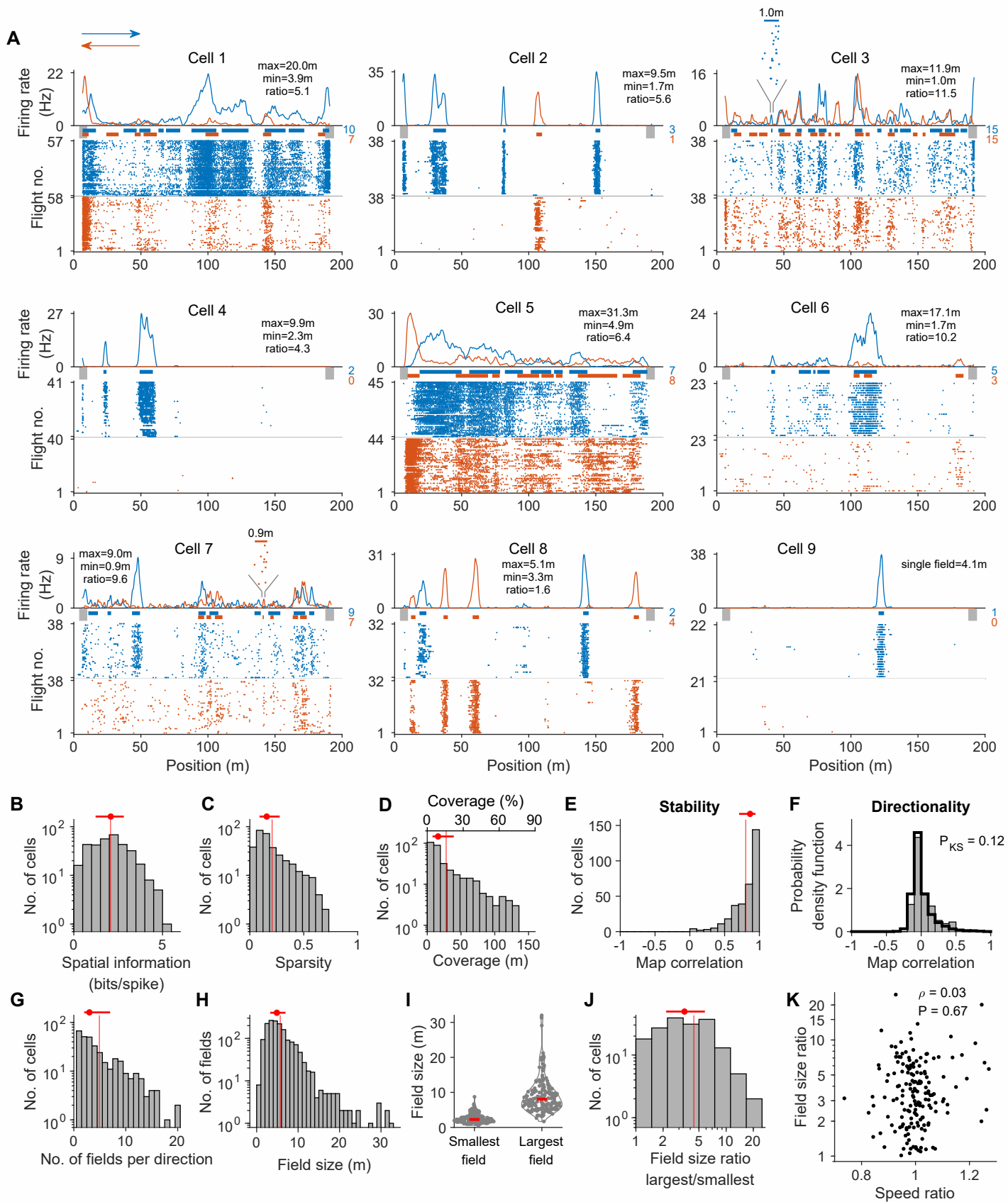


different environment sizes (from 20 m to 1,000 m). Right, slopes of the curves on the left, representing how many additional neurons are required on average when increasing the environment size by 1 m. Colors represent the six encoding schemes. (C–E) Decoding errors when using  $N=50$  neurons. (C) Mean decoding error versus environment size, showing that schemes 1, 3, 4 exhibit huge decoding errors for large environments. Inset, zoom on errors smaller than 20 m (see  $y$ -axis), showing that per-neuron multi-scale encoding (scheme 6: purple) outperforms fixed scale per-neuron (scheme 5: blue) in terms of mean decoding error. (D and E) Catastrophic errors. (D) Rare large errors (99<sup>th</sup> percentile of decoding error), plotted versus environment size. Inset: same plot in log-scale for the  $y$ -axis. (E) Probability of decoding error larger than 5% of the environment size, plotted as a function of environment size. (F) Theoretical estimate of energy expenditure under the various coding schemes: Shown is the number of ATP molecules per second required to represent the environment with mean decoding error  $< 2$  meters, plotted against the environment size (27).

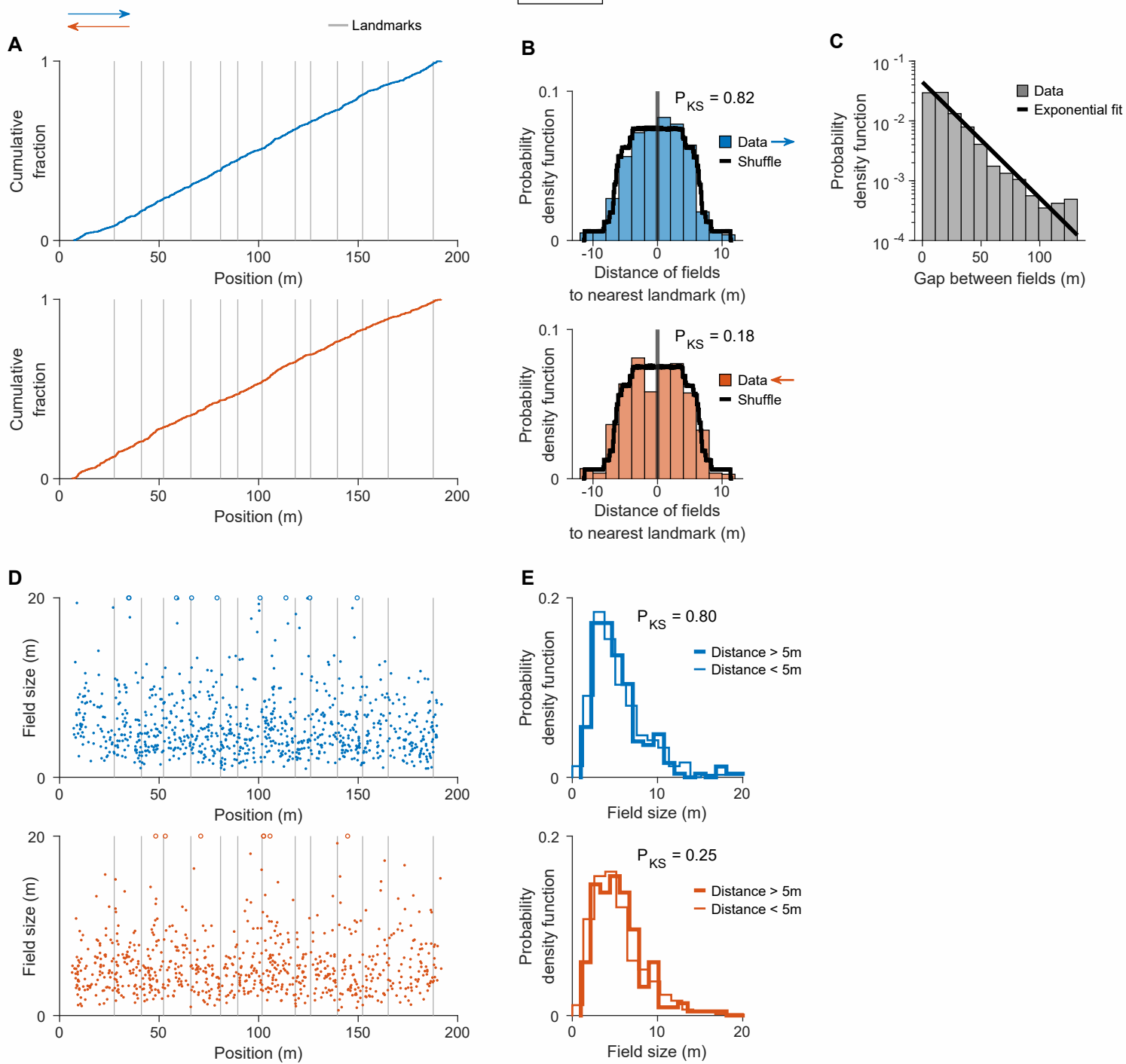
Fig\_1



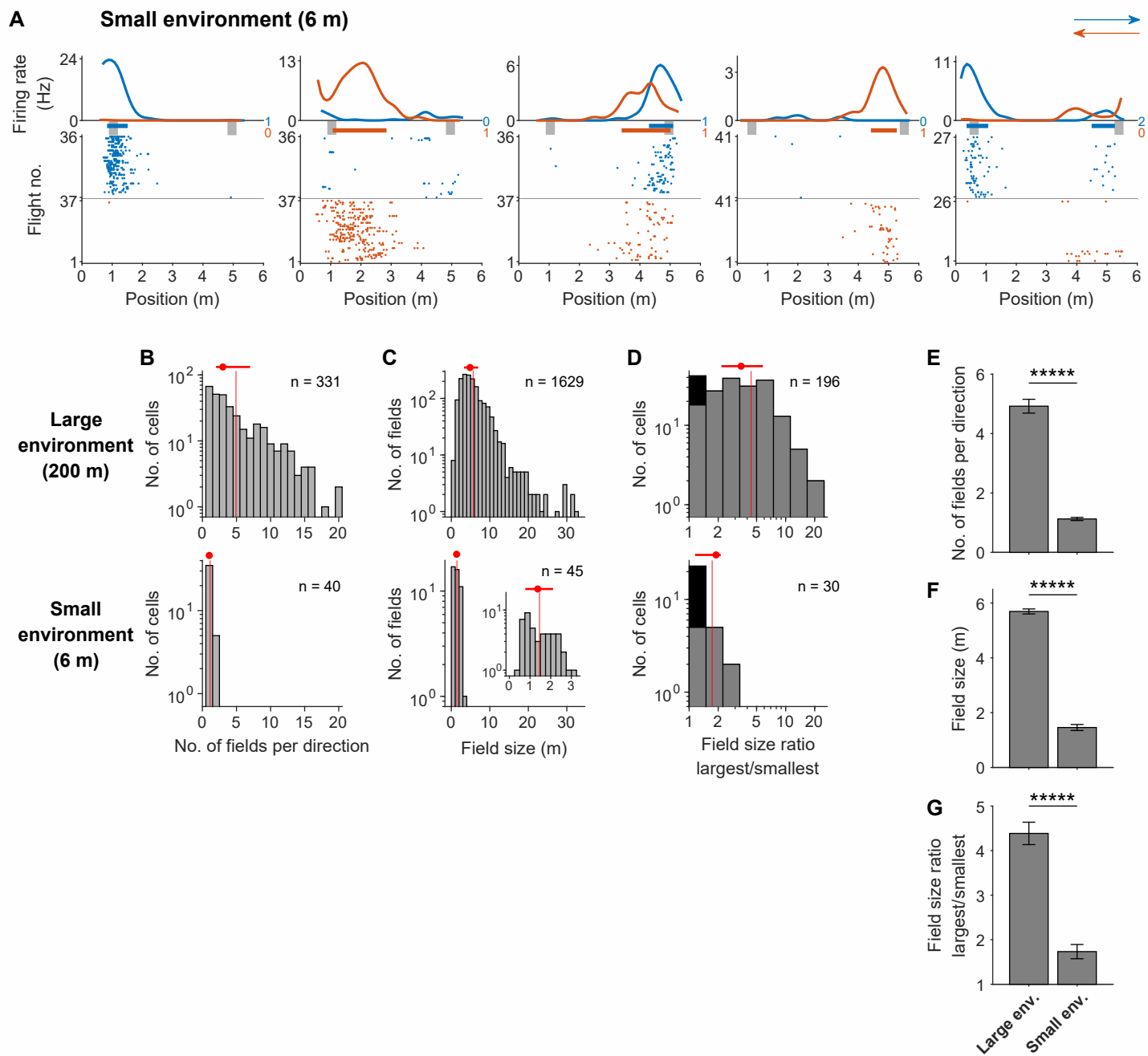
Fig\_2



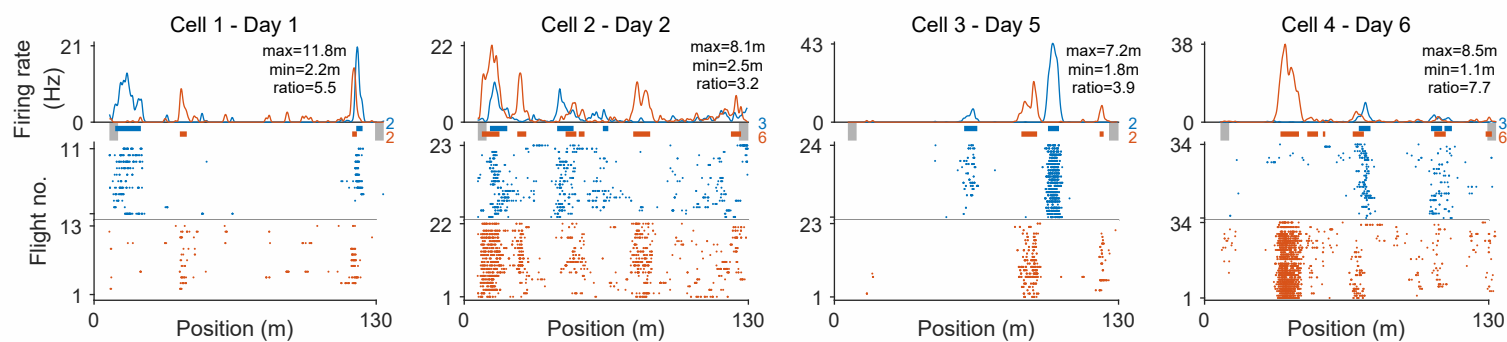
Fig\_3



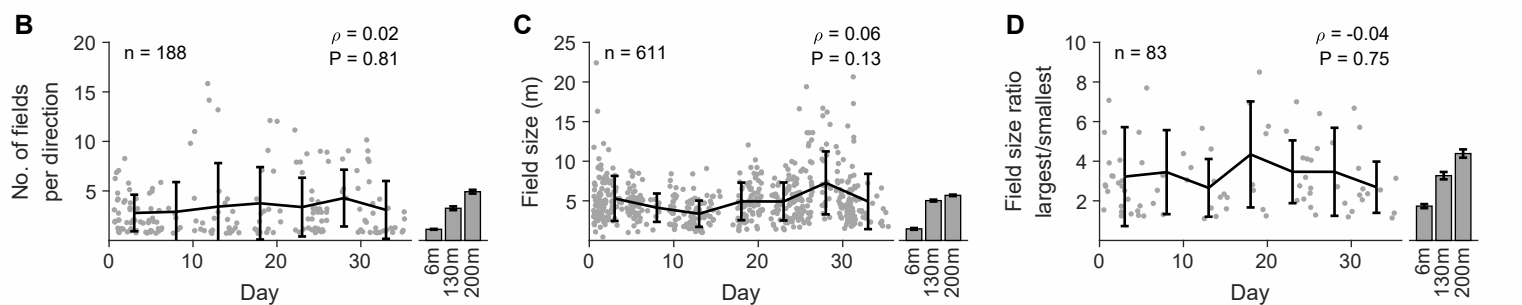
Fig\_4



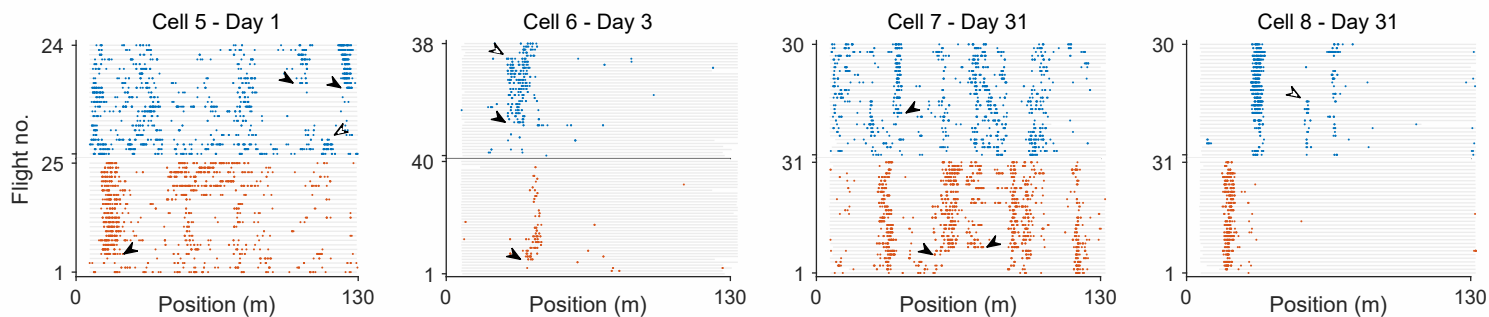
# A Examples of multi-scale coding in the first days of exposure to the tunnel



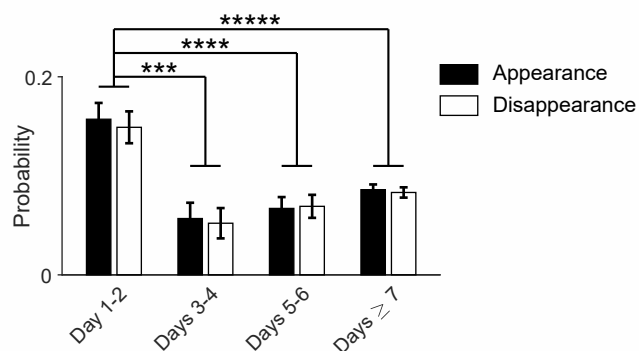
## Population: Stability of multi-scale coding across weeks, starting from day 1 in the tunnel



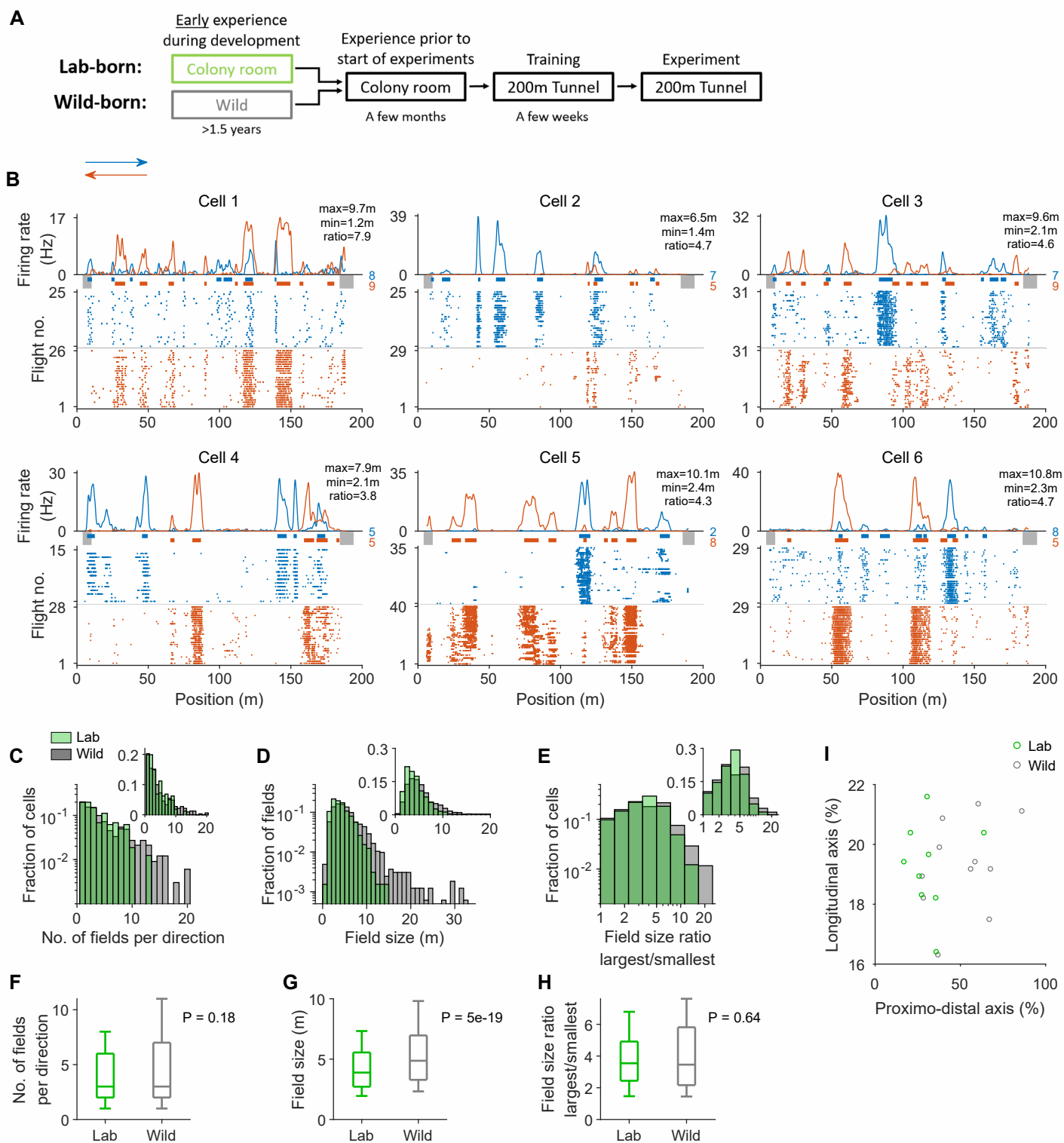
# E Examples of within-day dynamics in spatial tuning



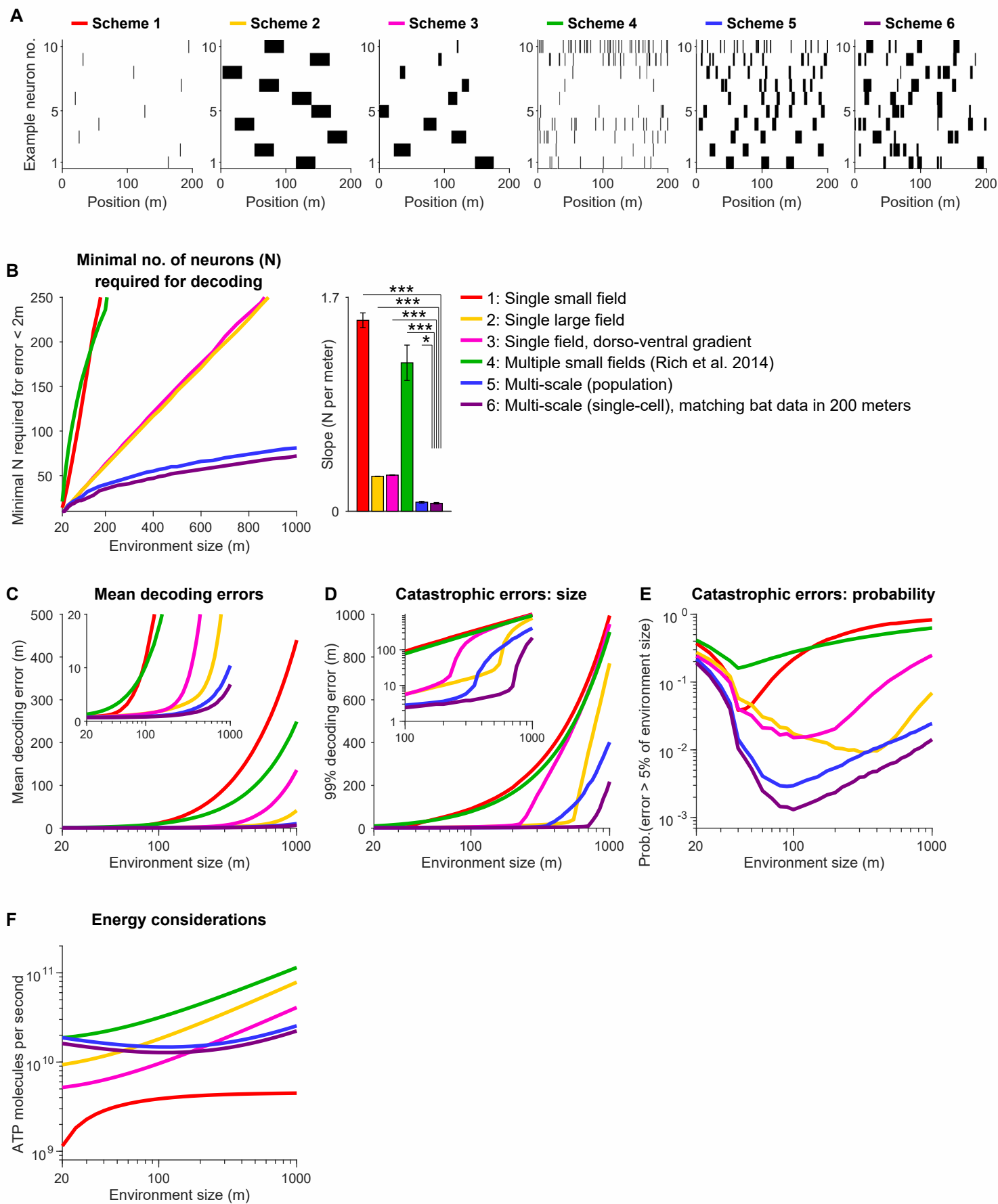
## F Population: Within-day dynamics is most prominent during the first 2 days, but occurs also later



Fig\_6



Fig\_7







## Supplementary Materials for

### **Multi-scale representation of very large environments**

### **in the hippocampus of flying bats**

Tamir Eliav<sup>1\*</sup>, Shir R. Maimon<sup>1\*</sup>, Johnatan Aljadeff<sup>1,2</sup>, Misha Tsodyks<sup>1,3</sup>, Gily Ginosar<sup>1</sup>, Liora Las<sup>1</sup>,

Nachum Ulanovsky<sup>1†</sup>

1. Department of Neurobiology, Weizmann Institute of Science, Rehovot 76100, Israel
2. Section of Neurobiology, Division of Biological Sciences, University of California San Diego, CA 92093, USA
3. The Simons Center for Systems Biology, Institute for Advanced Study, Princeton, New Jersey 08540, USA

\* These authors contributed equally to this work

† Corresponding author. Email: [nachum.ulanovsky@weizmann.ac.il](mailto:nachum.ulanovsky@weizmann.ac.il)

#### **This PDF file includes:**

Materials and Methods

Supplementary Text

Figs. S1 to S23

Table S1

Supplementary References

## Materials and Methods

### Subjects and behavioral setups

Eleven adult male Egyptian fruit bats, *Rousettus aegyptiacus*, were included in this study (weights 160–200 gr). Information on the 11 individual bats is summarized in Table S1. Prior to the start of experiments, all bats were housed for several months in a large vivarium: a  $5.3 \times 5.0 \times 2.9$  meter colony room with many enrichment items and dozens of other bats living communally (see photos of this room in fig. S16A). All the bats were then pre-trained for a few days in a large flight-room ( $5.8 \times 4.6 \times 2.7$  meters) to fly between two landing-balls that were similar to the balls used subsequently in the tunnel experiments; the goal of this pre-training was to get them used to flying between the balls and landing on them for food reward. All experimental procedures were approved by the Institutional Animal Care and Use Committee of the Weizmann Institute of Science.

Bats no. 1–5 (“dataset 1” in Table S1) were caught as adults in the wild (in Israel). Following pre-training in the flight-room, the bats were trained to fly continuous directed flights in a long tunnel (Fig. 1E), and to shuttle between two landing balls that were located at the two ends of the tunnel (see fig. S3A for example trajectories). Food (fruit) was available to the bats at the landing balls, and the bats could also land and rest there. The tunnel was uniformly illuminated (illuminance level: 5 lux). Tunnel dimensions were as follows: Length = 194 m (the linearized distance between the two balls was 185.3 m); Width = 2.30 m; Height at maximal point = 2.35 m (see Fig. 1E for top-view and Fig. 1H for the cross-section of the tunnel). The tunnel was composed of a long 140 m arm and a shorter 54 m arm, with a  $43^\circ$  smooth turn connecting them (Fig. 1E). The inverted V-shape of the tunnel’s ceiling was designed to channel the bats to fly at the center of the tunnel (Fig. 1H and fig. S3B-C). Along the tunnel we placed

13 landmarks (fig. S2), whose positions were fixed across all days and all bats. All these bats were well trained and familiar with the tunnel prior to the microdrive-implantation surgery (see Table S1 for training history). Following training, bats were implanted with a microdrive for electrophysiological recordings in dorsal hippocampal area CA1 (see below). Each experimental day started with a sleep session and ended with a sleep session (each sleep session lasting 10–15 min). For the sleep sessions, the bat was placed alone inside a small covered cage which was positioned in a quiet location inside the tunnel, on the floor. Data from bats no. 1–5 are shown in Figs 1, 2 and 3.

Bats no. 6–8 (“dataset 2”) were also caught as adults in the wild, and CA1 neurons were recorded while bats were flying back-and-forth between two balls located at the ends of a 6 meter portion of the tunnel; this short 6 m portion was blocked using curtains. Data from bats no. 6–8 in the 6-m short tunnel are shown in Fig. 4.

Bats no. 6–7 (“dataset 3”) were recorded in a 130 m blocked portion of the tunnel (part of the long arm), in the exact same manner as bats 1–5 (dataset 1). The only two differences were: First, these bats were pre-trained and recorded in a 6-meter blocked segment of the tunnel (bats no. 6–7 were two of the three bats described above for dataset 2). Second, we then recorded their CA1 neural activity from the very first exposure-day (‘day 1’) in the long tunnel – on day 1 we opened the blocking-curtain and allowed them to fly back-and-forth along the entire 130-meter length. On subsequent days we continued testing them in the 130 m tunnel in every session, with recordings lasting overall for >1 month. These data starting from day 1 are shown in Fig. 5.

Bats no. 9–11 (“dataset 4”) were born in the lab and raised in the enriched large colony room ( $5.3 \times 5.0 \times 2.9$  m) with many other bats and multiple enrichment items (fig. S16A). Upon reaching adulthood (age >18 months; note the longevity of this bat species is >20 years; weight

>170 gr for all these 3 bats), these lab-born bats were pre-trained in the flight room, and subsequently were trained in the 200-m tunnel, in the exact same way as bats no. 1–5 – and were then recorded also in the exact same way as bats no. 1–5 (same landmark positions, same experimental procedures, same localization system, etc.). The precise matching of training and recording conditions between the lab-born bats no. 9–11 and the wild-born bats no. 1–5 was done in order to allow comparing large-scale spatial representations in CA1 of lab-born bats versus wild-born bats. These comparisons are shown in Fig. 6.

### **Animal localization system**

The 3D position of the bat in the tunnel was tracked at a rate of 18.3 Hz or 14.2 Hz, using an ultra-wideband (UWB) radio-frequency-based localization system (BeSpoon Inc). This system used 14 antennas whose 3D positions were calibrated at a 1 cm accuracy by surveyors. The 14 antennas were located around the tunnel (Fig. 1F, red dots), and during recording sessions they were used to measure the distance to a mobile active radio tag that was mounted on the bat's head: The bat's position was estimated as the intersection of the spheres around each antenna, which represent the measured distances from the antennas to the mobile tag (Fig. 1F). A real-time server collected all the distance measurements from the antennas, and further processed the raw distance measurements to yield 3D localization in the reference-frame of the antenna-array.

Next we converted the data to the coordinate-frame of the tunnel. We first used the antenna array to calibrate the position of the entire midline of the tunnel (the tunnel's 'backbone'): This was done by slowly moving a mobile tag along the center of the tunnel (the midline) – which yielded the tunnel position in the coordinate-frame of the antenna-array, i.e. the same coordinate system used later for tracking the bats. Landmark positions were measured and calibrated similarly. We subsequently projected the measured bat positions onto this calibrated tunnel midline ('backbone').

To estimate the precision of the localization system in a moving-tag scenario, we did the following calibration (Fig. 1G). We rapidly slid a mobile tag multiple times along a taut thin wire (~10 m long) that was placed perpendicular to the tunnel, and measured the tag's position. Then, we calculated the transverse deviations of the tag position from the interpolated line that connected the two ends of the wire – whose positions were measured separately with high precision. These transverse deviations (transverse to the wire, which means parallel to the long axis of the tunnel) represent the measurement-errors of the localization system along the long axis of the tunnel – which is the direction of the bat's 1D flight. These errors were found to have a standard deviation of 8.9 cm (Fig. 1G) – two orders of magnitude better than the typical ~5–10 meter accuracy of GPS.

### **Surgery and neural recording techniques**

After training or pre-training, each bat was implanted with a four-tetrode microdrive (weight 2.1 gr), loaded with four tetrodes, where each tetrode was constructed from four strands of insulated wire (17.8  $\mu\text{m}$  diameter platinum-iridium wire or 12.7  $\mu\text{m}$  diameter nichrome wire) – as described previously (1-4). Some of the bats were implanted with a 16-tetrode microdrive (weight 3.4 gr). Tetrodes were gold-plated to reduce wire impedance to the range between 0.25–0.7  $\text{M}\Omega$  (at 1 kHz). The microdrive was implanted above the right dorsal hippocampus (3.0–3.6 mm lateral to the midline and 5.7–5.8 mm anterior to the transverse sinus that runs between the posterior part of the cortex and the cerebellum). Surgical procedures were similar to those described previously (1-4): We used an injectable anesthesia cocktail composed of Medetomidine 0.25 mg/kg, Midazolam 2.5 mg/kg and Fentanyl 0.025 mg/kg (5) – and subsequently added supplemental injections as needed, based on monitoring the bat's breathing and heart-rate. The microdrive was attached to the skull with bone screws, using a layer of adhesive (Super-Bond C&B) and then

dental acrylic; the craniotomy was then covered with an inert silicone elastomer (Kwik-Sil or Kwik-Cast). A ground wire was attached from the microdrive to a bone-screw that touched the dura in the frontal plate. Following surgery, the tetrodes were slowly lowered towards the CA1 pyramidal cell layer over a time period of 2–3 weeks; positioning of tetrodes in the layer was provisionally assessed by the presence of high-frequency field oscillations (‘ripples’) and associated neuronal firing, and was later verified histologically (fig. S1B). During recordings, a 16-channel or 64-channel wireless neural-recording device (‘neural-logger’) was attached to an Omnetics connector on the microdrive. Signals from all channels of all the tetrodes were amplified ( $\times 200$ ) and bandpass filtered (1–7,000 Hz), and were then sampled continuously at 29.3 kHz or 31.25 kHz per channel, and stored on-board the neural-logger. During subsequent offline processing, the neural recording was further high-pass filtered with 600 Hz cutoff for spikes – creating a spike bandwidth of 600–7,000 Hz – and then 1 ms spike waveforms were extracted using a voltage threshold.

### **Spike sorting**

Spike-sorting procedures were similar to those described previously (1-4, 6). Briefly, spike waveforms were sorted manually using Plexon Offline Sorter, on the basis of their relative amplitudes on different channels of each tetrode. Data from all sessions – the behavioral session and the two sleep sessions – were spike-sorted together. Well-isolated clusters of spikes were manually selected, and a refractory period ( $< 2$  ms) in the inter-spike-interval histogram was verified. Spike-sorting was done in consecutive time-windows, to allow for drift-correction of the spike clusters. We included only neurons that were stably isolated throughout the recording. In total we recorded 757 well-isolated CA1 neurons from the 11 bats, of which we further

analyzed only putative pyramidal cells with firing rate  $\leq 5$  Hz, which met behavioral-coverage criteria as described below ( $n = 624$  cells): see Table S1 for details on the four individual datasets. The main analyses in the paper (Figures 1, 2, 3) focused on dataset 1 – wild-born bats flying in the 200-meter tunnel: In this dataset, a total of 304 well-isolated cells were recorded from dorsal hippocampal area CA1 of five bats. We further considered here only putative pyramidal neurons ( $n = 248$ , based on mean firing-rate of  $\leq 5$  Hz along the entire recording [including both behavioral and sleep sessions]), and discarded putative interneurons ( $n = 56$ , mean firing-rate  $> 5$  Hz). Of those 248 neurons,  $n = 235$  cells met behavioral-coverage criteria (see below), and were considered for further analysis.

### **Extracting flights and computing firing-rate maps**

The bats' flight behavior was mostly restricted to a 1D narrow horizontal corridor at the middle of the tunnel (Fig. 1H, and fig. S3B-C). Therefore, all the analyses and statistical tests in this study were performed strictly on the basis of 1D firing-rate maps (projections on the long axis of the tunnel), as follows.

Location data from the localization-system were first processed to remove outliers (we removed data-points that were far away [ $>2$  m] from the tunnel's midline, or data with velocity higher than 20 m/s). We then linearized the data by projecting the valid positional data onto the long 1D axis of the tunnel (the tunnel's "backbone", which was measured using the radio-frequency localization tag, as explained above). We then filled short gaps where localization data were missing – which constituted a total of 3.1% of the data; this was done as follows: (i) Gaps of up to 1/3 second were linearly interpolated. (ii) Gaps between 1/3 second and 1.5 seconds were interpolated only if the effective velocities before, during and after the gap were similar (where

velocity during the gap was calculated as the distance between the data-points surrounding the gap, divided by the gap-duration). (iii) Larger gaps were not interpolated but rather extrapolated for 1/3 second from each side of the gap. These criteria and parameters for interpolating and extrapolating the missing data (which constituted only 3.1% of the total data) were chosen as follows: we conducted extensive simulations of gaps that were artificially added to real data that did *not* contain any actual gaps – and the criteria of interpolation and extrapolation were taken such that they yielded a *maximal* error of no more than 25 cm on average with respect to the original data points that were taken out in these simulations. Finally, 1D positional data were up-sampled to 100 Hz.

Firing-rate maps were constructed for flight periods only – separately for the two flight directions. Individual flights were identified by local peaks in the flight speed that had maximal-speed  $> 4$  m/s without changes in flight direction. To improve the accuracy in estimating flight speed, the bat's position was smoothed using a smoothing spline (*csaps.m* in Matlab), based on which the instantaneous speed was extracted. The beginning and end of each flight was taken as the time-point where the bat's speed crossed a threshold of 1 m/s. We included in further analysis only unidirectional flight-trajectories longer than 100 meters, and the spikes that occurred during these flight-trajectories.

To compute 1D firing-rate maps, we used fixed-sized spatial bins (20 cm) and collapsed the time-spent (occupancy) data and the spike counts onto the horizontal 1D dimension along the tunnel (linearized  $x$ -axis). We smoothed both the spike-count and time-spent 1D maps with a Gaussian kernel ( $\sigma = 2.5$  bins = 0.5 m), and then divided, bin by bin, the smoothed 1D spike-count by the smoothed 1D time spent. Only sessions with more than 10 long flights per direction were included for further analysis (see Fig. 1K for the distribution of the number of such long flights [ $> 100$  m] per direction). The exact same criteria, binning and smoothing were used also



for constructing maps in dataset 4 – lab-born bats flying in the 200 m tunnel, and in dataset 3 – wild-born bats flying from day 1 in a 130 m tunnel. For dataset 2 – the 6 m short tunnel – we included also slower flights (maximum speed  $> 2$  m/s without changes in flight direction), and used a 10-cm bin and a smoothing kernel of  $\sigma = 2$  bins for constructing firing-rate maps over 6 m.

### **Quantifying spatial coding, definition of place-cells, and defining place-fields**

To quantify spatial coding of the firing-rate map in each direction, we used the spatial information index (7), measured in bits/spike: spatial information per spike (7, 8) is equal to  $\sum p_i(r_i/r) \log_2(r_i/r)$ , where  $r_i$  is the firing-rate of the cell in the  $i^{\text{th}}$  spatial bin,  $p_i$  is the probability of the bat being in the  $i^{\text{th}}$  bin, and  $r = \sum p_i r_i$  is the overall mean firing-rate. We calculated the spatial information index also for spike-train shuffles. To shuffle the spike-train, we rigidly and circularly shifted in time the spikes of each flight, using a uniform random shift; the value of the shift differed randomly between individual flights, so each shuffle consisted of a unique set of temporal shifts that differed randomly across flights. We performed 1,000 such random shuffles. A cell was regarded as a significant place-cell in a particular flight-direction if the following criteria were met for that direction: (i) The cell emitted at least 50 spikes in-flight; (ii) Spatial information was  $> 0.25$  bits/spike; (iii) Spatial information was also  $> 99\%$  of the shuffles; (iv) The cell had at least one significant place-field (see next paragraph for place-field detection and significance).

To detect place-fields, we took the following steps. (1) First, we extracted local peaks in the firing-rate map, with a peak-rate of  $> 1$  Hz. (2) To remove small local peaks ‘riding’ on a large field, we searched for shallow ‘dips’, i.e. cases where the dip between two adjacent peaks was  $> 50\%$  of the firing-rate of the larger peak – and then disregarded the lower peak. (3) We then defined the boundaries of the field as follows. We identified the zone covering 20% of the peak firing rate of that place-field. Then, in order to overcome the smearing caused by the

smoothing of the firing-rate map, we defined the field size as the 5–95% percentile of the positions of the spikes that occurred inside the 20% zone (see fig. S4). The use of raw spikes for defining field sizes was done to enable the detection of very small fields, if they exist. (4) Field stability criterion: We required at least 5 different laps with spikes to have occurred inside the place-field, or 20% of the laps with spikes – whichever is larger. (5) Field significance criterion: In order to capture clear distinct fields, we treated a place-field as significant only if it had significant spatial information in its local area, near the place-field. To quantify this, we looked at the area surrounding the field (specifically, the field itself plus 50% of the field’s size in each direction). Focusing on this local area around the place-field, we calculated the spatial information in this local area for the real spikes and also for 1,000 shuffles (same rigid shuffling as above), and considered the field to be significant only if it had spatial information  $> 95\%$  of the shuffles in the same local area. (6) Finally, we considered place-fields only at locations where the flight-speed was high, away from takeoff and landing. For this we defined fixed takeoff- and landing-zones (fixed across all bats and sessions), where the flight speed was lower than 80% of the grand median flight speed over the entire tunnel – and removed any fields that were fully contained within these takeoff and landing zones (see Fig. 1I, gray areas). The flight speed in the valid area (excluding the takeoff and landing zones) was very constant (Fig. 1I,J).

For each neuron we computed five indices: (i) Spatial information, in bits/spike – as defined above (Fig. 2B). (ii) Sparsity ( $\delta$ ) (Fig. 2C), defined as  $\langle r_i \rangle^2 / \langle r_i^2 \rangle = (\sum p_i r_i)^2 / \sum p_i r_i^2$ , which is bounded between 0 and 1, with low values indicating high spatial selectivity. (iii) Total coverage of all the fields, defined as the sum of all field sizes per direction, normalized by the length of the flight-track excluding the takeoff and landing zones (Fig. 2D). (iv) Map correlation – an index of map stability – computed as the Pearson correlation between maps computed for odd versus even

flights (Fig. 2E). These four indices were computed separately for each flight-direction.

(v) Pearson correlation between the maps for the two flight-directions (directionality: Fig. 2F).

### **Within-day dynamics of place fields**

*Place-field detection in time-windows:* For the analysis shown in Fig. 5F, fig. S20J and fig. S23, we considered place-cells defined as above. For these neurons, we detected place-fields on a flight-by-flight basis, in order to measure within-session dynamics in place-fields. This was done as follows: First, we computed firing-rate maps for each flight using a 5-flight sliding windows, with 1-flight steps. Maps for each flight were computed similarly to the computation done for the entire session, except that here, since the maps were based on a smaller number of flights ( $n = 5$ ), we used a slightly wider Gaussian kernel for smoothing ( $\sigma = 3$  bins = 0.6 m). Second, we detected fields for each per-flight firing rate map, similar to the detection performed on the entire session, but with the following changes due to the sparser data: minimum number of spikes = 3; minimum flights with spikes = 2; overlapping fields were defined using a 20% criterion (instead of 50%) to avoid over-splitting of fields due to the sparseness of the data; and we did not use the local spike shuffling here. Third, we merged fields across different flights if their center-of-mass positions were spatially closer than their mean field size; in addition, to account for global drift across the entire session, we merged fields if the mean location of one field across all windows fell within the 25–75% percentiles of the edges of the other field, across flights. Fourth, we removed fields detected only in isolated windows, if that field was not detected in the 5 windows before and in the 5 windows after the current window. Further, fields that were active in less than 20% of the session's flights or in less than 5 windows were entirely removed, similar to our field-stability condition in the main analysis.

*Detection of changes in place-fields:* Three types of changes were detected:

- 1) Appearance/disappearance of fields: if a field did not emit any spikes in the first two flights or in the last two flight, we considered this field as appeared or disappeared, respectively. If a field fired zero spikes for  $\geq 5$  consecutive flights, and then resumed firing, we considered it as disappeared and then appeared again.
- 2) Change in field size: we looked for step-like changes in the field size during the session, as follows: (i) the change in field size (mean size before versus mean size after the change) was  $>5$  meters or  $>50\%$  of the field size – and in case of the 50% criterion, we also required a minimal change of  $>1$  meter in field-size; and (ii) there were at least 5 flights before and 5 flights after the change-point that were stable, i.e. no change was detected there. Then, if the field size increased, the new segment of the field was considered as appeared; and vice versa, if the field size was reduced, the missing segment was considered as disappeared.
- 3) Change in field location: we looked for step-like changes in field location during the session, as follows: (i) the change in field location (mean location before versus mean location after the change) was  $>5$  meters or  $>50\%$  of the field size – and for the 50% criterion, we also required a minimal change in field location of  $>1$  meter; (ii) there were at least 5 flights before and 5 flights after the change-point that were stable, i.e. no change was detected there; and (iii) the overlap between fields (before and after the change) was less than 50%. The field was then considered as disappeared from its old location (before the change) and appeared in the new location.

Examples of field detection dynamics are shown in fig. S23A.

## **Statistics**

Correlations were based on Spearman's correlation coefficient,  $\rho$ , unless stated otherwise (this nonparametric rank correlation was used because in many cases the data were not normally

distributed). We used the Kolmogorov-Smirnov test to compare distribution shapes. To assess the significance of the spatial tuning of place-cells, we compared the real data to spike-shuffled data (99<sup>th</sup> percentile), as described above. To compute the shuffled distribution for map correlations between the two flight-directions (Fig. 2F, black line), we computed all the map correlations between direction 1 in cell  $i$  and direction 2 in cell  $j$ , where  $i \neq j$  (cell shuffling). To compute the shuffled distribution of the distances between place-fields and landmarks (Fig. 3B, black lines), we randomly shifted the location of each field independently 10,000 times circularly along the tunnel. To compare proportions in Fig. 5F, we plotted error bars as the standard error of the proportion and used the two-proportion  $z$ -test.

## Histology

Histology was done as described previously (1, 9). In brief, at the end of recordings, the bats were anesthetized, and electrolytic lesions (DC positive current of 30  $\mu$ A, 15-s duration) were made to assist in the precise reconstruction of tetrode positions. The bat was then given an overdose of sodium pentobarbital and, with tetrodes left *in situ*, was perfused transcardially using 4% paraformaldehyde or 4.5% histofix. The brain was removed and thin coronal sections were cut at 30- $\mu$ m intervals. The sections were Nissl-stained with cresyl violet and were photographed to determine the locations of tetrode tracks in dorsal CA1 (e.g. fig. S1B, right). Positions of tetrode-tracks were then projected onto coronal plates of our stereotaxic brain atlas of the Egyptian fruit bat (10), and were also projected onto a 3D rendering of CA1, which we prepared based on our stereotaxic brain atlas (see 3D rendering in fig. S1A). Finally, we used these projections to estimate the tetrode-track position along the longitudinal axis and proximo-distal axis of CA1 (fig. S1B-left and S1C, and Fig. 6I; the borders of CA1 in the atlas were determined based on a combination of histological, immunohistochemical, and tract-tracing data from several dozens of bats).

## Compartmentalization model

Here we tested whether the statistics of field-sizes in the large-scale spatial maps in the bat can be explained by a scenario where the hippocampus is segmenting the tunnel into small independent segments (according to the landmark locations), wherein fields could be concatenated at the edges of the compartments (i.e., around the landmarks), thus creating larger fields. We considered each segment between landmarks in the tunnel as a separate, small-scale compartment. To model this, we generated compartmentalized maps using field statistics that we observed in the data, as follows: First, for each segment of the environment between two landmarks, we randomly drew the number of simulated small fields from a Poisson distribution. The rate of the Poisson distribution was chosen such that the average coverage of the compartmentalized maps was 0.15, to match the empirical average of the bat data in the 200 m tunnel (fig. S13, top row), or we set the rate of fields to match the empirical average number of fields in the data (fig. S13, bottom row). Second, each simulated field had its size drawn from a gamma distribution that was fitted to one of the following: (i) Fitted to the distribution of field-sizes measured in the small environment of 6 m (Fig. 4): this resulted in the following gamma-distribution parameters: shape parameter, 3.56; scale parameter, 0.37 m. This option was plotted in fig. S13, left column. (ii) Fitted to the data in the small 6-meter environment, as in (i), but scaled up to match the median inter-landmark interval. We used here the same scaling factor  $\delta = 0.3$  as in Figure 7 (see the next section in the Methods for more details). This option was plotted in fig. S13, middle column. (iii) Fitted to the distribution of the smallest place-fields per neuron in the large 200-meter environment. This option was plotted in fig. S13, right column. Third, within each segment, we drew randomly the locations of each field (uniform distribution), and their sizes (from the gamma distribution described above). Importantly, we allowed fields from one segment

to extend to the neighboring segment and merge together, to produce larger fields. Fields within the same segment were not allowed to overlap. We then compared these null model distributions of field sizes (fig. S13, cyan) with the experimental data distributions (fig. S13, gray bars).

### **Simulations of various spatial encoding schemes, and analysis of decoding errors**

We created populations of neurons with simulated place-fields, using 6 encoding schemes: These different schemes were aimed to compare coding by single-fields versus multiple-fields versus multiple-fields with a multi-scale code (see below). The comparison between the 6 encoding schemes was done by utilizing two decoders – a Bayesian maximum-likelihood decoder and a population-vector decoder (see below) – which we used here in order to study how the field numbers and distribution of field-sizes affect the accuracy with which an environment of size  $L$  is represented. Decoding was done with an integration time window of 500 ms (Fig. 7 and figs S17 and S18); qualitatively similar results were obtained when using different time-windows (fig. S19).

*Encoding.* In our simulations, the environments had a 0.2 m resolution (0.2 m bin size: as in our empirical firing-rate maps). We varied the environment-size  $L$  between 20–1000 m. To simplify the analysis, we neglected neuron-to-neuron variability in firing rates: In all cases we assumed that neurons fire with Poisson statistics independently from each other, with in-field firing rate of 10 spikes/second (when using integration time-window of 500 ms, see below). We considered 6 schemes for encoding position in the environment (see Fig. 7A):

Scheme 1: A single small field. Each neuron had one field of size 1 meter, located randomly in the environment (uniform distribution).

Scheme 2: A single large field. Each neuron had one field located randomly in the environment (uniform distribution); field size was  $0.15 \times L \times (200/L)^\delta$  meters, where  $L$  is measured in meters,

and the prefix 0.15 represents the average coverage of place-fields in our data for the 200 meter tunnel (see below). The coverage in scheme 2 (as well as in schemes 3, 4, 5, 6) was thus scaled with environment size as  $1/L^\delta$  – with  $\delta$  being a ‘scaling factor’ – as further explained below.

Scheme 3: A single field per neuron, with gradually increasing field size across the neuronal population – mimicking the dorso-ventral anatomical gradient of field sizes in the hippocampus (11). Each neuron had one field located randomly in the environment (uniform distribution). The field sizes linearly ranged from 1 meter up to  $0.15 \times L \times (200/L)^\delta$  meters, i.e. a linear progression from scheme 1 to scheme 2.

Scheme 4: Gamma-Poisson distribution of small fields, as described in ref. (12) – which is the only previous study that described quantitatively the distribution of the number of CA1 place-fields in a 1D environment. We randomly drew multiple fields for each neuron using the following steps (identical to the model in ref. (12)): (i) We randomly chose a field-propensity value from a gamma distribution with shape parameter 0.57 and rate parameter  $7.75 \times (L/50)^\delta$  m – the exact numbers reported in ref. (12). This ensured that at  $L = 50$  m (the approximate environment size in that study) the encoding was identical to the model of ref. (12) – but for other values of  $L$ , the coverage scaled as  $1/L^\delta$ , allowing a comparison to schemes 5, 6 below, which have the same scaling. (ii) We then randomly drew multiple field positions from a Poisson distribution with a rate equal to the field-propensity value of each neuron. All fields had a 1 m size. A neuron was accepted into the population only if it had at least one field.

Scheme 5: Multi-scale field size distribution at the population level – with multiple fields per neuron that all have a fixed field-size. We assigned a field size  $l_i$  for each neuron  $i$ , such that the field sizes of all neurons followed a gamma distribution with shape parameter  $\alpha = 3.16$  and scale parameter  $\theta = 1.8 \times (L/200)^\delta$  meters. These parameters were taken from the gamma-



distribution fit to the data (fig. S8); we opted to use the gamma distribution for the field-sizes, rather than the log-normal distribution, because a gamma distribution can be scaled naturally by changing the scale parameter  $\theta$ , unlike the log-normal distribution. The number of fields for each neuron was then taken as the rounded value of  $0.15 \times L \times (200/L)^\delta / l_i$  (the division by  $l_i$  ensured that for a given environment size  $L$ , the average coverage was the same for all neurons, regardless of each neuron's field-size). Field locations were randomly distributed along the environment, with no overlaps.

Scheme 6: Multiple fields per neuron, with a multi-scale distribution of field sizes at the single-neuron level – with all possible field-sizes per neuron. For each neuron, we picked field sizes randomly from a gamma distribution with shape parameter  $\alpha = 3.16$  and scale parameter  $\theta = 1.8 \times (L/200)^\delta$  meters, as in scheme 5 – and the number of fields was chosen such that the coverage, i.e. the cumulative size of all the fields together, reached  $0.15 \times L \times (200/L)^\delta$ . Field locations were randomly distributed along the environment, with no overlaps.

Schemes 5v and 6v: These are variations of schemes 5 and 6, which have variable coverage across neurons that captures the full coverage-distribution of the data. We first fitted the coverage distribution of the neurons recorded in the 200 m tunnel (dataset 1) with an exponential distribution (fig. S17F). Then we created maps as in the original schemes 5 and 6, except that we iteratively added fields until a random target coverage (drawn from the fitted exponential distribution) was reached. Similar to the original schemes 5 and 6, also here the coverage was scaled with the environment size as  $1/L^\delta$ .

For all schemes, fields were positioned uniformly and randomly in the environment. To avoid distorting the uniform distribution of fields near the boundaries of the environment, we allowed fields to be located anywhere and be truncated at the boundaries. In order to account for

the sub-linear increase in field-sizes as a function of the environment size (which has been reported in previous rodent experiments (13)), and the decrease in coverage as a function of environment size, we did the following: In schemes no. 2–6 the relative total coverage (the average fraction of the environment covered by the fields of each neuron) was decreased as  $\sim 1/L^\delta$  – with  $\delta = 0.3$ , where the value 0.3 was fitted from the experimental data (see below for further details). Likewise, in schemes 2,3,5,6 the mean field-size was increased as  $\sim L^\delta$  (as a function of the environment size  $L$ ) – also with  $\delta = 0.3$ . Note that, in schemes 2, 3, 5, 6, the pre-factor 0.15 represents the average coverage at the environment size of our experiments (200 m). In schemes 4, 5 and 6, which had multiple fields per neuron, the fields of the same neuron were not allowed to overlap.

To fit the scaling factor  $\delta$  based on the experimental data, we used the average coverage  $\bar{\phi}$  and average field size  $\bar{l}$  from the data recorded at two different environment-sizes  $L$ : the large-scale environment (dataset 1: the 200 m tunnel) and the small-scale environment (dataset 2: the 6 m tunnel). That is, we used:  $\delta = \frac{1}{2}(\delta_l + \delta_\phi)$ , where  $\frac{\bar{l}_1}{\bar{l}_2} = (\frac{\bar{L}_1}{\bar{L}_2})^{\delta_l}$  and  $\frac{\bar{\phi}_1}{\bar{\phi}_2} = (\frac{\bar{L}_1}{\bar{L}_2})^{-\delta_\phi}$ . This calculation gave scaling factors of  $\delta_l = 0.36$  and  $\delta_\phi = 0.24$ , yielding a mean scaling factor of  $\delta = 0.3$ , which was subsequently used in all our analyses. In fig. S17H we further explored a wide range of values for the scaling factor  $\delta$ .

We denote each neuron’s spatial selectivity map by  $f_{a,i}(x)$ , where  $i$  is the neuron index ( $i = 1, \dots, N$ ), and  $a$  is the scheme index ( $a = 1, \dots, 6$ ).  $f_{a,i}(x)$  is equal to 1 if the neuron has a field in position  $x$  and 0 if it does not – that is, the field shapes in our model were taken to be rectangular (see examples in Fig. 7A).

*Generating spike counts.* We assumed that the animal starts each iteration of the simulation (each ‘simulation-trial’) at a random position  $x = x_0$ , and flies at velocity  $v = 8$  m/s (the typical flight-speed we measured empirically) for a time interval  $\Delta t$ . The expected spike count of the neuron during that

trial is given by:  $m_i = \frac{m_0}{v\Delta t} \int_{x_0}^{x_0+v\Delta t} f_{a,i}(x)dx$ , where  $m_0$  is the expected spike count if the animal spent the entire interval within a field. We used  $m_0 = 5$  in all our simulations (taken together with the integration time window of 500 ms, this gives a 10 Hz in-field firing rate). The actual spike count in each trial was drawn from a Poisson distribution with rate  $m_i$ , and is denoted below as  $n_i$ .

*Decoding.* We considered two decoders:

Population Vector (PV) decoder: The classical PV decoder (14, 15) was adapted to the case where the stimulus space (i.e., the environment) is not circular, and where neurons can represent more than one location. In each trial, for each scheme  $a$  we computed the following sum over the  $N$  neurons:

$$A_{PV}(x) = \sum_{i=1}^N n_i f_{a,i}(x)$$

The decoded location was then taken as the one that maximizes  $A_{PV}(x)$ .

Maximum Likelihood (ML) decoder: Here we computed the log-likelihood of each neuron's spike count, and summed over the  $N$  neurons (15):

$$A_{ML}(x|\{n_i\}) = \sum_{i=1}^N n_i \log[m_0 f_{a,i}(x)] - m_0 \sum_{i=1}^N f_{a,i}(x)$$

Where the term on the left hand side denotes the log-likelihood of the bat being in position  $x$  given the observation of a vector of  $\{n_i\}$  spikes in each of the neurons  $i$ . The first term on the right hand side corresponds to a sum of spatial tuning of all neurons, weighted by their activity (similar to  $A_{PV}$ ). The second term on the right hand side corresponds to a correction for unequal coverage of the neuronal representation in different locations. This expression is an approximation of the likelihood function, where the decoder knows each neuron's firing-rate map (i.e.,  $f_{a,i}(x)$ ), but it does not rely on continuously computing a convolution of the firing-rate map with the animal's motion. Again, the decoded location was then taken as the one that maximizes  $A_{ML}(x|\{n_i\})$ . Note

that, unlike the PV decoder, the ML decoder accounts for the fact that if the spike-count is low, the animal is more likely to be in a place that is less well covered by the spatial representation – so in this sense, the ML decoder is better than the PV decoder – which is why we used the ML decoder for the main analyses (Fig. 7), and the PV decoder in the supplementary (fig. S18).

Fig. 7 and figs S17–S19 show results from  $10^6$  simulation-trials generated by drawing random field locations 4,000 times, then drawing random spike counts from the Poisson distribution 10 times, and then performing decoding at 25 equally spaced locations spanning the entire environment ( $4,000 \times 10 \times 25 = 10^6$ ).

To estimate the energy expenditure (number of ATP molecules per second) that is required to represent the environment with a mean error of less than 2 meters (Fig. 7F), we used the following formula:

$$\frac{ATP}{s} = coverage \times firing\ rate \times N_{required\ neurons} \times N_{\left[\frac{ATP}{spike}\right]}$$

Where coverage is the proportion of area covered by fields in each scheme; in-field firing rate is 5 spikes/s (the average in-field firing rate in our data: see fig. S6B); the number of required neurons is taken from the linear fit to the data in Fig. 7B; and  $N_{\left[\frac{ATP}{spike}\right]} = 600 \times 10^6$  is the number of ATP molecules required to generate one spike: this number was taken from ref. (16).

### Attractor-network model

We developed a network model of multiple interacting continuous attractor networks, at different scales, which randomly shared neurons between them. This model comprised  $N = 4,000$  neurons, with  $P = 8$  continuous attractor neural networks (CANNs) embedded, each covering overlapping portions of the environment of  $L = 400$  spatial bins. Each bin represents 0.5 m of the

tunnel, resulting in a total tunnel-length of 200 meters, as in the experimental data. One attractor covered the entire environment, two intermediate attractors covered half of the environment each, and finally five smaller attractors covered consecutive fifths of the environment (see fig. S20A). Each CANN was modeled as a one-dimensional chain of neurons with Mexican-hat connectivity and open boundary conditions (17, 18).

We assigned each neuron to several CANNs, at random positions, as follows: for each CANN, a random sample of  $f=0.3$  of all the neurons were recruited (i.e., a random choice of 1,200 out of 4,000 neurons for each attractor). Each neuron could participate in multiple CANN's; the locations of the same neuron were independent between the different CANNs. The connection strength between each pair of neurons is the sum of contributions from each CANN to which both of the neurons belong. In particular, if neurons  $i$  and  $j$  both belong to a set of CANNs  $\{P\}$ , the connection strength between these neurons is given by:  $J_{ij} = \sum_{p \in P} J_{ij}^p$

Where  $J_{ij}^p = J_1 e^{-\frac{|x_i^p - x_j^p|}{l^p}} - J_0$ , and  $x_i^p$  stands for the positional label of neuron  $i$

( $i = 1, \dots, N$ ;  $0 < x_i^p < L$ ) in the corresponding  $p$ 'th CANN, chosen randomly as explained above;  $l^p$  is the interaction radius of the corresponding CANN. The dynamics of the network were controlled by the following equations for the synaptic current of each neuron,  $h_i$ :

$\tau \frac{dh_i}{dt} = -h_i + \sum_j J_{ij} g(h_j) + I_b + I_i^{pos}(t)$ , where  $g(h)$  is a neuronal gain function that has a threshold-linear form ( $g(h) = h$  for  $h > 0$ , and  $0$  for  $h < 0$ );  $I_b$  is a uniform background input; and  $I_i^{pos}(t)$  is position-dependent input to a neuron  $i$  at time  $t$ , which is determined by the position of the simulated animal at that moment, and was calculated as a sum of contributions

from each CANN to which a given neuron belongs:  $I_i^{pos}(t) = \sum_p I_1 e^{-\frac{|x_i^p - pos(t)|}{l^p}}$ , where  $pos(t)$

is the current simulated position, moving from left to right at a constant speed of 10 m/s.

A phase diagram of a single CANN was computed in ref. (19). In particular, for the CANN to be in the regime of a spontaneous generation of a bump of activity, the strength of recurrent excitation has to be big enough ( $J_1 > 0.5$ ). When multiple CANNs with overlapping neuronal assignments are embedded in the network, there is a range of parameters for which all of them are in the regime of spontaneous bump generation. In the simulations presented here (see fig. S20A-C and fig. S21), we used the following parameter values:  $J_1 = 0.7$ ;  $J_0 = 0.15$ ;  $\tau = 0.01\text{sec}$ ;  $I_b = 0.1$ ;  $I_1 = 0.05$ ; the interaction length  $l^p$  for each CANN  $p$  was chosen to be 0.05 (5%) of the size of the area covered by this CANN (i.e. 10 m for the largest 200-meter CANN, 5 m for the two intermediate 100-meter CANNs, and 2 m for the five smallest 40-meter CANNs).

We note that this model is fundamentally different from previous models that used multiple attractors for different environments, where only one attractor was active at any moment (18, 20), and also fundamentally different from models using non-randomly shared neurons (21).

### **Feedforward models**

*Input.* We generated four types of hypothetical input neurons that project to a CA1 neuron:

Model 1 – single-field CA3: Here each input neuron had one field, with field-size drawn from a gamma distribution fit to the data: shape parameter = 3.16, scale parameter = 1.8 meters (as in fig. S8). The field was positioned uniformly at a random location in the environment.

Model 2 – multi-field CA3: Here each input neuron had multiple fields such that the total coverage of the environment was 0.15. These spatial maps were generated as the maps in scheme 6 in Fig. 7.

Models 3 and 4 – periodic MEC: Our model consisted of 5 modules with grid spacings that spanned a small range relative to the size of the environment – following theoretical models of optimal grid-cell encoding of large environments (22). The periods we used were:

$5 \times [1, \sqrt{2}, \sqrt{5}, \sqrt{13}, \sqrt{23}]$  meters. First, we generated two-dimensional periodic hexagonal profiles for each module. Then, the one-dimensional (1D) spatial maps of MEC inputs were taken as a slice through the two-dimensional (2D) maps described above (similar to ref. (23)). The angle of the slice was identical for all modules, in agreement with ref. (24). The slice angle was varied from  $0^\circ$  to  $29^\circ$  in  $1^\circ$  jumps. The slice phase (i.e., the position of the start of the slice) varied uniformly at random for each input neuron. For the analyses in fig. S20 (Model 3) we used a  $0^\circ$  slice angle – corresponding to precisely-periodic 1D grid cells. For the analyses in fig. S22 (Model 4) we used all slice angles – corresponding to angled 1D slices through a perfect 2D grid (23).

All spatial maps were binary, i.e., had a firing-rate of 1 for bins inside a field and 0 outside a field. We used spatial bins of 0.2 m, and the length of the environment was 200 m – as in the data. For each input-model (single-field CA3; multi-field CA3; periodic MEC at 30 different slice angles) we created a bank of 2,000 input neurons, as explained above. For the MEC model, each of the 5 modules had 400 neurons.

*Output.* To generate the spatial map of an output neuron in CA1 we did the following. First, we chose 100 input neurons randomly, and assigned a random synaptic weight to each, drawn from a log-normal distribution with parameters  $\mu=1$  and  $\sigma=1$ . For the MEC model we ensured there were 20 inputs from each module. Second, we computed the weighted sum of inputs in each position, and smoothed it by computing a 4-m window moving average (equivalent to 500 ms given a flight-speed of 8 m/s). This smoothing was done to eliminate high-frequency fluctuations in the input to CA1, stemming from the binary nature of the inputs in the model. Smoothing the input is further justified in this model because without it, the CA1 output neurons of the model would have many more very-small fields ( $<1$  m) than observed in the data. Third, we picked a target coverage for the output neuron from an exponential distribution with mean 0.15, to match the coverage distribution

of the experimental data (see fig. S17F). Then, we computed a threshold such that the fraction of the smoothed weighted sum of inputs which is above the threshold is equal to the randomly drawn value of the coverage. The output spatial map of the CA1 neuron was then set to 1 or 0 where the smoothed weighted sum was above or below the threshold, respectively.

*Combining CA3 and MEC inputs.* We studied (in fig. S20G-H and fig. S22E-G) a model where a fraction of the 100 inputs are from Model 1 ‘single-field CA3’ neurons, and the remaining are from Model 3 ‘periodic MEC’ neurons – keeping a total of 100 input neurons per output neuron in CA1. We varied the fraction from 0 (only single-field CA3 inputs) to 1 (only periodic MEC inputs). The output maps were then computed from the inputs as described above.

*Perturbation.* To model the dynamic changes of spatial maps on a flight-by-flight basis, we introduced a perturbation to CA1 spatial maps for the three main types of inputs described above (input models 1, 2, 3), by randomly modifying a small fraction of the input synapses, as follows. In addition to the original CA1 map as described above, we computed a perturbed map by randomly re-drawing a small fraction of the 100 synaptic weights (4% of the synaptic weights were re-drawn in the simulations shown in fig. S23B; synaptic strengths were re-drawn from the same log-normal distribution of synaptic strengths as before). The output was computed using the same threshold as before the perturbation. By comparing the original and perturbed maps, we defined two types of map-segments: (i) appeared: map segments in which the output neuron was not active in the original map and was active in the perturbed map; and (ii) disappeared: map segments in which the output neuron was active in the original map and was not active in the perturbed map. Two (or more) segments of the same type that overlapped with the same field in the original map were defined as a single appeared/disappeared segment.



**Data and code availability**

All the behavioral and neural data in this study were analyzed using custom code written in Matlab; the modeling work was also carried out in Matlab. The data and code that support the conclusions of this study are available from the authors upon a reasonable request, and are also accessible online at Zenodo (see link in the Acknowledgments).

## Supplementary Text

### Neural network modeling of multi-scale codes: Attractor networks and feedforward models

Classical models of hippocampal place-cells are characterized by a single spatial scale per neuron in a given environment (17, 18, 20, 25-30). We looked for mechanistic neural-network models that could generate the multi-field multi-scale code that we observed. We considered two types of models. First, we examined this in the framework of a continuous attractor neural network. Modeling of spatially-tuned cells (and also other types of tuning, e.g. in sensory systems) is often done using a 1D continuous attractor network, in which cells with similar response properties have strong excitatory connections, together with a global feedback inhibition (i.e. Mexican-hat connectivity) (17-20, 27, 30, 31). This model design enables generating strong and reliable network activity from a weak and noisy spatially-modulated input, in the form of a single activity-bump with a fixed width. The tuning of single-cells in such networks exhibits a single-field per neuron, with a fixed field-size (determined by the width of the lateral excitation that sets the width of the network bump of activity) – which is very different from the multi-scale tuning properties in our bat data. We therefore asked whether we could generate a multi-field multi-scale code in single neurons, by using multiple interacting attractors – specifically, multiple attractors at different scales that randomly share a fraction of the neurons between them – and in particular we asked whether this network could maintain a stable bump of activity in each of the attractors. We generated 8 attractors spanning 3 different scales, with the largest attractor spanning the entire 200-meter tunnel and the smallest attractors each covering one fifth of the tunnel (fig. S20A). Each neuron could randomly participate in any of the attractors, and interact with the other neurons in those attractors according to the scale of each attractor (see Materials and Methods) (fig. S20A, red neuron participates in attractors no.

A4,5,6,8, and is interacting with neighboring neurons at distances proportional to the attractor scale). Simulations of this model displayed coherent bumps of activity that followed the simulated animal position and exhibited different bump-width for the different attractor scales (fig. S21A-B). Single neurons had multiple fields, with positions and sizes corresponding to the set of attractors they belong to — thus exhibiting multi-field multi-scale coding (fig. S20B – examples; fig. S20C – population). The fields showed a *continuum* of sizes (fig. S20C, top-right distribution), despite the fact that the underlying individual attractor networks had discrete scales (fig. S20A). By contrast, simulations of a model of 8 independent attractors (with no shared neurons) showed single fields for each neuron (fig. S21C-left), with a highly-discretized distribution of field sizes (fig. S1C-right: only 3 field sizes across the population).

Our multiple-attractor modeling results have several implications: (i) We identified a novel regime whereby all the interacting attractors generate coherent coexisting activity bumps, all being active simultaneously, resulting in a multi-field multi-scale code – as in the bat data. This suggests that our experimental data are compatible with the framework of continuous attractor networks. (ii) This model can also explain mechanistically the difference between single-field coding in the small environment, versus the multi-field multi-scale code found in the large environment: The hippocampus might allocate only one attractor for small environments – thus creating a single-field code, while in larger environments the hippocampus may allocate many more attractors – thus creating multiple fields for each neuron, with each field having a different scale (as in fig. S20A-C). (iii) Our network model yields a *continuum* of place-field sizes (fig. S20C, top-right), which is due to the interactions between the overlapping attractors, that effectively introduce noise (fig. S21A-B). This continuum is very different from the case of independent attractors, which invariably generate a highly-discretized set of field-sizes (fig.

S21C, right) – not a continuum. (iv) We believe that the key features of our model – random sharing of neurons between multiple attractors, and superposition of multiple activity bumps – could be generic also to other brain regions for which continuous attractors were proposed to underlie their function (32-34).

Second, we explored the possibility that multi-scale coding in CA1 results from feedforward connections coming into CA1 from CA3 and medial entorhinal cortex (MEC) (see Materials and Methods). We considered four types of feedforward inputs (fig. S20D and fig. S22A-B): (i) CA3 neurons with single-field per neuron and different field sizes across neurons (fig. S20D, left); (ii) CA3 neurons with multiple fields of different sizes per neuron (i.e. multi-field multi-scale coding being present already in CA3; fig. S20D, middle); (iii) MEC neurons with periodic grid-fields (fig. S20D, right); and (iv) MEC neurons whose firing in 1D is captured by a straight line passing through a perfect 2D grid at a certain angle and phase (fig. S22A) – a 1D slice through 2D – as proposed by a previous study (23). We then generated 1,000 output CA1 neurons, each connected randomly to 100 input CA3 or MEC neurons, with different synaptic strengths; we have set a firing-threshold such that the overall coverage of fields across the population matched the experimental data (see Materials and Methods). All four models qualitatively captured the basic multi-scale properties of CA1 (fig. S20E and fig. S22C – examples, fig. S20F and fig. S22D – population; the models yielded somewhat higher field-size ratios than in the data). Next, to test the viability of the two MEC-input models, we reasoned that if the MEC input neurons are periodic, then the output neurons in CA1 should show a signature of periodicity that is inherited from the input (35). We created a family of models with weighted inputs from CA3 and MEC, which showed that the stronger is the input from MEC, the larger are the spectral peaks of the output maps in CA1; this was true both for MEC inputs which

consisted of perfectly periodic 1D grid cells (fig. S20G-H) and for MEC inputs taken as 1D slices through a 2D grid (fig. S22E-G). By contrast, *no* spectral peaks were found when we examined the spectra of the spatial firing-rate maps for the experimentally-recorded place-cells (200 m tunnel) – neither when pooling across all place-cells (fig. S20I), nor in individual animals (fig. S22H) – indicating a lack of spatial periodicity in the multi-field firing of bat CA1 cells. This is consistent with our finding of an exponential distribution of gaps between fields (Fig. 3C), which also argues against any spatial structure. We therefore predict that *non*-periodic activity will be found in MEC neurons in large-scale environments; or alternatively, the inputs from CA3 are much more dominant than MEC inputs in setting CA1 activity – consistent with recent findings showing that CA3 is the predominant driver of CA1 place-cell activity (36).

Next, because our spectral analyses argued against the MEC-based feedforward models, we proceeded to examine the CA3-based feedforward models. Specifically, we considered the appearance/disappearance of place-fields, which we observed in the data (Fig. 5E-F), and modeled this field-dynamics via plasticity of CA3-CA1 synapses (see Materials and Methods; we also modeled via plasticity in MEC-CA1 synapses). We reasoned that different CA3 feedforward models may yield different patterns of change in CA1 upon a simulated perturbation of CA3-CA1 synapses: Intuitively, in models with multiple fields in each input-neuron (e.g., multi-field multi-scale CA3 model, but also MEC-based models), synaptic perturbations should show concurrent changes in multiple fields of the output CA1 neuron – while models with single-field inputs (single-field CA3 model) should exhibit independent dynamics in different fields, and therefore show lower probability of concurrent changes in several fields (fig. S23B). The experimental data were most consistent with the single-field CA3 model (fig. S20J and fig. S23B-C). Taken together, we conclude that the feedforward model that is most consistent with

the data is single-fields in CA3. Notably, this prediction sets up a puzzle, because our own decoding analysis (Fig. 7) showed that single-field codes are not efficient for representing large environments – which should apply also to CA3; this may possibly point to different coding objectives in CA3 versus CA1 (37-39). It is therefore important to conduct future recordings in CA3 and MEC in very large environments, in order to resolve this puzzle regarding CA3 – and also to test our prediction that the coding of MEC neurons in very large environments is unlikely to be periodic.

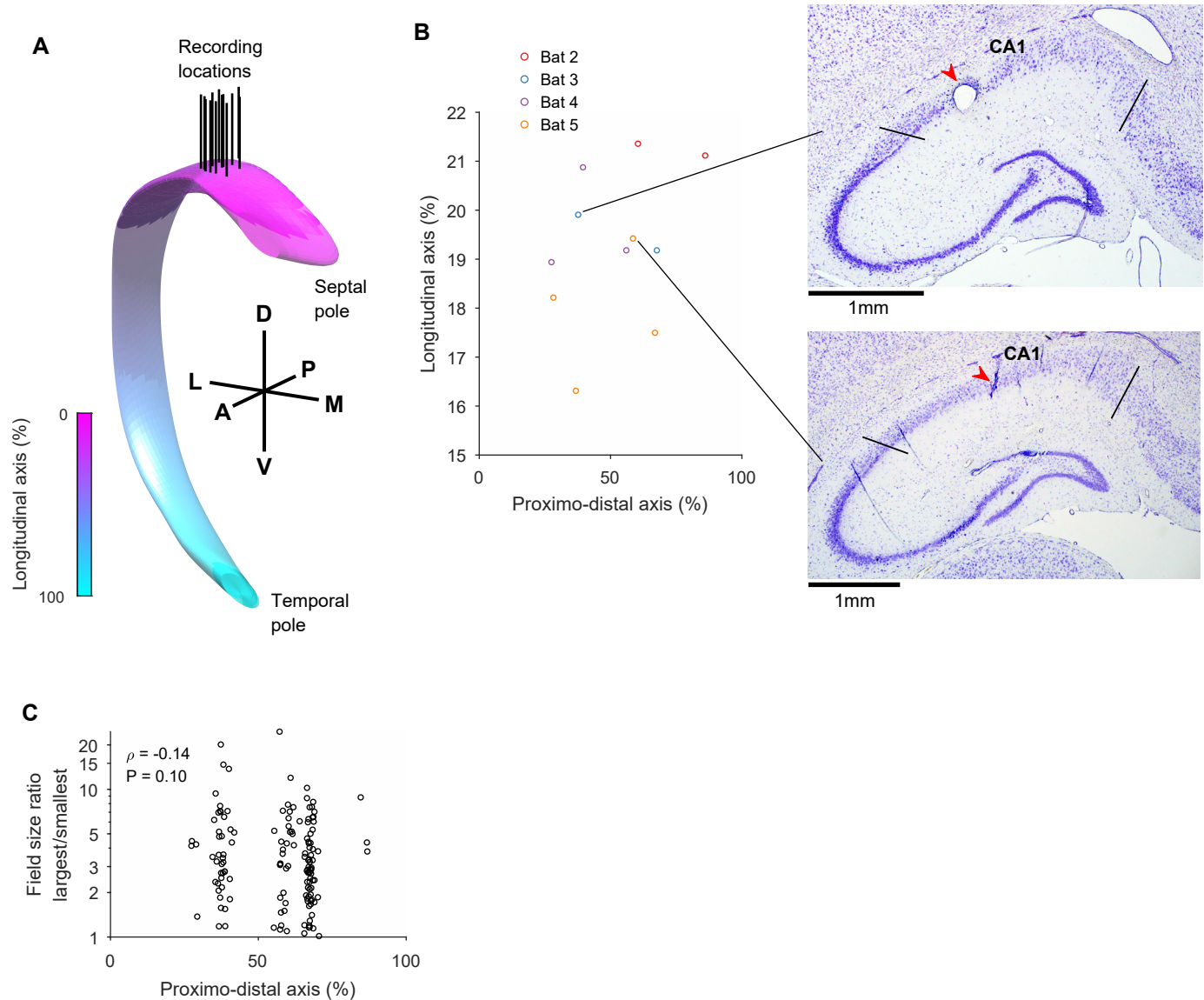
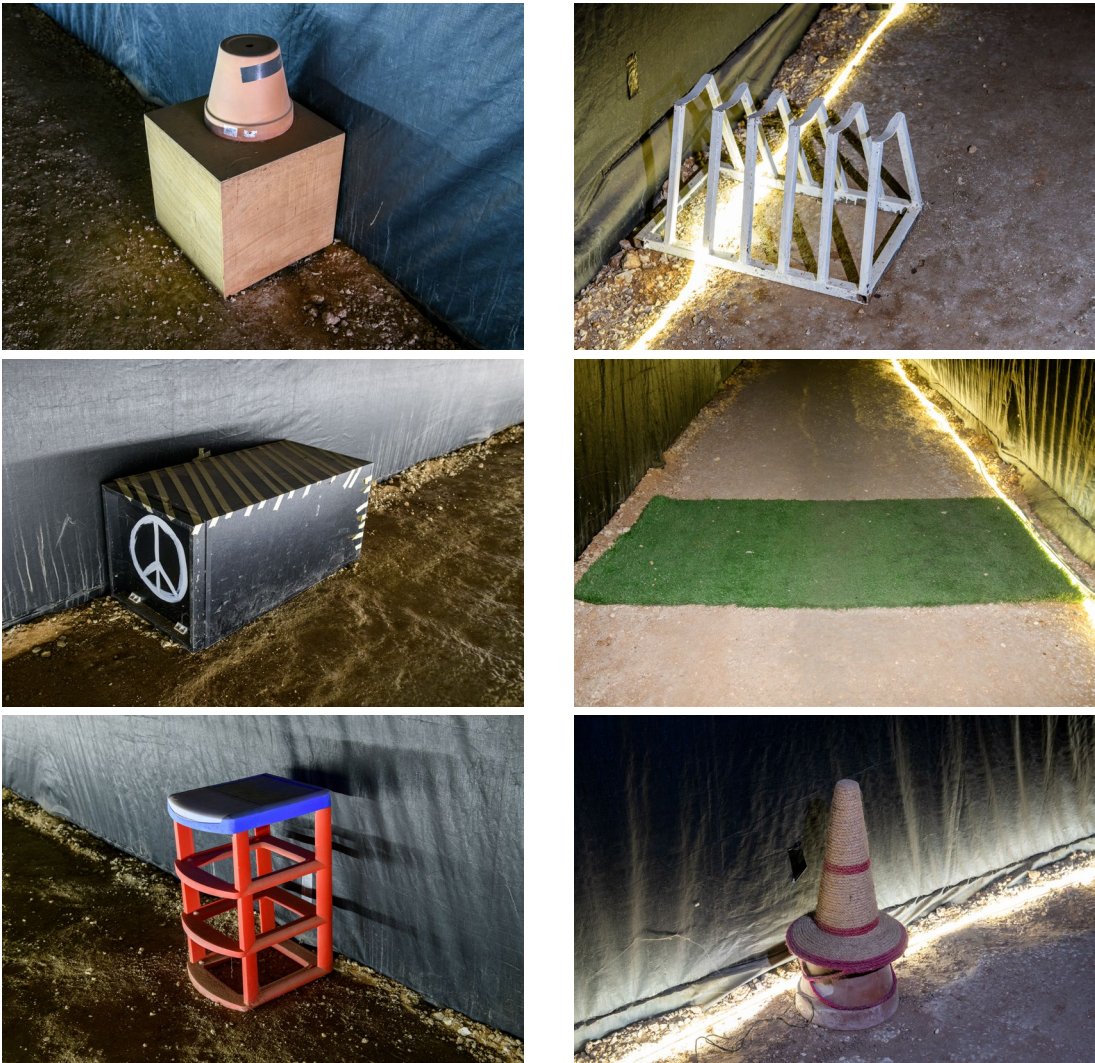


**fig. S1. Anatomical reconstruction of tetrode positions.** (A) 3D reconstruction of the CA1 sub-region of the bat hippocampus, showing the entire dorso-ventral (septo-temporal) longitudinal extent of CA1. Black lines labeled 'recording locations' mark the locations of all our identified tetrode-tracks in CA1, for the bats in dataset 1 (wild-born bats flying in the 200-m tunnel); all of them were located in dorsal CA1. The 3D axes represent the cardinal directions in the brain (A, Anterior; P, Posterior; M, Medial; L, Lateral; D, Dorsal; V, Ventral); each line in the 3D axes represents a 2 mm scale bar (e.g. from M to L is 2 mm). (B) Left: Anatomical position of tetrode penetrations along the CA1 longitudinal axis and proximo-distal axis; colored separately for each bat (bat numbers are indicated; one of the bats [bat 1] is missing here [as well as in the other panels] because we did not have precise anatomical localization for the tetrode tracks of this bat, due to damaged histology). Note that all the tetrode tracks were in dorsal CA1 (all were around the 20% most septal part of the longitudinal axis of CA1); the tetrode tracks were mostly distributed around the middle portion of the proximo-distal axis of CA1. Right: Two histology sections from two different bats, showing examples of recording sites. Red arrowheads indicate lesion (top) or track (bottom). Black lines indicate the proximal and distal borders of CA1. (C) Scatter of field size ratio for recorded place-cells versus the proximo-distal location of the tetrode from which the cell was recorded. No significant correlation was found between the anatomical location and the functional multi-scale property (Spearman correlation:  $\rho = -0.14$ ,  $df = 142$ ,  $P = 0.10$ ). Dots were slightly jittered along the proximo-distal x-axis, for display purpose only (Gaussian jitter with s.d. = 1%; the correlation was computed without the jitter). Note that most tetrodes were located in the intermediate part of CA1 and did not span the entire proximo-distal axis – i.e. we did not have any CA1 recordings that were very close to CA2 (very proximal) or very close to the Subiculum (very distal).



A



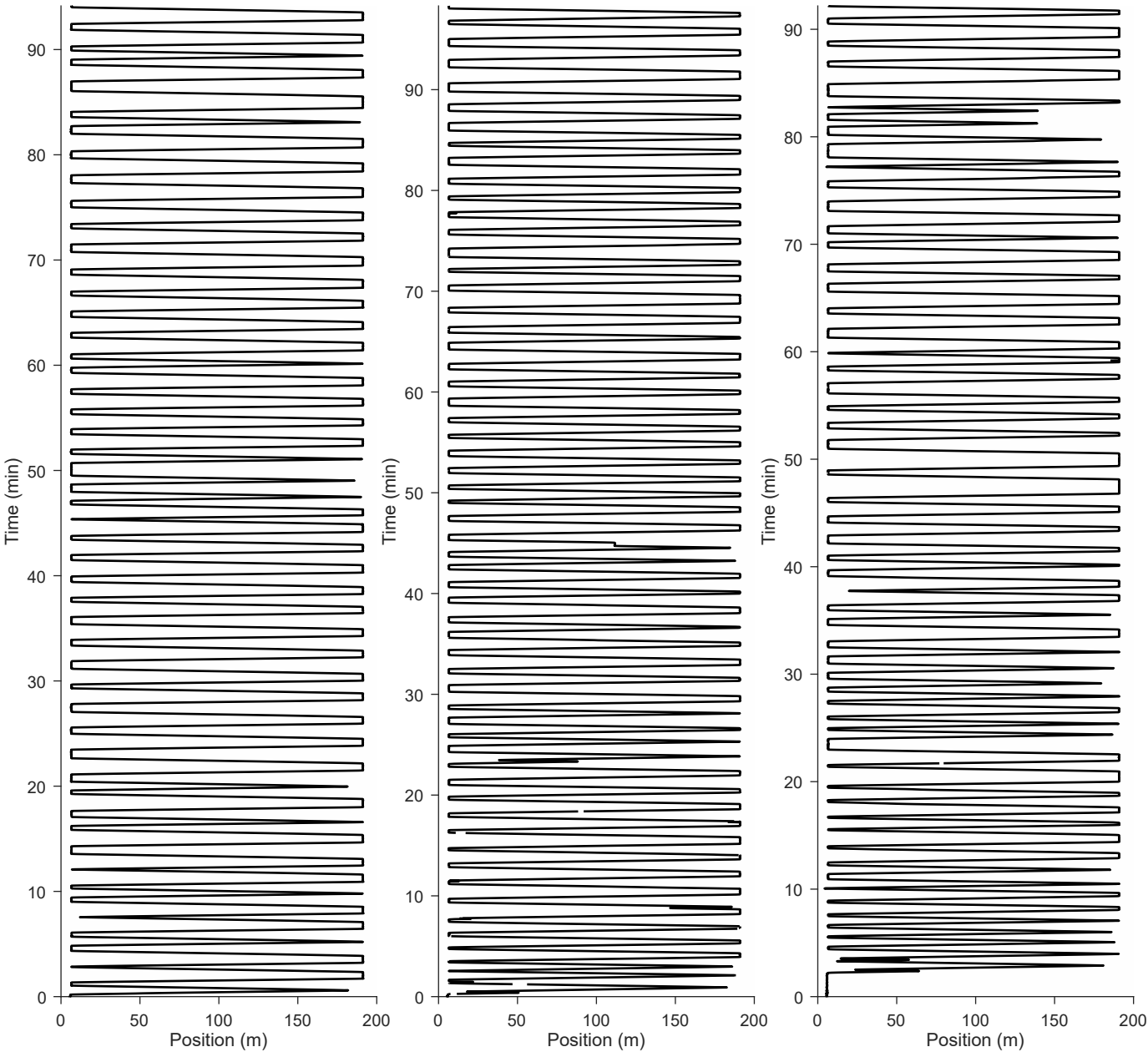
B



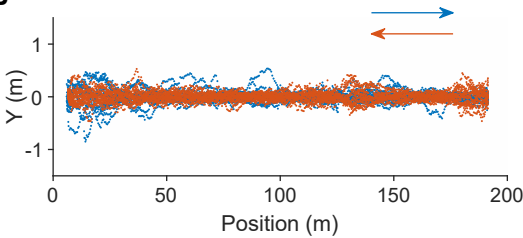


**fig. S2. Landmarks in the tunnel.** (A) Examples of six different landmarks that were placed along the tunnel. (B) Photograph taken in the middle of the tunnel, at about the same height as the bats flew – showing that several landmarks are visible simultaneously. The three landmarks seen here are the three landmarks shown in the left column of panel A. Note that these photographs were taken with long exposure and with complementary flash-lights, for clarity; the actual light levels we used in the experiments (5 lux) were lower than this – but they were bright enough to enable bats (and humans) to see the landmarks very clearly, including seeing several landmarks simultaneously ahead of the bat.

**A**



**B**



**C**

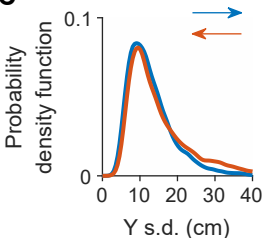


**fig. S3. Bats flew in the tunnel in narrow one-dimensional stereotypical flight trajectories.**

(A) Examples from 3 recording sessions, showing the full behavioral coverage during the session: plotted are the bats' position along time in the session, demonstrating that the bats flew many times back-and-forth between the two landing balls. (B and C) The bats exhibited only small lateral deviations in the tunnel (perpendicular to the tunnel's long axis) – i.e., they flew largely in the center of the tunnel (see also Fig. 1H). (B) Example session: plotted are the lateral deviations (Y-axis) of the bat location from the mean location along the tunnel. Blue and red colors show the two flight directions (see arrows). (C) Population summary: Distribution of the standard deviations of the bats' positions in the Y-axis ('Y s.d.'), pooled across all positions in the tunnel, for all the sessions of all the 5 bats. Note the deviations in the Y direction were quite small (typically < 20 cm). Only full (>100 meter) unidirectional flights were analyzed here – and throughout the paper.

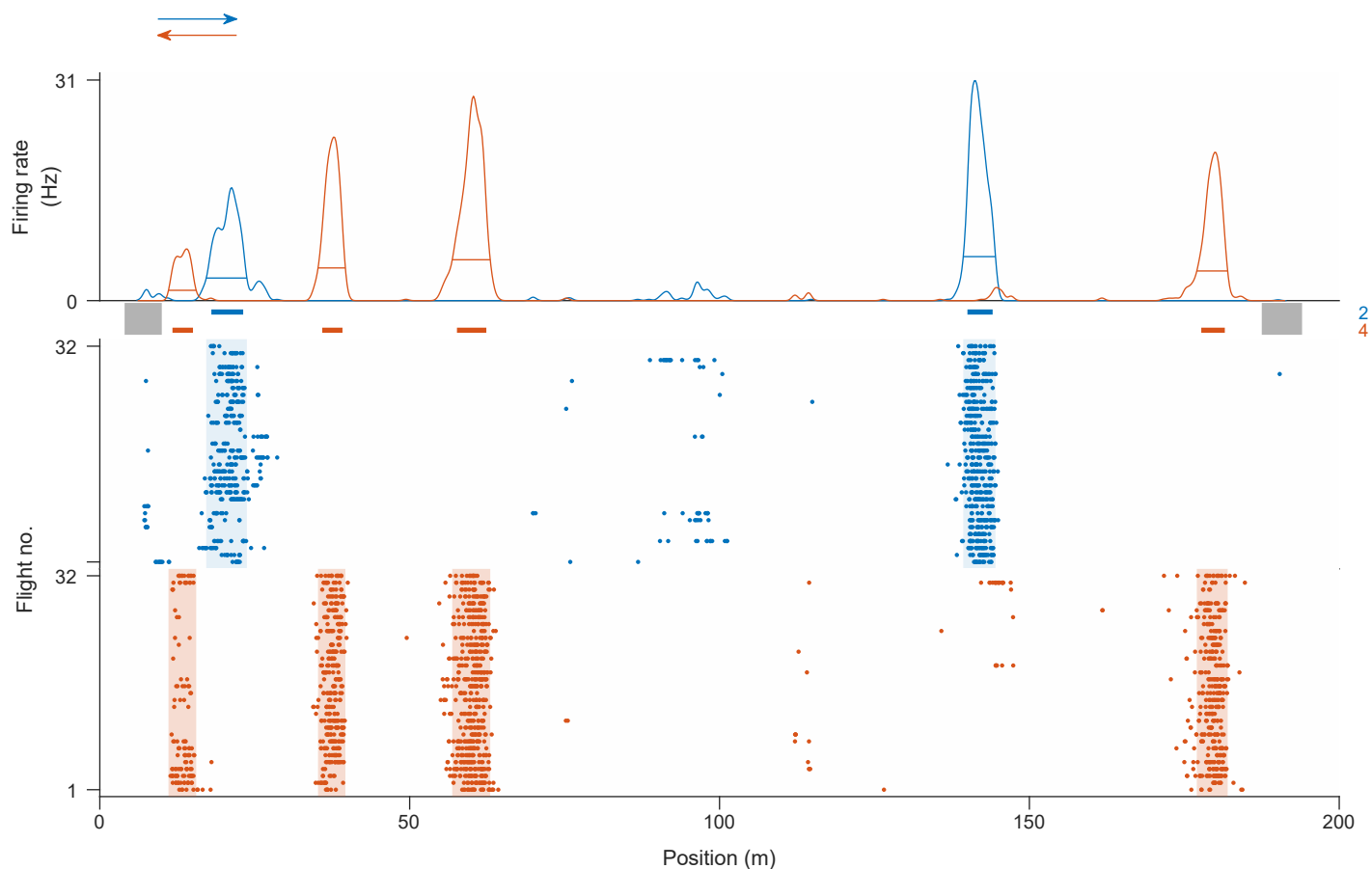


**fig. S4. Field detection and place field size.** Example cell showing the field detection process in detail. Top, firing-rate maps for both directions (blue and red lines; arrows indicate the flight direction). Bottom, raster plots of spike positions in each flight, presented separately for each flight direction (blue and red dots).

Place field size was defined as follows: For each field we computed its width at 20% of the field's peak firing-rate, which is plotted here as a horizontal thin line inside the firing-rate maps and as a shaded colored area in the rasters. We then defined the field edges by taking the 5–95% percentiles of spike locations included inside 20% of the field's peak, which is denoted here by the shaded area. Importantly, for defining the field size we used directly the spikes, and not the firing-rate map, in order to avoid smearing of small fields due to the Gaussian kernel smoothing that we used for the firing-rate maps ( $\sigma = 50$  cm; bin size 20 cm). We considered the field-size throughout the paper based on this latter definition of 5–95% percentiles of spike locations: these detected field-sizes are marked here by red- and blue-colored *thick* horizontal lines above the raster plots and below the firing-rate maps (same notation for field-size as in Fig. 2A, Fig. 4A, Fig. 5A, and Fig. 6B). Gray rectangles, low flight-speed zones. The numbers of fields in each direction are indicated by blue and red numbers on the right.

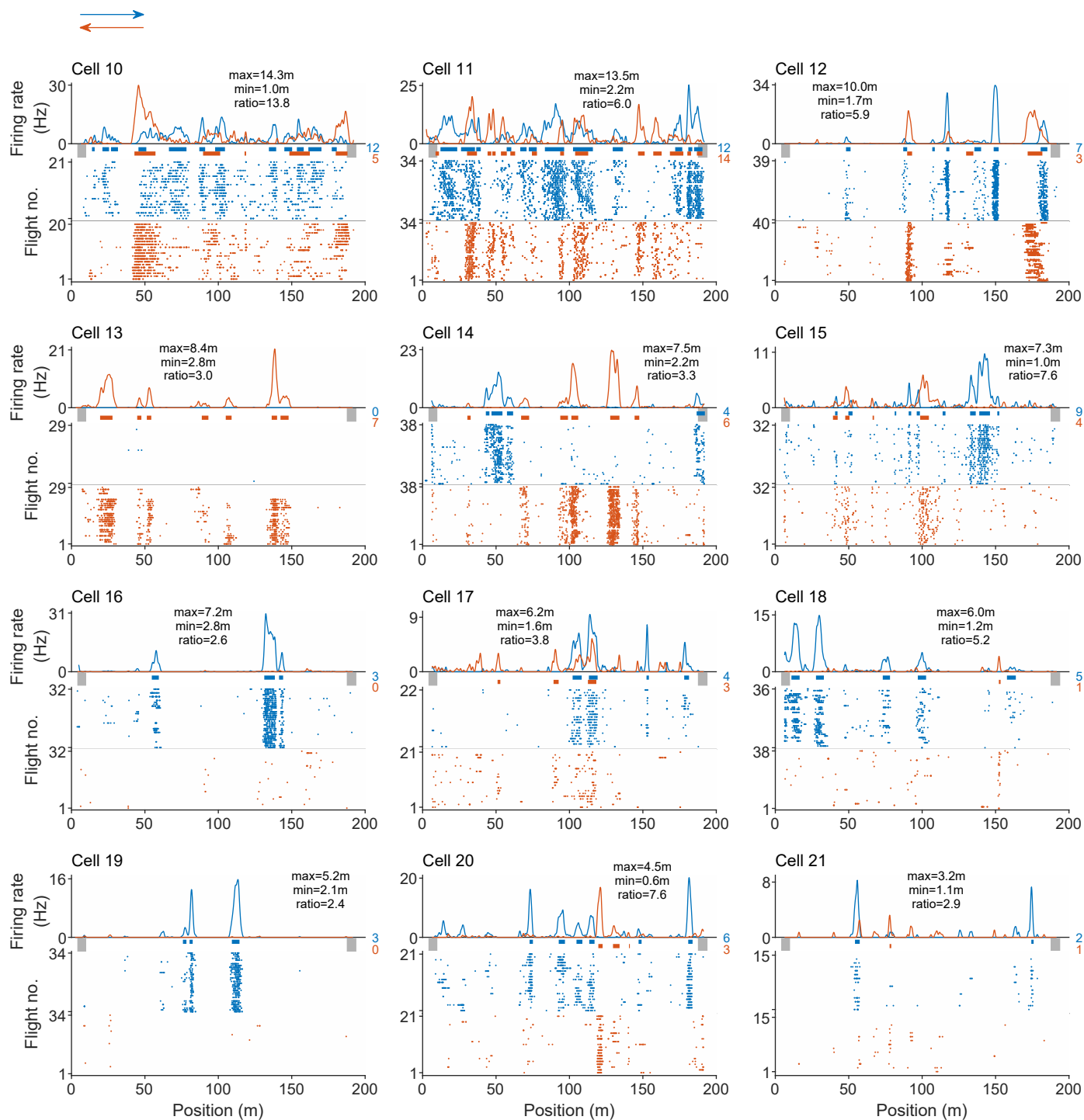


**fig. S5. Additional examples of firing-rate maps and raster plots for neurons recorded in the long 200 meter tunnel.** Examples of 12 significant place-cells, recorded from wild-born bats in the 200-meter long tunnel (dataset 1). Plotted as in main Fig. 2A. The examples were ordered here by the neuron's largest field size.

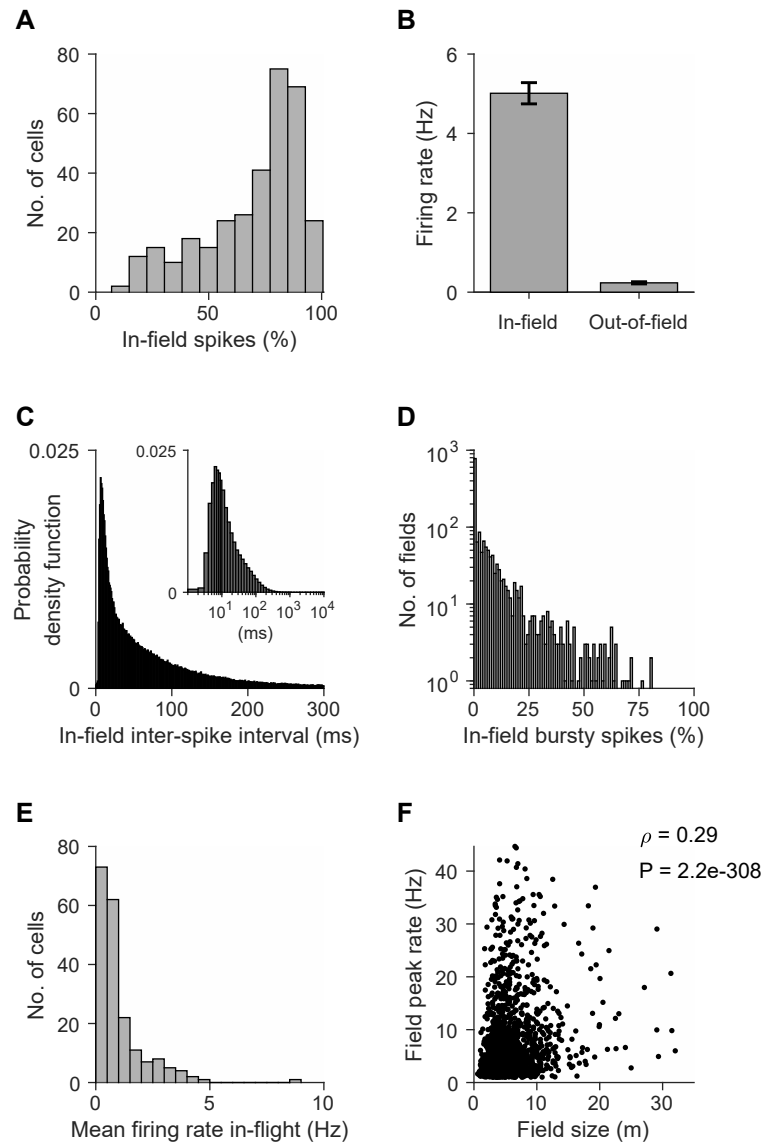


**fig. S6. Cells exhibited strong spatial tuning with high firing rates in-field and low firing rates out-of-field.**

(A) Distribution of the percentage of 'in-field spikes', i.e. spikes that occurred inside the place-fields of each cell; high percentage indicates low background firing ( $n = 331$  cells × directions; 5 bats). (B) Comparison of the firing rates in-field versus out-of-field: For each cell × direction we calculated the median firing rates within the fields ("in-field") and outside of fields ("out-of-field"). Error bars, mean  $\pm$  s.e.m – where the average was taken across those median values over the cells × directions (in-field firing rate:  $5.01 \pm 0.27$  Hz; out-of-field firing rate:  $0.24 \pm 0.03$  Hz;  $n = 331$  cells × directions). (C) Inter-spike-interval distribution, computed only for spikes that occurred inside fields (in-field spikes); pooled over all the in-field spikes from all the place cells ( $n = 196$  cells; 5 bats). Inset, x-axis in log-scale, showing a wider range of inter-spike intervals. (D) Distribution of the percentage of in-field bursty spikes, i.e. for each field we calculated the percentage of spikes that were part of a burst, where a burst was defined as spikes with inter-spike interval  $< 6$  ms (40). Pooled over all the fields from all the place cells ( $n = 1,629$  fields; 5 bats). (E) Distribution of mean firing rates during flight ( $n = 196$  place cells; the one neuron with in-flight firing-rate of  $> 5$  Hz was not classified as an interneuron, because the classification of putative interneurons versus pyramidal cells was based on mean firing-rate over the entire recording session, including the rest-epochs on the landing-balls and the sleep sessions, while here we plotted specifically the in-flight firing rate). (F) Scatter plot of the peak firing-rate of a field versus the field size, pooled over all the fields of all the place cells ( $n = 1,629$  fields; 5 bats [dataset 1]). The positive correlation (Spearman  $\rho = 0.29$ ,  $df = 1,627$ ,  $P = 2.2 \times 10^{-308}$ ) suggests that the firing rates go in the same direction as the field sizes – which may potentially further strengthen the decoding advantage of the multi-field multi-scale code that we discovered.

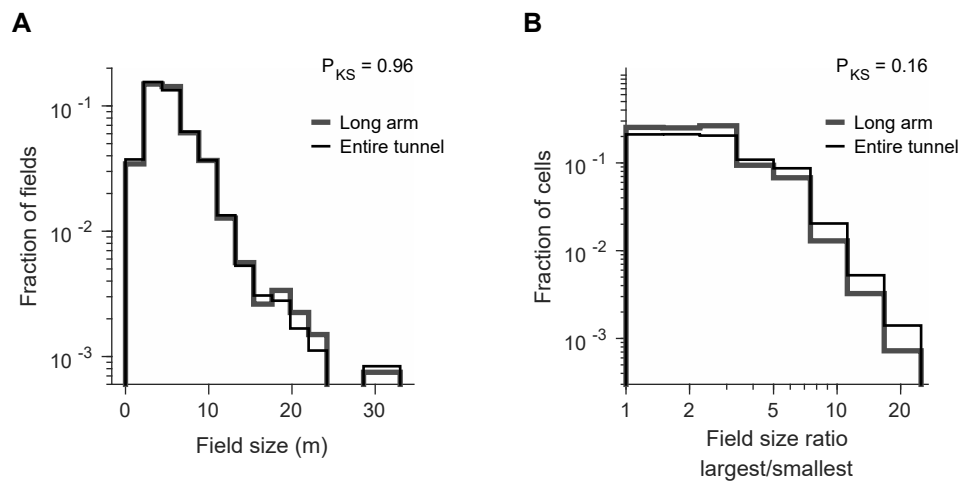


**fig. S7. Bat dorsal CA1 neurons exhibited multi-scale coding also when analyzing fields only in the long arm of the tunnel.** We compared here the distribution of field sizes and field size ratios between the data for the entire tunnel (for dataset 1), versus the same data but restricting the analysis only to fields in the long arm of the tunnel (see Fig. 1E-F). **(A)** Distributions of field sizes plotted separately for the long arm of the tunnel (thick gray line) and for the entire tunnel (thin black line). No significant difference was found between the two distributions (Kolmogorov-Smirnov test:  $P = 0.96$  [ $D_{KS\ 1214,1629} = 0.02$ ]). **(B)** Distribution of the ratio between largest and smallest field sizes for each neuron, using only the fields located in the long arm of the tunnel (thick gray line), or fields from the entire tunnel (thin black line) for comparison. The two distributions are very similar and did not differ significantly (Kolmogorov-Smirnov test:  $P = 0.16$  [ $D_{KS\ 167,172} = 0.12$ ]).

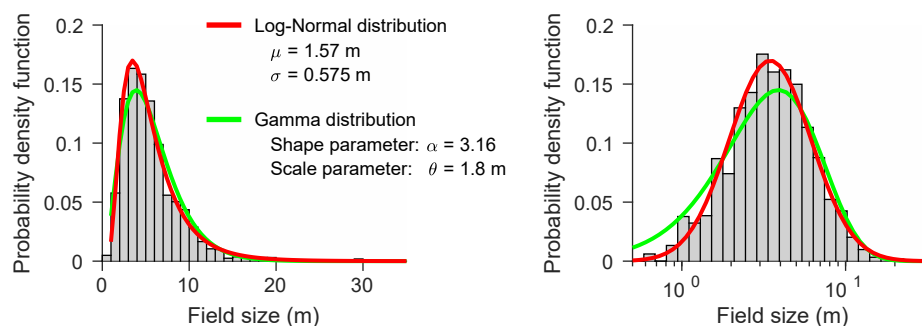


**fig. S8. Field-size distribution was skewed, and was well-fitted by a log-normal distribution, as well as by a gamma distribution.** Shown is the distribution of field-sizes found in our experiment, pooled over bats no. 1–5 (dataset 1) – all neurons, and both flight-directions (gray bars;  $n = 1,629$  fields) – together with fits of a log-normal distribution function (red) and gamma distribution function (green). The empirical distribution and the two fits were plotted here both using linear x-scale (left; bin size, 1 m) and using logarithmic x-scale (right). The empirical distribution was fitted well by both log-normal and gamma functions; the log-normal function (41), shown in red, provided a slightly better fit – as the log-normal fit was not significantly different from the data (Kolmogorov-Smirnov test:  $P = 0.74$  [ $D_{KS} = 0.017$ ]), while the gamma fit did differ significantly from the data (Kolmogorov-Smirnov test:  $P = 0.00036$  [ $D_{KS} = 0.051$ ]).



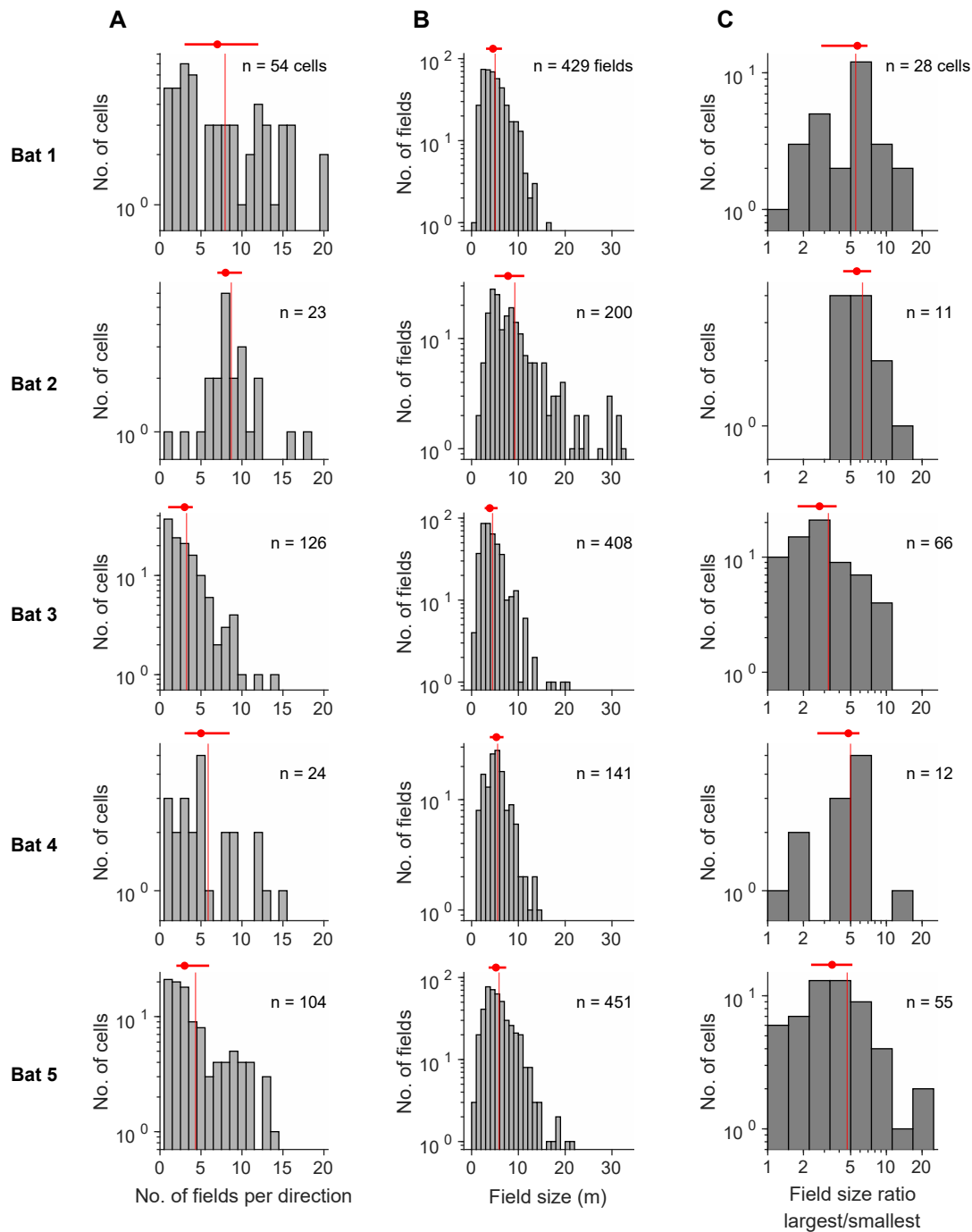


**fig. S9. Place-cells from all five bats exhibited a multi-field multi-scale code.** (A–C) Distributions of number of fields per direction (A), field sizes (B) and field size ratio (C), shown per animal – for all the 5 bats in dataset 1. Same graphical conventions as in main Fig. 2G,H,J. (A) Distribution of the number of place-fields per neuron per flight-direction ( $n$ , the number of cells  $\times$  directions, is indicated). Rightmost bar, cases with  $\geq 20$  fields per direction. (B) Distribution of place-field size ( $n$ , the number of fields, is indicated). Note that for *all* the individual bats, the field size ranged from sub-meter or meter level and up to at least 15 m size. (C) Distribution of the ratio between largest and smallest field sizes for each neuron ( $n$ , the number of cells with at least two fields, is indicated). Both axes here are in log-scale. Note that for *all* the individual bats, the field size ratio went up to at least a ratio of 10. For all the histograms in this figure: red vertical line indicates the distribution mean, red horizontal line and red dot indicate the interquartile range and the median.

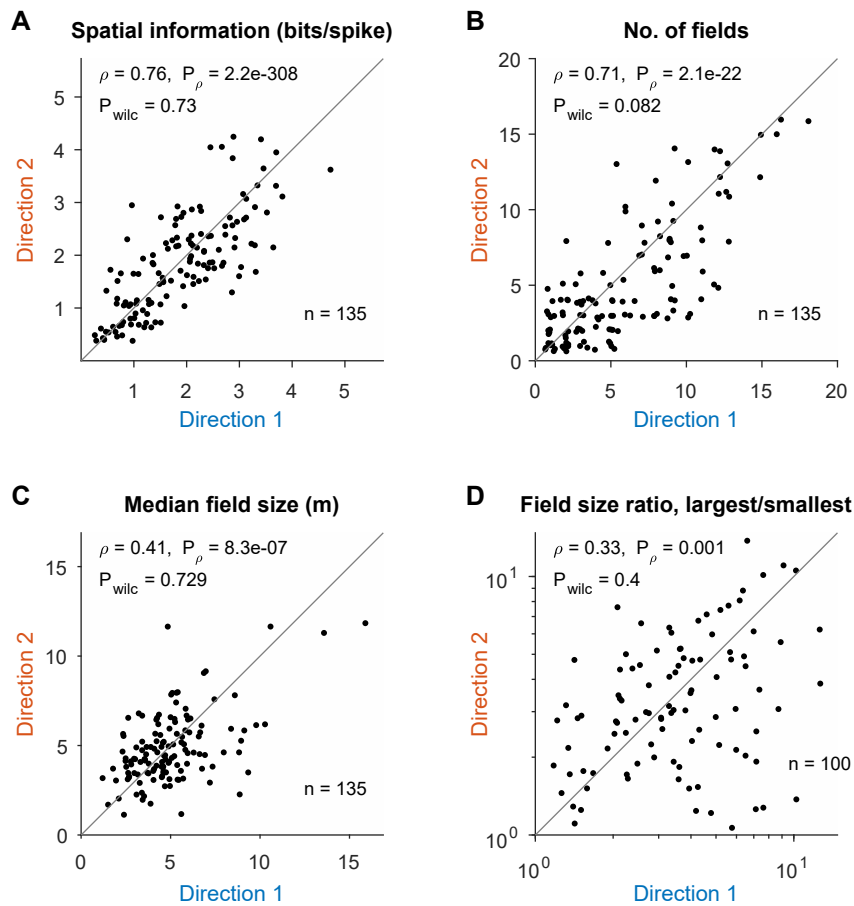


**fig. S10. Individual neurons exhibited similar multi-scale firing properties in both flight directions.**

(A–D) We compared four spatial firing properties between the two flight directions: spatial information (A), number of fields per direction (B), median field size (C), and field size ratio between the largest and the smallest fields per direction (D). Plotted are only neurons that were significant place-cells in both directions ( $n = 135$ ; in D we plotted only neurons with at least two fields in each direction [ $n = 100$ ]; the dots in B were slightly jittered, for display purposes only). Note the high correlations between the two directions, in all four panels (Spearman correlations  $\rho$ ; the  $P$ -values are indicated), as well as the lack of significant differences in paired comparisons between the two directions (Wilcoxon signed-rank test;  $P$ -values indicated) – together suggesting that individual place-cells have a characteristic firing-propensity per neuron, which is similar on average between the two directions.

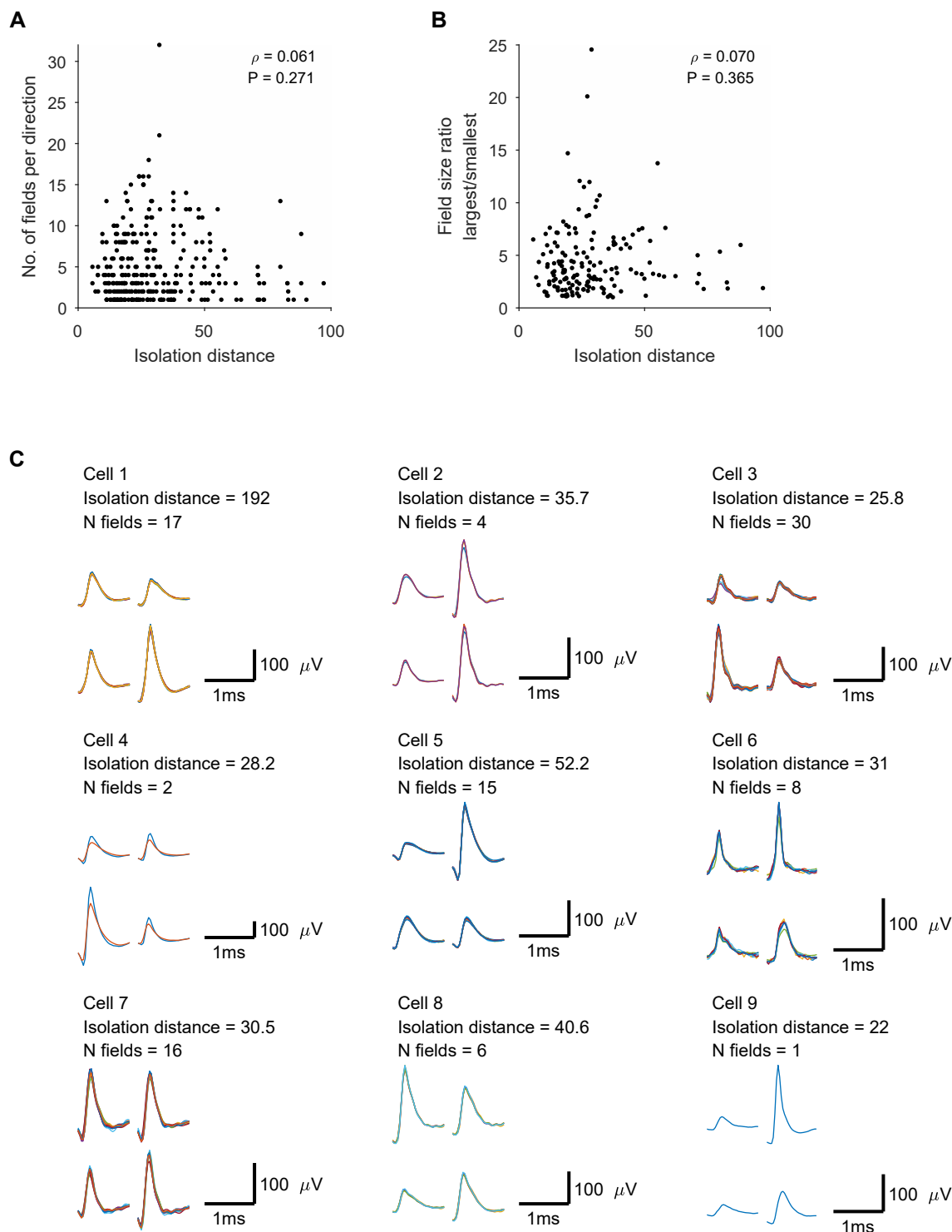


**fig. S11. Multi-scale coding cannot be explained by quality of single-unit spike sorting.** (A) Number of fields per direction plotted against the isolation-distance index (a standard metric for spike-sorting quality (42); a larger number means a better-isolated cluster; the isolation-distance was averaged over 10 min windows). There was no significant correlation between the spike-sorting quality and the number of fields per direction (Spearman  $\rho = 0.061$ ,  $df = 329$ ,  $P = 0.271$ ;  $n = 331$  cells  $\times$  directions; included were only cells  $\times$  directions that were significantly place-tuned) – suggesting that the multiple-fields cannot be explained by poor spike sorting. (B) Field size ratio between the largest and smallest field for each neuron, plotted against the isolation-distance index (42). There was no significant correlation between the spike-sorting quality and the multi-scale property (Spearman  $\rho = 0.070$ ,  $df = 170$ ,  $P = 0.365$ ;  $n = 172$  cells; included were only place-cells with  $\geq 2$  fields overall) – suggesting that the multi-scale property cannot be explained by poor spike sorting. In panels A and B, we showed data only up to isolation-distance = 100, for visualization purposes only (*all* data points, including with isolation-distance  $> 100$ , were used in the computation of the correlations).

(C) Mean spike waveforms for each place-field, for the 9 cells shown in Fig. 2A (same numbering as in Fig. 2A). Spike waveforms from different fields were averaged and overlaid on top of each other with different colors (the 4 spike panels for each neuron correspond to the 4 channels of the tetrode). The isolation-distance and number-of-fields for each neuron are indicated. Note that the spike waveforms were very similar for spikes from different fields: For example, in cell 1, the average spikes of 17 fields are plotted on top of each other and are totally overlapping – arguing that all these 17 fields came from the same neuron. Scale bars: 1 ms, 100  $\mu$ V.

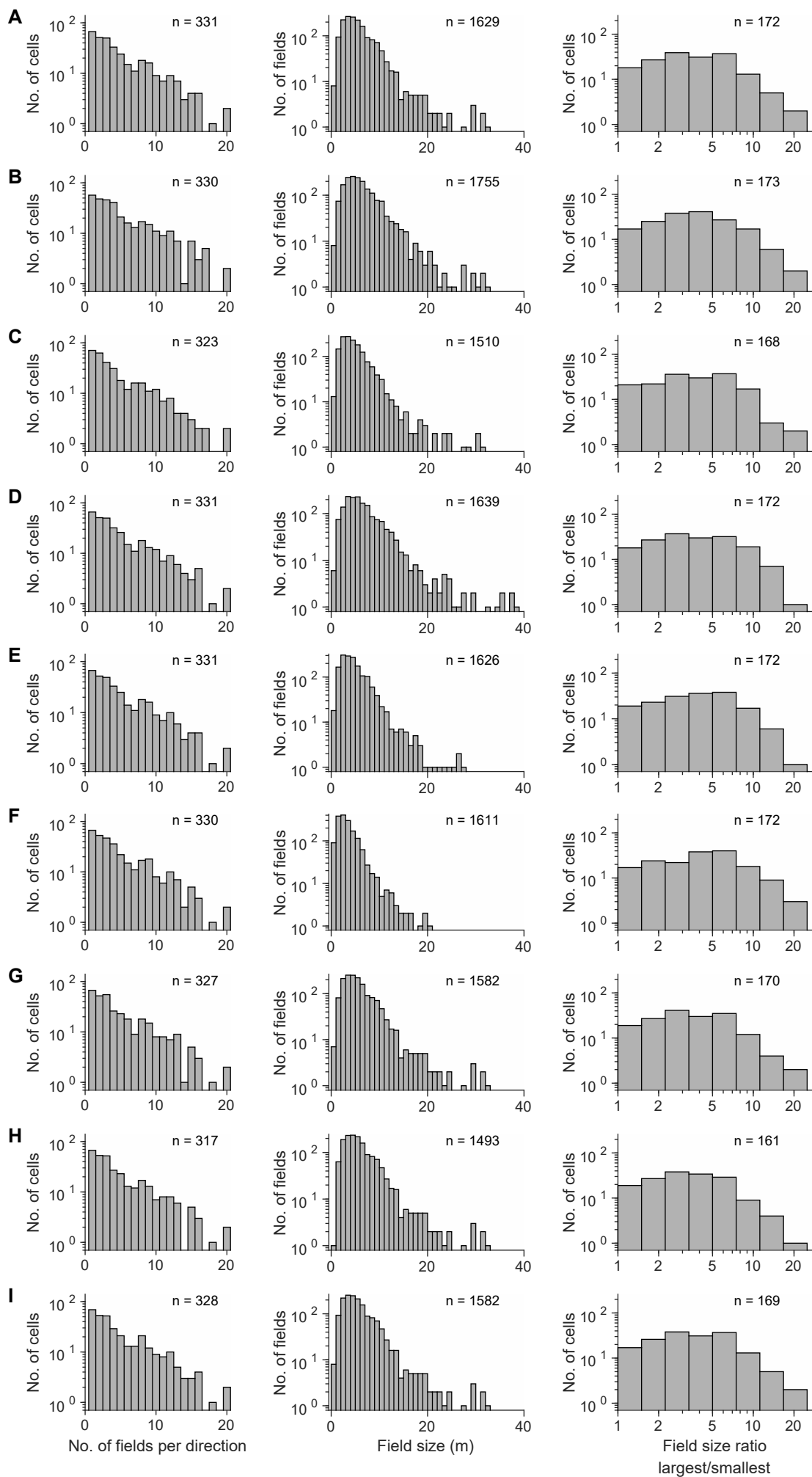


**fig. S12. The multi-field and multi-scale results were robust to the criteria of field-detection.**

To ensure the multi-scale results are robust to the detailed criteria of field-detection, we repeated all analyses with several different sets of parameters for field-detection (listed below). For each set of parameters (rows), we plotted the following three distributions (columns): (i) number of fields per direction (left column); (ii) field size (middle column); and (iii) field size ratio of largest field / smallest field (right column). Same binning was used here as in Fig. 2G, H, J. The number of cells or fields that passed the criteria is indicated on each panel.

(A) The original set of parameters used for all the analyses in the paper (identical to main Fig. 2G, H, J: see details in Materials and Methods). (B–I) Variations on place-field detection criteria. (B) Boundaries of the field were computed based on 10% of the peak firing rate of the place-field (instead of the standard 20%). (C) Boundaries of the field were computed based on 30% of the peak firing rate of the place-field (instead of the standard 20%).

(D) Field size was defined as the 0–100% percentile of the spike positions – i.e. we used all spikes (instead of the standard 5–95%). (E) Field size was defined as the 10–90% percentile of the spike positions (instead of the standard 5–95%). (F) Field size was defined as the 20–80% percentile of the spike positions (instead of the standard 5–95%). (G) We required at least 25% laps with spikes inside the place-field (instead of the standard 20%).

(H) We required at least 30% laps with spikes inside the place-field (instead of the standard 20%).

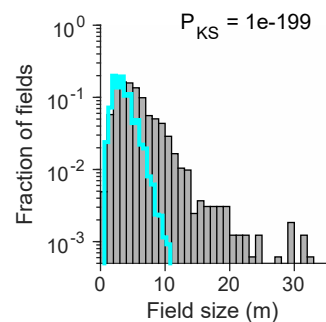
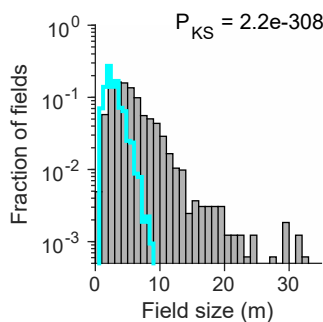
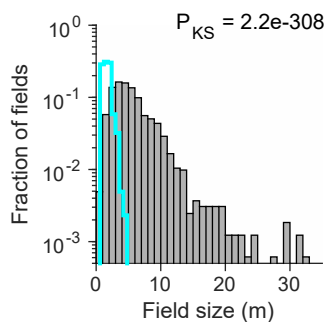
(I) We required at least 5 laps (or 20% of the laps – whichever is larger) with  $\geq k$  spikes inside the place-field, where  $k$  is the expected number of spikes – i.e. the total number of spikes inside the field divided by the total number of laps through the field.

## Gamma distribution fitted to:

Field sizes in 6m tunnel  
scaled to median  
inter-landmark interval

Smallest field per neuron  
in 200m tunnel

Matched  
coverage



■ Data  
— Small-scale  
compartments model

Matched  
no. of fields

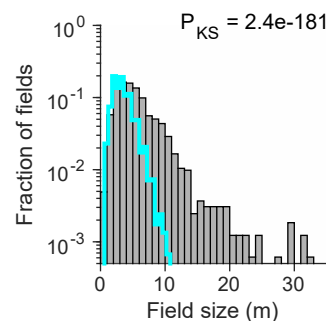
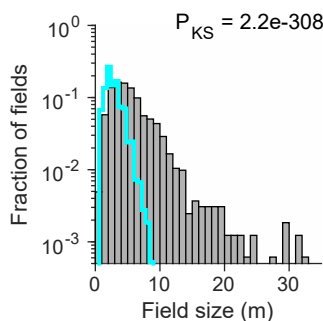
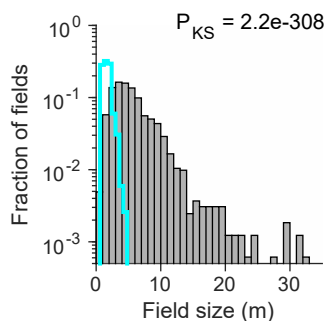


**fig. S13. A small-scale compartmentalization model could not explain the wide distribution of field sizes.** We considered here an alternative hypothesis in which the landmarks divided the large environment into multiple compartments. We generated new fields in each compartment with locations drawn from a Poisson distribution and size drawn from a gamma distribution with parameters fitted to the data (see details in Materials and Methods, and below). Importantly, overlapping fields were allowed to merge at the edges of the compartments (i.e. at the landmarks) – yielding enlarged fields. We considered 6 different models. Top row, models matched to the average coverage in the 200 m tunnel; Bottom row, models matched to the average number of fields in the 200-m tunnel. Columns, fitting a gamma distribution to the field-sizes in the 6 m tunnel (left), or to the field-sizes in the 6 m tunnel scaled up to the median of the inter-landmark interval (middle), or to the field-sizes based on the smallest field per neuron in the 200 m tunnel (right). Gray bars, distribution of field sizes from the experimental data in the 200 m tunnel (dataset 1; 5 bats); Cyan line, field sizes of the null distributions that were computed based on the small-scale compartmentalization model. Note that all the null distributions based on the compartmentalization model (cyan) did *not* capture the experimental data (gray), but rather had a narrow field size distribution – with much smaller fields than observed in the data. Further, we note that because this compartmentalization model yields enlarged fields near landmarks, this should create a clustering of large fields near landmarks – which we did *not* observe in the data (Fig. 3).

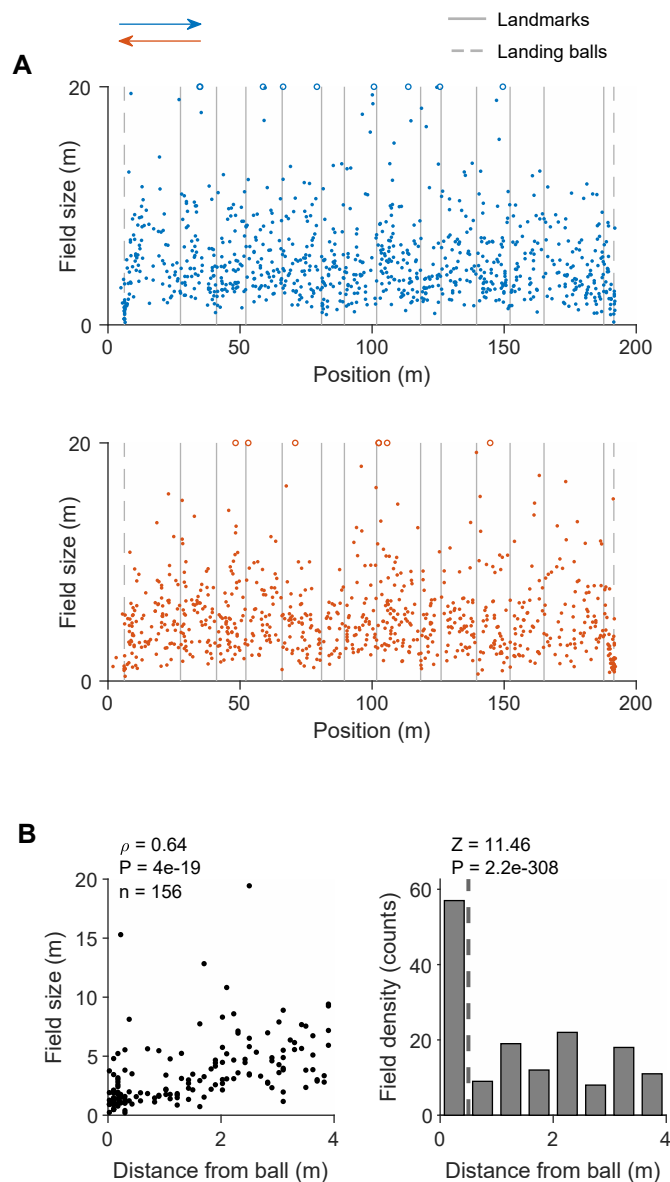


**fig. S14. Over-representation near the landing balls (reward locations).** (A) Shown are field size versus field location (defined as the location of the field's peak firing-rate). Open circles, fields larger than 20 meters. This plot is identical to main Fig. 3D, except that here we included also the fields near the landing-balls with the food (vertical dashed lines), where the flight speed was lower (i.e. the fields in the gray zones in Fig. 1I – which were *not* included in the main analyses in the paper). Note the over-representation of fields near these two reward areas, manifested as higher density of fields and smaller field-sizes (see concentration of dots near the vertical dashed lines). (B) Focus on the vicinity of the landing-balls (4 meters from the balls); as in A, we included here also fields that were excluded in the main analyses because they were very close to the landing-balls. Left: In the vicinity of the landing-balls the place-fields tended to be smaller, indicated by a significant positive correlation between field-size and distance-to-ball (Spearman  $\rho = 0.64$ ,  $P = 4 \times 10^{-19}$ ; correlations computed over the 4 meters nearest to the balls, pooling the 2 balls and 2 directions together). Note, however, that despite this strong correlation, there were nevertheless also a few very large place-fields adjoining the landing-balls (note the four fields [four uppermost dots] with size of  $>10$  meters, whose peaks occurred within the first 4 meters of the tunnel). The decrease in field-size near landing-balls could be due to the importance (saliency) of this reward location, or due to the low velocity during landing/takeoff, or it could reflect predictions from the boundary vector-cell model (26, 28). Right: field density was much higher adjacent to the landing-balls (field density was binned here using 0.5-meter bins, and then the value in the first bin was z-scored with respect to the values in all the other bins; z-score [ $z = 11.46$ ] was computed compared to the 50 meters nearest to the balls, pooling the 2 balls and 2 directions together).



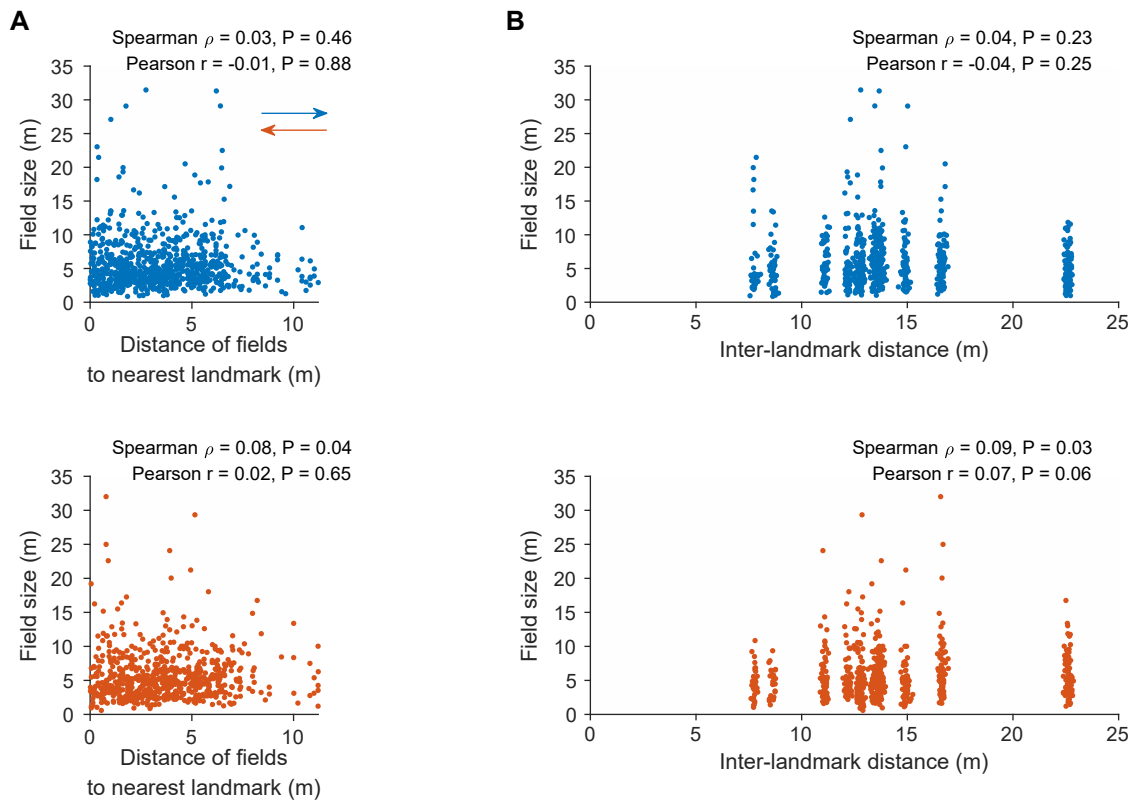


**fig. S15. Field sizes did not correlate strongly with the distance to the nearest landmark, or with the local inter-landmark distance.** (A) Scatter plots of the field-size versus the distance of the field's peak to its nearest landmark – plotted separately for the two directions (top and bottom). No strong correlation was found (Top scatter: Spearman  $\rho = 0.03$ ,  $P = 0.46$  and Pearson  $r = -0.01$ ,  $P = 0.88$ ;  $df = 780$ ; Bottom scatter: Spearman  $\rho = 0.08$ ,  $P = 0.04$  and Pearson  $r = 0.02$ ,  $P = 0.65$ ;  $df = 659$ ). (B) Scatter plots of field-size versus the local inter-landmark distance (the distance between the two landmarks that surround the location of that field – i.e. the landmarks before and after the location of the peak of that particular field). Top, Eastward flight direction; Bottom, Westward flight direction. No strong correlation was found between field size and the distance between its surrounding landmarks (Top scatter: Spearman  $\rho = 0.04$ ,  $P = 0.23$  and Pearson  $r = -0.04$ ,  $P = 0.25$ ;  $df = 780$ ; Bottom scatter: Spearman  $\rho = 0.09$ ,  $P = 0.03$  and Pearson  $r = 0.07$ ,  $P = 0.06$ ;  $df = 659$ ). The distance between adjacent landmarks is strongly discretized (see discretization of data along the x-axis in B), hence we slightly jittered the dots in the x-axis for display purposes only (the correlations were computed without the jitter).

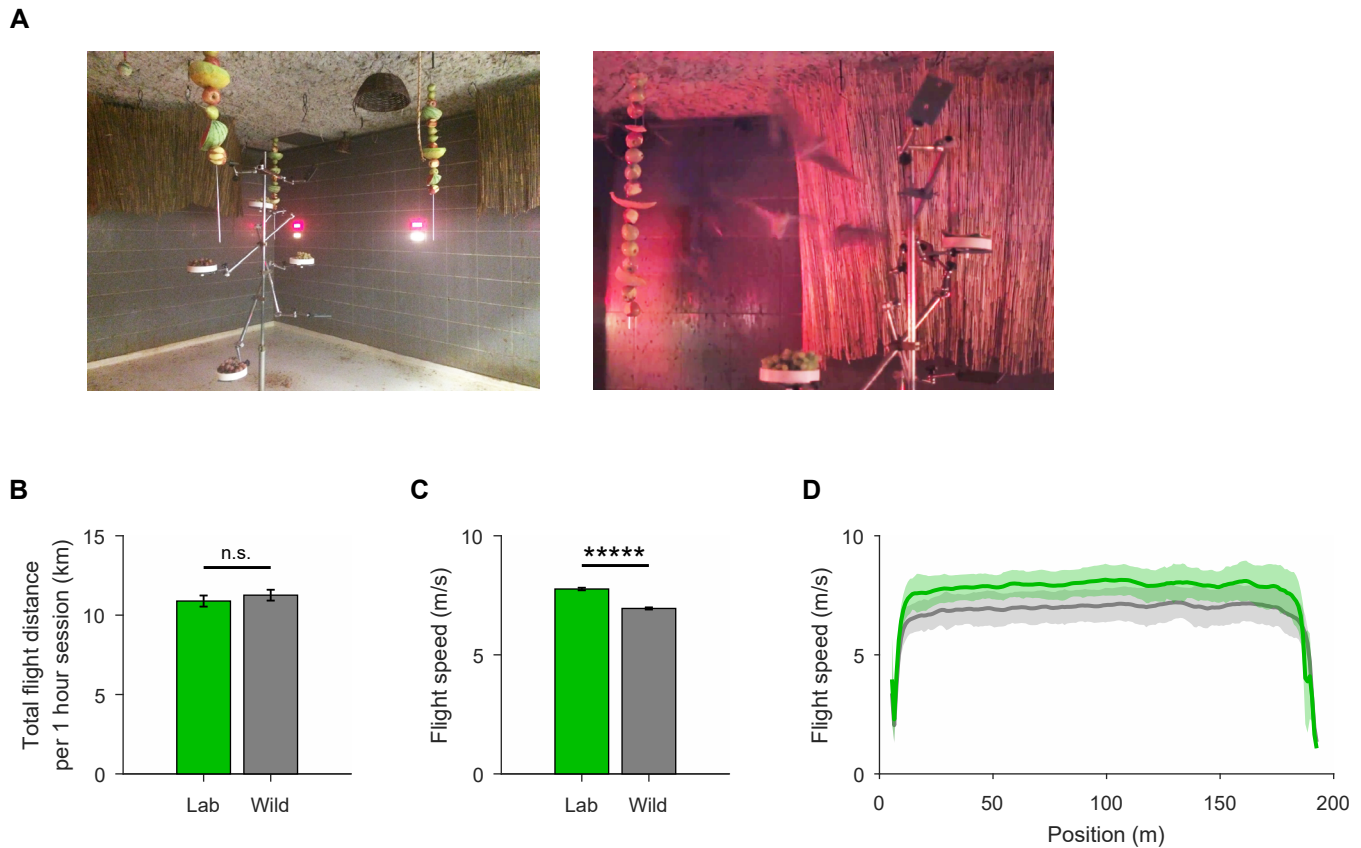


**fig. S16. Lab-born bats were housed in an enriched environment and did not undergo strong sensory or motor deprivation, and performed many continuous fast flights in the tunnel, similarly to the wild-born bats.**

(A) Photographs of the bat colony room (5.3 × 5.0 × 2.9 meters), where the lab-born bats (dataset 4: see Table S1) were born and developed until adulthood. Left, zoom-out view of the room; Right, zoom-in showing several bats flying (photographs taken on different days). All the other bats, which were wild-caught as adults [datasets 1,2,3] resided in the same colony room for several months prior to the start of pre-training. The lab-born bats were never exposed to larger rooms than this colony room during their development. The room was large enough for the bats to fly freely, and it was enriched with many items on which the bats could land – such as nets, ropes, baskets, curtains, skewers with fruit, and tree-like structure (only some of these items are visible on these photographs). The colony included several dozens of bats at any given moment, with rich social interactions between them, and thus the bats were not socially deprived. (B) Total flight distance per hour for recording sessions in the 200 m tunnel, for the lab-born bats (green,  $n = 37$  sessions, 3 bats) and for the wild-born bats (gray,  $n = 60$  sessions, 5 bats); these are all the sessions in which place-cells were recorded. No significant difference was found between the datasets ( $t$ -test:  $t = -0.72$ ,  $df = 95$ ,  $P = 0.47$ ) – suggesting that the lab-born bats were in good flight shape, as good as the wild-born bats. They maintained good flight shape by flying extensively in the large colony room shown in A. Error bars, mean ± s.e.m. (C) Flight speeds of the lab-born bats in the tunnel were rather high – even slightly higher than for the wild-born bats ( $t$ -test:  $t = 13.04$ ,  $df = 95$ ,  $P = 6.9 \times 10^{-23}$ ) – indicating again that the lab-born bats were not motor-deprived. Error bars, mean ± s.e.m. (lab:  $n = 37$ , wild:  $n = 60$  sessions); the averaged flight speed per session was computed over the entire session, pooled over all locations (excluding the ‘gray zones’ near the landing-balls, shown in Fig. 1I). (D) Flight speeds of the lab-born bats (green: dataset 4), plotted as a function of position, showing that the flight speed was rather constant along the tunnel – as was the case for the wild-born bats (gray: dataset 1). Error bars, mean ± s.d., computed in 1-meter bins, pooled across all bats and flights in each dataset.

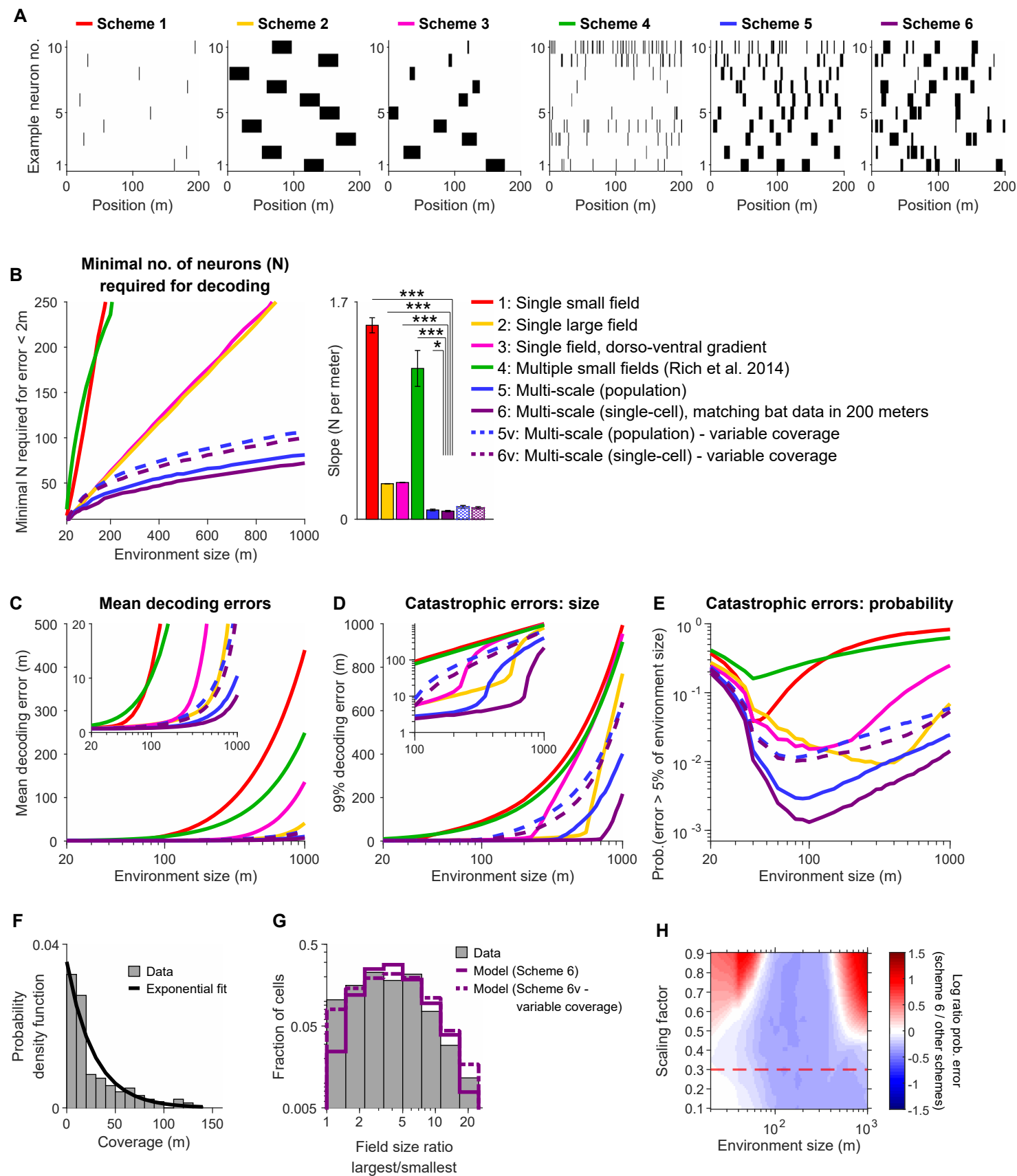


**fig. S17. Robustness of the theoretical decoding results to variations in field coverage and in the scaling factor  $\delta$ .** (A–E) Same as Fig. 7A-E, but here we added two new variants of schemes 5 and 6 – denoted as schemes 5v and 6v (dashed lines) – which had variable coverage across neurons, matching the coverage distribution of the data (see panel F; the coverage of a neuron denotes the overall fraction of the environment covered by the neuron's place-fields). (F) Distribution of the coverage for the experimental data (gray bars), together with the fitted exponential distribution (black line). This exponential distribution was used to generate the fields in schemes 5v and 6v (see Materials and Methods). (G) Distributions of the field size ratio (ratio of largest to smallest field sizes per neuron) for the experimental data (gray bars) and for model schemes 6 and 6v (purple solid line and purple dashed line, respectively). (H) Robustness of model results to variations in the scaling factor  $\delta$  (which determines how the average field size and total coverage scale with the environment size; see Materials and Methods). Shown in color is the log of the ratio between the probability for large error (larger than 5% of the environment) in scheme 6 versus the best (lowest) probability in all the five other schemes: blue color, scheme 6 outperforms all others; white, no difference; red, one of the other schemes outperforms scheme 6. This plot shows that scheme 6 has outperformed all the other schemes over a wide range of scaling factors  $\delta$  (y-axis) and environment sizes (x-axis): note the large region of blue color (scheme 6 outperforms all the other schemes). Red dashed line, scaling factor  $\delta = 0.3$ , which is the scaling factor that was fitted to the bat data and which was used in all the main decoding analyses.

## Population Vector decoder instead of Maximum Likelihood decoder

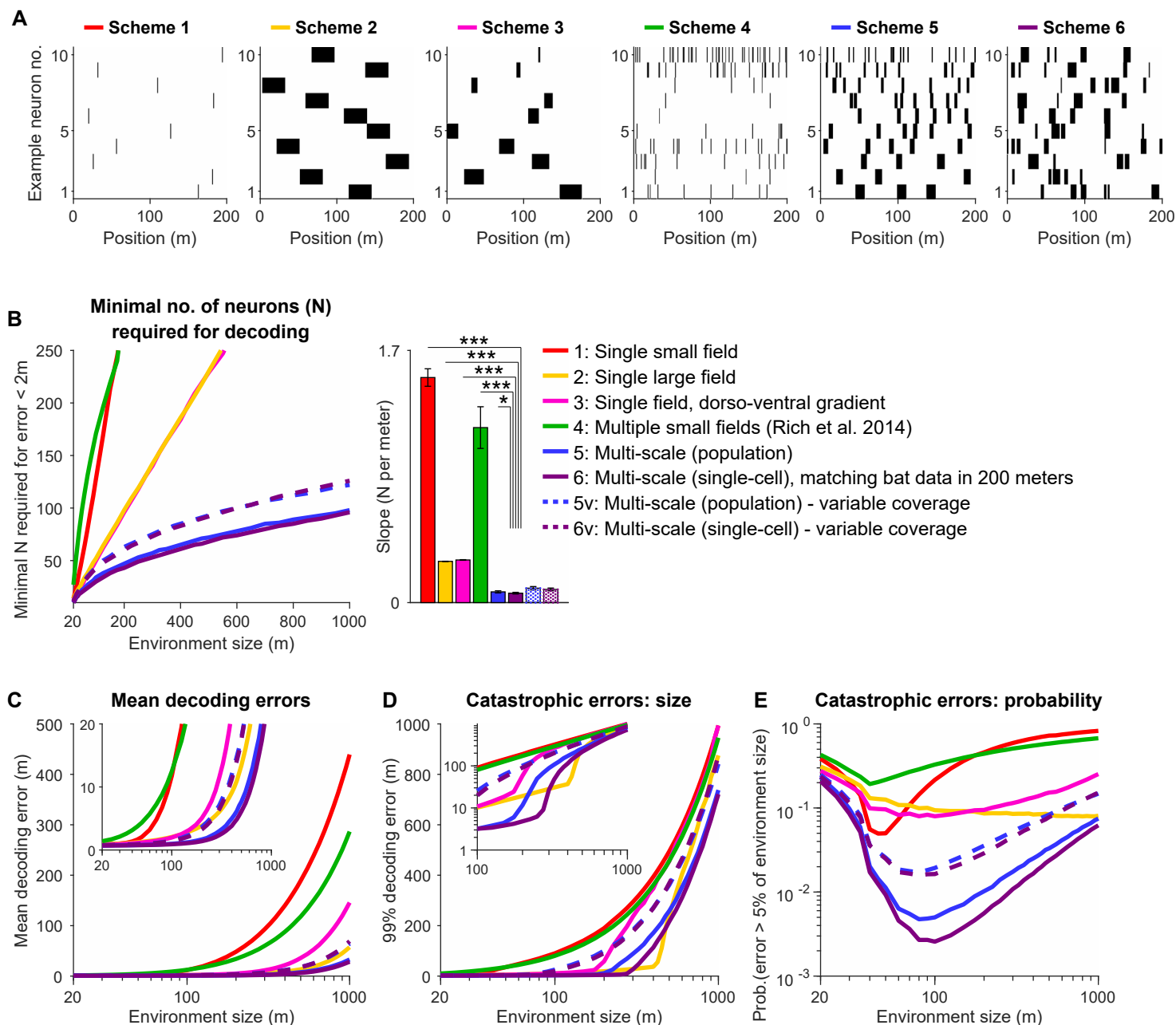
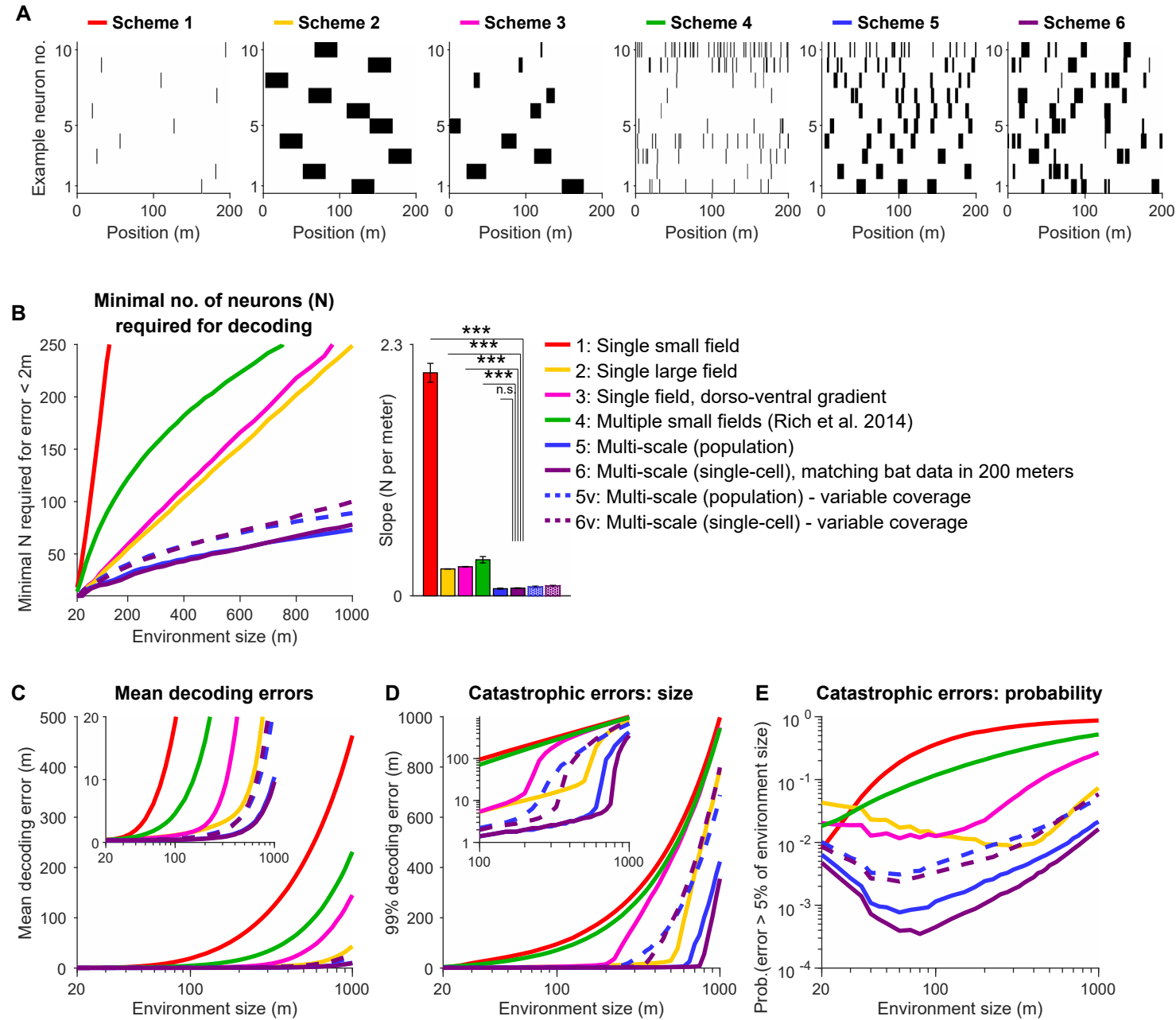


**fig. S18. Decoding accuracy of model simulations using a Population Vector (PV) decoder was qualitatively similar to Maximum Likelihood (ML) decoder.** (A–E) Same as Fig. 7A–E, but based on PV decoder instead of the Bayesian ML decoder used in Fig. 7. The within-neuron multi-scale representation (scheme 6) outperformed other encoding schemes in terms of the minimum number of neurons required to maintain a small decoding error of 2-m (B); and in terms of the size (D) and probability (E) of catastrophic errors. We note that the absolute error using a PV decoder (this figure) is generally larger than using the ML decoder (Fig. 7) – but the overall pattern of results is similar between the two decoders.

Integration time window of  $\Delta t = 200$  ms instead of 500 ms



Varying the integration time window  $\Delta t$

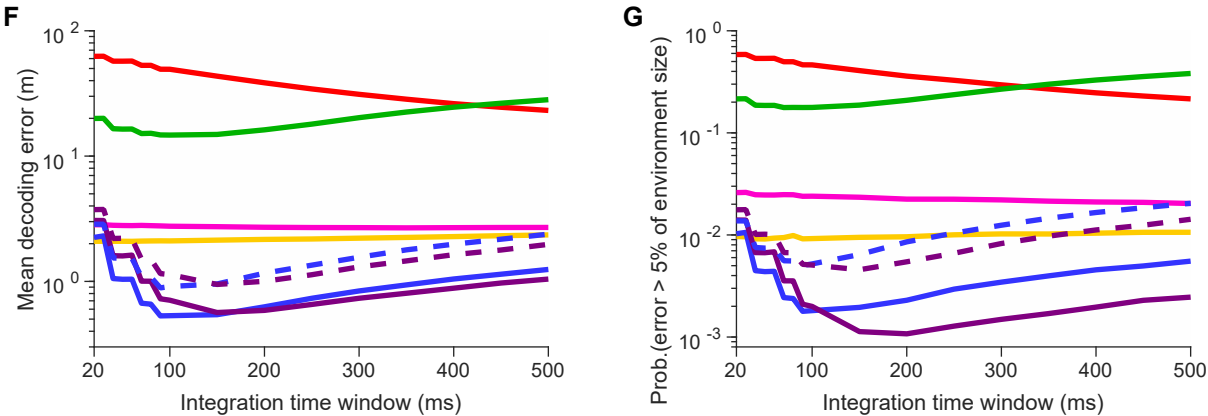
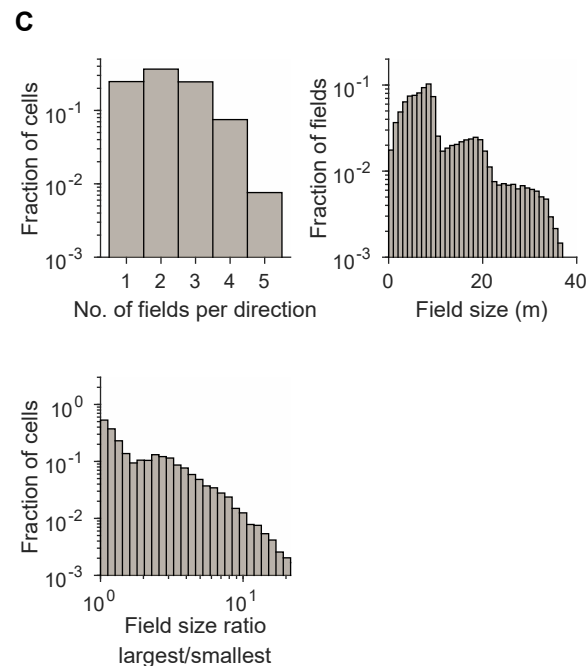
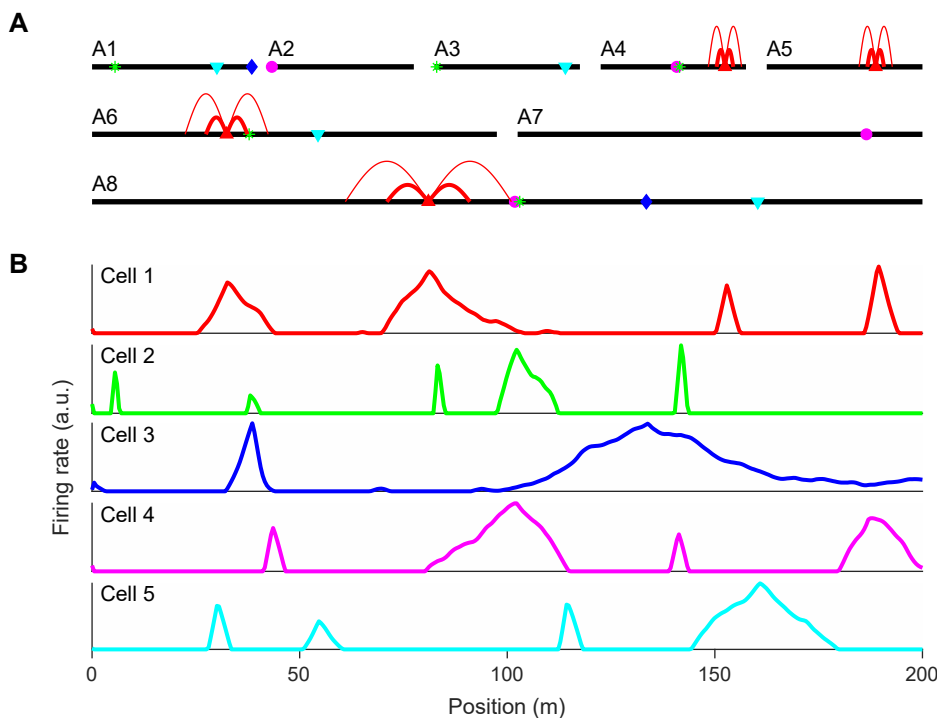


**fig. S19. Relative decoding accuracy of different encoding schemes did not depend strongly on the length of the integration time-window  $\Delta t$ .** (A–E) Same as Fig. 7A–E, but using integration time-window of  $\Delta t = 200$  ms, instead of the time-window of  $\Delta t = 500$  ms used in Fig. 7. (F and G) Mean decoding error (F) and probability for catastrophic errors (G) for all the schemes, at an environment-size of 200 m, plotted as function of the integration time-window  $\Delta t$  (for  $\Delta t$  between 20 ms and 500 ms). Encoding schemes with one or a few fields (schemes 1–4) showed little dependence on the integration time-window. Encoding schemes with a broad distribution of field-sizes (schemes 5, 6) showed stronger dependence on the integration time-window: encoding improved when the average field-size approximately matched the distance that the animal travels during the integration time-window  $\Delta t$ .

## Overall summary of neural network modeling

## Attractor network model



## Feedforward model

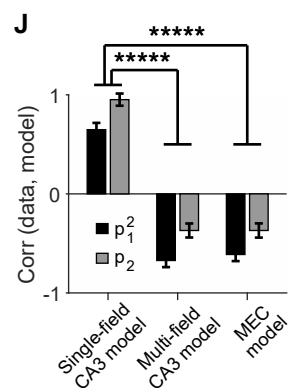
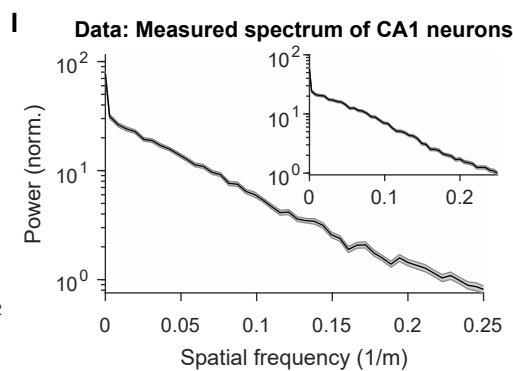
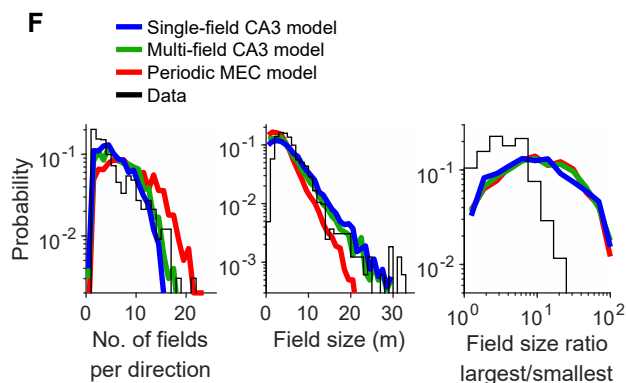
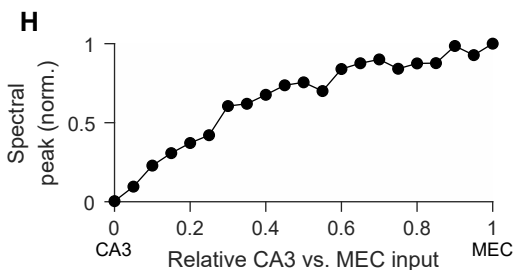
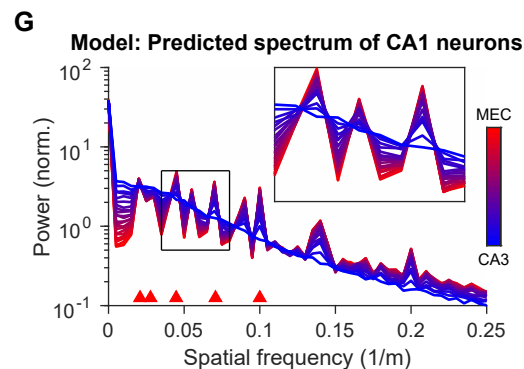
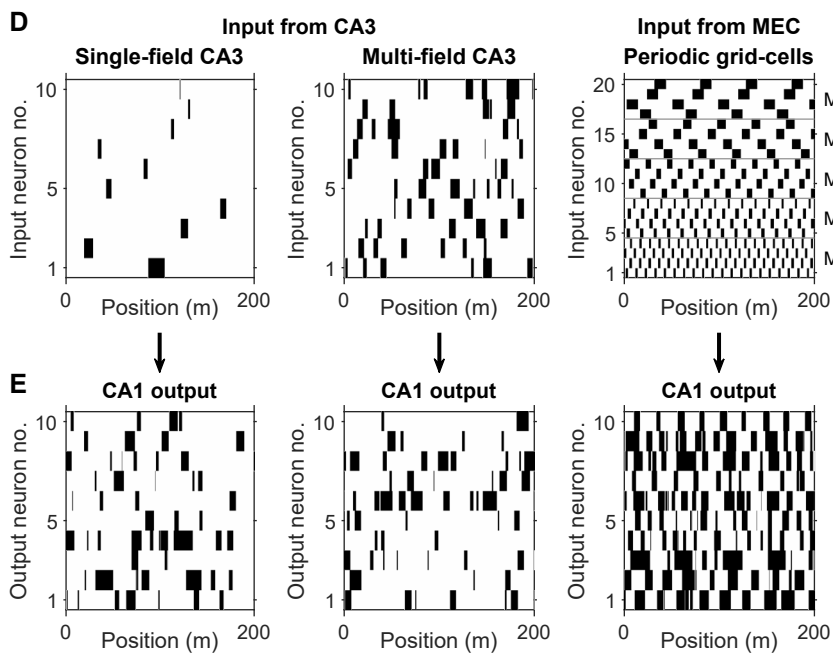




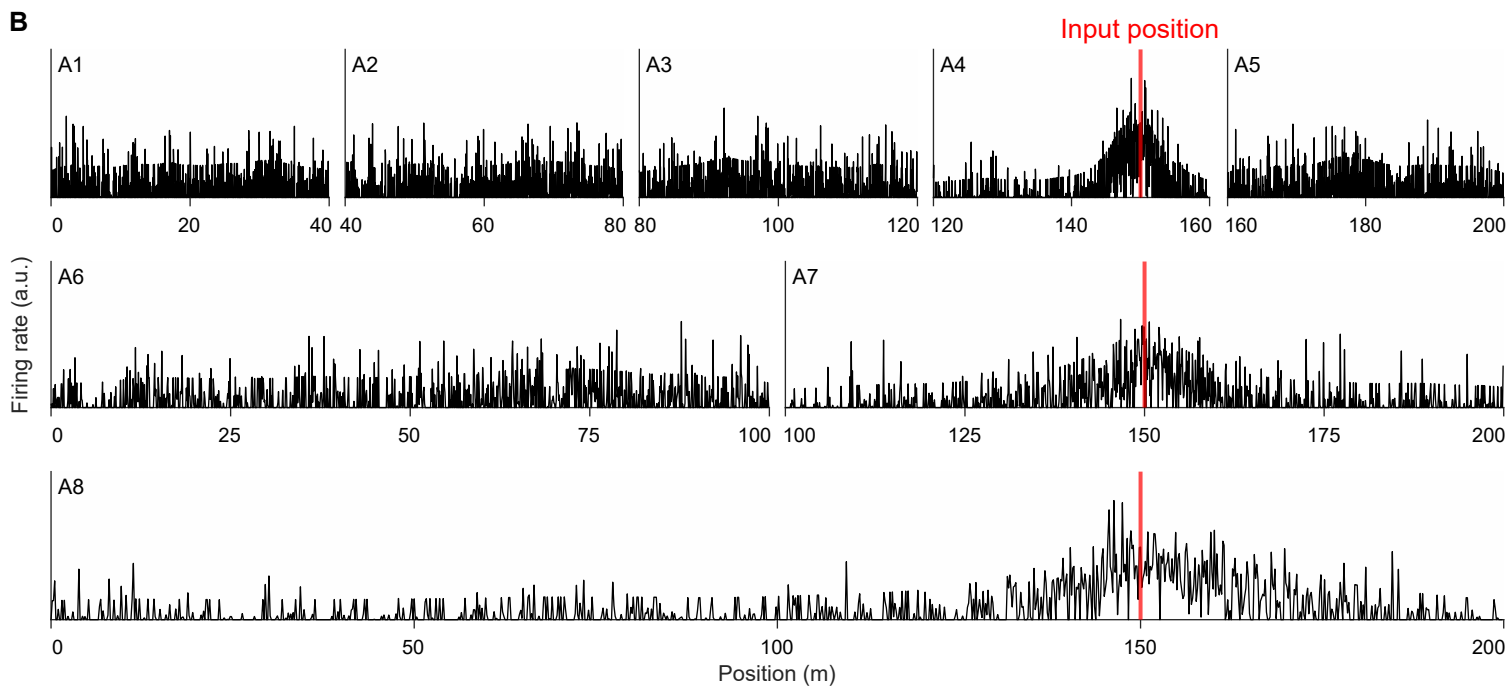
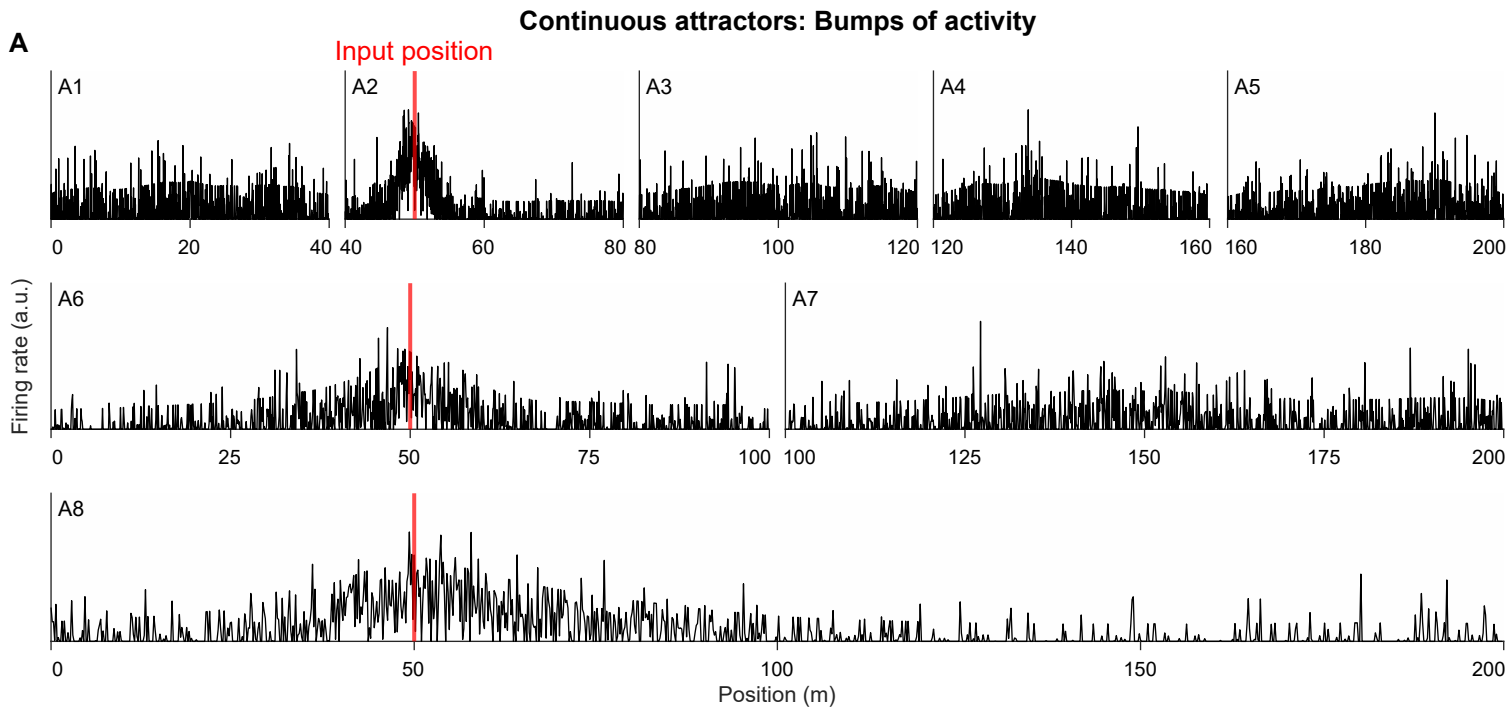
**fig. 20. Two families of neural network models for multi-scale coding: continuous attractor model with multiple attractors, and feedforward models with inputs from CA3 and MEC.**

For a detailed description of the models, see Supplementary Text.

**(A–C)** A model of multiple continuous attractor networks. **(A)** Schematic of the model: we simulated 8 attractors with different scales (black lines), in which we allowed neurons to randomly participate in several attractors (see Materials and Methods). Positions of five example neurons are denoted by colored symbols. The excitatory connectivity radius of each neuron is small for attractors A1–A5, medium for attractors A6–A7, and large for attractor network A8. For simplicity we only show the connectivity for the red neuron: see red arcs.

**(B)** Simulations of the model: examples. Plotted are the firing-rate maps of the five neurons from A, showing multiple fields and multi-scale coding for each neuron. Note that a neuron from the same attractor can have fields with very different sizes: For example, cell 3 (dark blue) and cell 2 (green) have their largest fields assigned to the same attractor (A8), but these fields exhibited very different sizes. **(C)** Distribution of multi-scale field properties of the attractor-model neurons. Top-left, number of fields per direction; right, field sizes; bottom, field size ratio. We simulated here only one flight direction, for which results are shown. Note the continuum of field sizes (top-right panel; achieved through the sharing of neurons across attractors), and the multi-scale coding at the level of single neurons (large values of field size ratio: bottom panel).

**(D–J)** Feedforward model with synaptic inputs from CA3 or MEC into CA1. **(D)** Three models of inputs from CA3 or MEC into CA1: Left, cells in CA3 have single fields with gradually increasing field sizes across the population (mimicking a dorso-ventral gradient); Middle, each cell in CA3 has multi-field multi-scale coding; Right, periodic 1D grid-cell inputs from 5 different grid-modules. **(E)** Examples of output neurons in CA1 for each scheme in D: these output neurons were generated by summing the inputs from 100 input-neurons with randomized synaptic weights, and then setting a threshold such that the total coverage matched the experimental data. **(F)** Distribution of multi-field multi-scale properties of CA1 output neurons (Blue, single-field CA3 model; Green, multi-field multi-scale CA3 model; Red, periodic MEC model; Black, experimental data). Note that all three models captured quite well the experimental results for the distributions of number of fields and field sizes, while the field size ratios were over-estimated by all 3 models. **(G–H)** A hybrid model, which weighs inputs from CA3 and MEC, exhibited clear spectral peaks (distinct spatial frequencies) in CA1 output cells. **(G)** Mean spatial spectrum of CA1 output neurons. Blue, only inputs from CA3: in this case CA1 shows a flat power spectrum. Increasing the relative contribution of MEC inputs (towards red color) changes the spectrum to have distinct spectral peaks, with spatial frequencies corresponding to the spacings of the input grid modules (red arrowheads at the bottom). Inset, zoom-in around the spectral peaks (black rectangle). **(H)** Quantification of the spectral peaks in CA1 as we gradually changed the inputs from pure CA3 inputs through CA3/MEC mixture to pure MEC inputs. **(I)** Testing the model in G–H against the data. Shown is the spatial spectrum of the firing-rate maps of the experimental data; mean  $\pm$  s.e.m across all recorded CA1 place-cells ( $n = 331$  cells  $\times$  directions). Note the lack of any distinct spectral peaks, indicating a lack of periodic inputs from MEC. Inset, the spatial spectrum for the binarized maps (in which bins inside the place-fields were set to 1, and bins outside of place-fields were set to 0); no spectral peaks are observed here as well. See also fig. S22H for similar plots for individual bats. **(J)** Correlation between the experimental data and the 3 feedforward models, comparing probabilities for field appearance/disappearance in the data (fig. S23A) and field appearance/disappearance under synaptic-perturbations in the model (see Materials and Methods). Here we computed the Spearman correlation between the probability profiles for data versus model of observing changes in a single place-field ( $p_1^2$ ) and concurrent changes in two place-fields ( $p_2$ ); see fig. S23B–C for the probability profiles, and for further details. Note the correlation between data and model was highest for the single-field CA3 model, suggesting that this model best describes the dynamics of field appearance/disappearance in the data. Error bars, mean  $\pm$  s.d. (estimated by randomly drawing 10,000 profiles from the data in fig. S23C according to their distribution, and computing their Spearman correlations with the profile of the model in fig. S23B); \*\*\*\*\*,  $P < 10^{-5}$  (z-test).



**C Control model: Independent attractors**

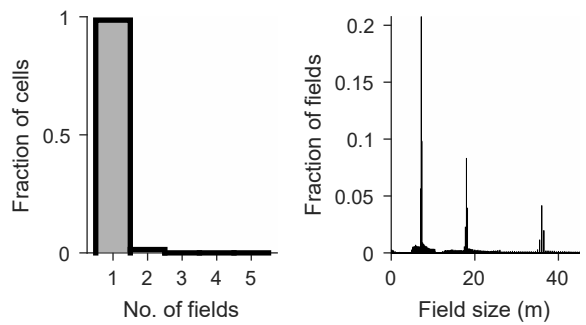


**fig. S21. Consistent bumps of activity across multiple interacting attractors with randomly-shared neurons; and analysis of independent attractors.**

For a detailed description of the continuous attractor model, see Supplementary Text, and Materials and Methods. (A and B) Network activity snapshots of the 8 attractors for the model shown in fig. S20A-C, when the bat was at positions 50 m (A) and 150 m (B) (marked by the vertical red lines denoted “Input position”). Note the clear bumps of activity at the input position, seen in all the relevant attractors concurrently. Note also that because in this model a single neuron can participate in multiple attractors, this creates what seems to be ‘noise’ in the activity profile. (C) Distributions of place-field properties for the control model of independent attractors: this model was identical to the main model, except that here each neuron participated only in one single attractor, with no sharing of neurons between attractors. Left, number of fields; Right, Fields sizes. Note that in this control model, each neuron exhibited a single place-field with a highly-discretized distribution of field sizes across the population (with three different scales corresponding to the 3 scales of the attractors) – as expected from classical studies of continuous attractor network models of place cells, but very different from the model of interacting attractors shown in fig. S20 (see distributions in fig. S20C).

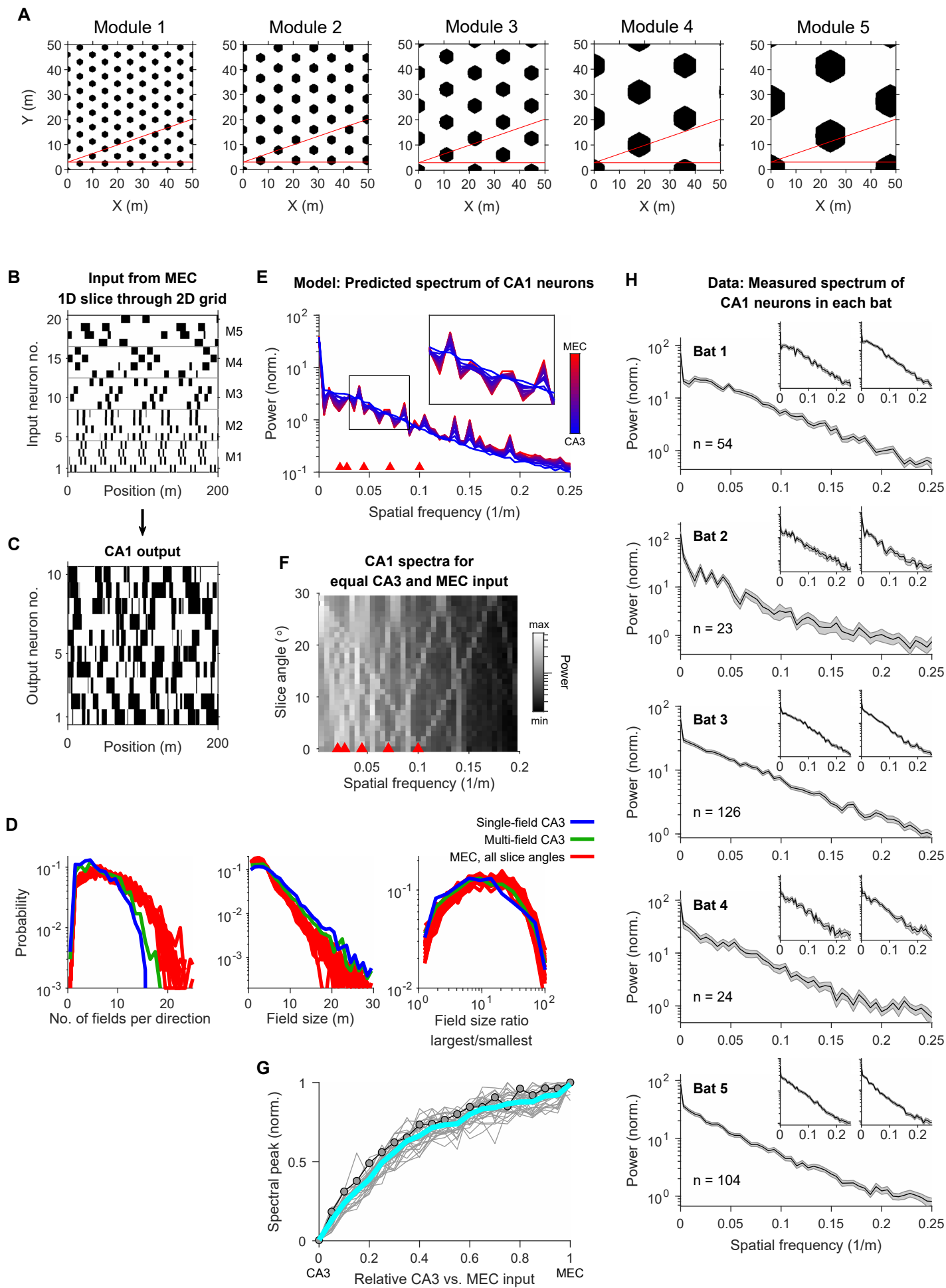


**fig. S22. Feedforward model with MEC inputs that are based on 1D slices through a 2D grid.**

For a detailed description of the feedforward models, see Supplementary Text.

We based here the MEC input on a published model of 1D slices through 2D grids (23). This model (Model 4 among the feedforward models discussed in the Supplementary Text and in the Materials and Methods) yields similar results to the model based on perfectly-periodic 1D MEC neurons (Model 3) that is shown in fig. S20. **(A)** Five example model 2D grid cells from grid modules with increasing scale. Red lines, two examples of 1D slices through the 2D grid. The horizontal line represents a perfect 1D periodic grid and was used in the main analysis (fig. S20D, right – Model 3). The other line was rotated by 19° and is one of 30 rotated lines that we considered in this analysis (Model 4; angles 0°–29° span the entire range of unique slicing angles through a hexagonal lattice). We used the slice at angle 19° shown here also for panels B,C,E,G. **(B)** Examples of input cells into CA1: MEC input model consisted here of 1D slices at 19° through a perfect hexagonal 2D grid (as shown in A); four example neurons are shown from each module. **(C)** Example neurons of output cells in CA1 generated from the input model MEC neurons in B. **(D)** Multi-scale field properties of CA1 output cells for the different input models (Blue, single-field CA3 model; Green, Multi-field CA3 model; Red lines, different angles of 1D slices through 2D grid [all 30 angles are shown]). Note that all models were qualitatively similar; in particular, different 1D slices through a 2D grid exhibited very similar results. **(E–G)** A hybrid model, which weighs inputs from CA3 and MEC, is exhibiting different magnitudes of spectral peaks in CA1 output cells – depending on the CA3/MEC mixture at the input. **(E)** Mean spatial spectrum of the firing-rate maps of CA1 output neurons (slice angle: 19°). Blue, only inputs from CA3 – showing a power spectrum with no distinct spectral peaks; when the relative contribution of MEC inputs is increased (towards red color), the CA1 spectra are changing and exhibit spectral peaks; the spatial frequencies of the peaks were different from those expected from 1 / spacing of the input grid modules (red arrowheads at the bottom), because the cutting-angle of the slice leads to different frequencies. Inset, zoom-in around the spectral peaks (rectangle). **(F)** A model that equally weights CA3 and MEC inputs shows clear spectral peaks in the CA1 output neurons, for all slice angles. Each row is the average spatial spectrum at a particular 1D-slice angle (averaged over many phases [shifts] of the 1D slice). Note that the expected frequencies are changing with the slice angle – but for all slice angles the model yields clear spectral peaks in CA1. **(G)** Quantification of the gradual change in the spectral peak size in CA1 model neurons when the input is changing from only CA3 inputs to only MEC inputs. Gray lines, different 1D-slice angles (all 30 angles are shown); Black circles, 1D-slice at angle 19° (same simulations as in panel E); Cyan line, average over all the 1D-slice angles. Note that clear spectral peaks occur even if the MEC input is as small as 10% or 20% of the total input into CA1 (high spectral peaks are seen even at  $x$ -axis = 0.1 or 0.2). **(H)** Spatial spectrum of the experimental firing-rate maps from the 200 m tunnel, shown separately for each individual bat; plotted are mean  $\pm$  s.e.m. over the spectra of all the place cells  $\times$  directions in each bat (the numbers of place cells  $\times$  directions are indicated). We plotted the spatial spectrum for each bat separately, in order to accommodate the possibility that each bat may represent the environment with slightly different spacings (which would yield different spectral peaks per animal), or with 1D-slices at different angles (which would also result in different spectral peaks: see panel F). Left insets, the spatial spectrum calculated for the binarized maps, where we set to 1 and 0 the bins inside and outside of the experimentally-measured fields, respectively – akin to our binarized model. Right insets, the spatial spectrum calculated for the long arm of the tunnel only. Note that the spatial spectrum of bat CA1 place-cells recorded in the 200 m tunnel does *not* show any prominent spectral peaks, in any of the bats, and in any of the variations (main plot + 2 insets) – indicating a lack of periodic contribution from MEC. This implies that either the MEC inputs provide little drive to CA1 neurons as compared to the CA3 inputs; or alternatively, this implies that MEC neurons do *not* exhibit periodic structure in 1D in very large environments, and also the firing of MEC neurons *cannot* be explained as a 1D slice through a 2D grid in very large environments. Testing this latter prediction calls for performing MEC recordings in the large-scale tunnel.

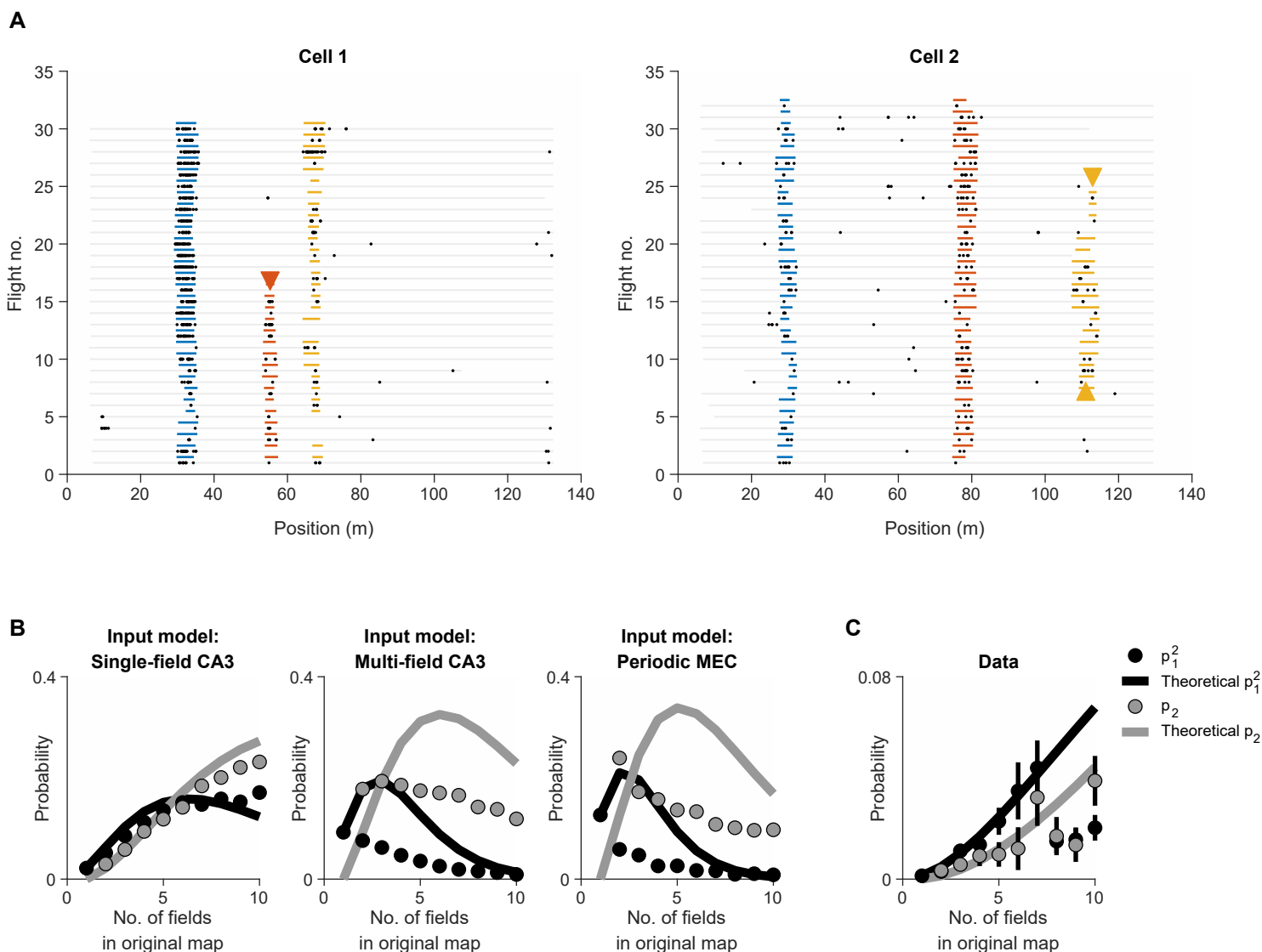


**fig. S23. Detection of within-day dynamics, and the consistency of this dynamics with the feedforward single-field model of CA3.** For a detailed description of the feedforward models, see Supplementary Text, and Materials and Methods. **(A)** Examples of the detection of within-day place-field dynamics in two recorded CA1 cells (dataset 3). Shown are the position of the bat on different flights (gray horizontal lines) overlaid with spike rasters (black dots) and with field detections (colored lines; plotted with a vertical offset of 0.5 flights for display purposes). Fields were detected using a moving window of 5 flights; arrowheads denote appearance and disappearance of fields (as determined by the algorithm described in the Materials and Methods). Note the disappearance of the middle field in cell 1 while the other fields were stable; and likewise the appearance and disappearance of the rightmost field in cell 2 while the other fields were stable. **(B)** Modeling the changes in output maps in CA1, based on our set of feedforward models (fig. S20D-J), after applying concurrent synaptic perturbations in a small portion (4%) of the input synapses to CA1. Dots, probability of a change in a single field ( $p_1$ , black) or in two fields simultaneously ( $p_2$ , gray), plotted as a function of the number of fields in the original map – shown for the different feedforward models. Lines, the theoretical probability of  $p_1$  (black) and  $p_2$  (gray) [we plotted here the square of  $p_1$  ( $p_1^2$ ) for display purposes – because for a small number of fields,  $p_1^2 \approx p_2$  in the independent binomial case]. These theoretical probabilities were derived from the probability of a single-field change ( $p_1$ ) within one field in the original map (leftmost black point); this theoretical probability is based on an assumption of independence between fields and thus uses the binomial distribution. Note that the probabilities for changes in one field ( $p_1$ ) or in two fields ( $p_2$ ) are *increasing* with the number of fields for the ‘single-field CA3’ model (left panel, black and gray dots), while they are *decreasing* for models with multiple fields (middle and right panels, black and gray dots). Note also that the theoretical lines, which were computed based on an independence assumption (binomial distribution: computed based on  $p_1$  only), are capturing well the probabilities of the simulated model only for the ‘single-field CA3’ model (left) but not for the models with multiple fields (middle and right panels).

(C) Probability of field changes in the experimental data from dataset 3 (Table S1; measured as shown in panel A). Plotted using the same notations as in panel B. Error bars, mean  $\pm$  standard error of the proportion. Rightmost data-points represent maps with 10 or more fields pooled together. Note that the theoretical predicted line (based on the independence assumption) is capturing the data quite well. Importantly, note that the probability for a single-field change ( $p_1^2$ ) and for two-fields change ( $p_2$ ) are increasing with the number of fields in the map (see black and gray dots) – which is most similar to the trend of the black and gray dots in the ‘single-field CA3’ model (panel B, left); the correlations between the dots in the data (panel C) versus the models (panel B) are shown in fig. S20J.

**Table S1. Experimental datasets**

Experimental dataset	Figures where these data are plotted	Bat no.	Bat ID	Wild / Lab born bat	Arena size	No. of training sessions*	No. of recording sessions with: CA1 cells / Behaviorally-Active cells / Place cells	No. of cells: CA1 putative pyramidal cells <sup>†</sup> / Behaviorally-Active cells <sup>‡</sup> / Place cells
<b>1) Wild-born bats, large-scale</b>	Fig. 1-6 fig. S1 fig. S3-S17 fig. S20F,I fig. S22H	1	0034	Wild	200 m	10	7/7/7	31/31/30
		2	0079	Wild	200 m	10**	17/17/10	25/25/12
		3	0148	Wild	200 m	12**	28/28/25	97/97/79
		4	2289	Wild	200 m	15	3/3/3	15/15/14
		5	9861	Wild	200 m	11	17/17/15	67/67/61
		<b>Total</b>					<b>72/72/60</b>	<b>235/235/196</b>
<b>2) Wild-born bats, small-scale</b>	Fig. 4 Fig. 5	6	2382	Wild	6 m	>20***	5/5/4	28/13/11
		7	2311	Wild	6 m	>20***	3/2/2	15/10/7
		8	2329	Wild	6 m	>20***	5/5/4	24/13/12
		<b>Total</b>					<b>13/12/10</b>	<b>67/36/30</b>
<b>3) Wild-born bats, large-scale, recordings from day 1</b>	Fig. 5 fig. S20J fig. S23	6	2382	Wild	130 m	0	31/30/29	173/115/104
		7	2311	Wild	130 m	0	12/11/11	36/26/21
		<b>Total</b>					<b>43/41/40</b>	<b>209/141/125</b>
<b>4) Lab-born bats, large-scale</b>	Fig. 6 fig. S16	9	9845	Lab	200 m	47	17/13/10	20/15/11
		10	0102	Lab	200 m	17	8/8/8	15/15/15
		11	0194	Lab	200 m	20	19/19/19	78/70/69
		<b>Total</b>					<b>44/40/37</b>	<b>113/100/95</b>

\* Number of training sessions or recording sessions in the tunnel before the first place-cell was recorded.

\*\* For bats no. 2 and 3 there may have been a few additional training sessions that were not documented.

\*\*\* There was no systematic documentation for the training sessions in the 6 m arena.

† CA1 putative pyramidal cells listed here were all the pyramidal cells that were recorded during the recording session: either cells that were behaviorally-active in flight, or cells that were active during the two sleep sessions, or both (during sleep sessions, when the bat was not behaviorally-active, there were many sharp-wave-ripples [SWRs] and many spikes). Thus the numbers describing CA1 putative pyramidal cells include also cells that participated in SWRs but were not active during behavior.

‡ We regarded a cell as behaviorally-active if at least in one of the flight directions the spike count during flight met the minimal-spikes threshold criterion (see Materials and Methods). Note that the lower fraction of behaviorally-active cells in earlier days of recording (dataset 3: 67% [141/209] versus dataset 1: 100% [235/235]) could arise from: (i) smaller environment size (130 m versus 200 m); (ii) fewer flight epochs in the first days of exposure to the environment (dataset 3); and (iii) genuinely less spikes during the first explorations.

Finally, we note that the numbers of cells reported here are the numbers of *cells*, not numbers of cells × directions: For example, in dataset 1, there were a total of 235 cells, and many of them had significant place tuning in *both* flight directions.



## Supplementary References

1. M. M. Yartsev, M. P. Witter, N. Ulanovsky, *Nature* **479**, 103-107 (2011).
2. M. M. Yartsev, N. Ulanovsky, *Science* **340**, 367-372 (2013).
3. A. Finkelstein *et al.*, *Nature* **517**, 159-164 (2015).
4. M. Geva-Sagiv, S. Romani, L. Las, N. Ulanovsky, *Nat. Neurosci.* **19**, 952-958 (2016).
5. A. Tuval, L. Las, Y. Shilo-Benjamini, *Lab. Anim.* **52**, 515-525 (2018).
6. A. Sarel, A. Finkelstein, L. Las, N. Ulanovsky, *Science* **355**, 176-180 (2017).
7. W. E. Skaggs, B. L. McNaughton, M. A. Wilson, E. J. Markus, in *Adv. Neural Inf. Proc. Syst.* 5, S. J. Hanson, J. D. Cowan, C. L. Giles, Eds. (Morgan Kaufman, 1993), pp. 1030-1037.
8. W. E. Skaggs, B. L. McNaughton, M. A. Wilson, C. A. Barnes, *Hippocampus* **6**, 149-172 (1996).
9. N. Ulanovsky, C. F. Moss, *Nat. Neurosci.* **10**, 224-233 (2007).
10. R. Eilam-Altstädter, L. Las, M. P. Witter, N. Ulanovsky, *Stereotaxic Brain Atlas of the Egyptian Fruit Bat* (Elsevier - Academic Press, 2021, in press).
11. K. B. Kjelstrup *et al.*, *Science* **321**, 140-143 (2008).
12. P. D. Rich, H. P. Liaw, A. K. Lee, *Science* **345**, 814-817 (2014).
13. M. Geva-Sagiv, L. Las, Y. Yovel, N. Ulanovsky, *Nat. Rev. Neurosci.* **16**, 94-108 (2015).
14. A. P. Georgopoulos, A. B. Schwartz, R. E. Kettner, *Science* **233**, 1416-1419 (1986).
15. H. S. Seung, H. Sompolinsky, *Proc. Natl. Acad. Sci. USA* **90**, 10749-10753 (1993).
16. S. Hallermann, C. P. de Kock, G. J. Stuart, M. H. Kole, *Nat. Neurosci.* **15**, 1007-1014 (2012).
17. M. Tsodyks, T. Sejnowski, *Int. J. Neural Syst.* **6**, 81-86 (1995).
18. F. P. Battaglia, A. Treves, *Phys. Rev. E* **58**, 7738-7753 (1998).
19. D. Hansel, H. Sompolinsky, in *Methods in Neuronal Modeling: From Ions to Networks*, C. Koch, I. Segev, Eds. (MIT Press, 1998), pp. 499-567.
20. A. Samsonovich, B. L. McNaughton, *J. Neurosci.* **17**, 5900-5920 (1997).
21. L. Kang, V. Balasubramanian, *eLife* **8**, e46687 (2019).
22. S. Sreenivasan, I. Fiete, *Nat. Neurosci.* **14**, 1330-1337 (2011).
23. K. Yoon, S. Lewallen, A. A. Kinkhabwala, D. W. Tank, I. R. Fiete, *Neuron* **89**, 1086-1099 (2016).
24. H. Stensola *et al.*, *Nature* **492**, 72-78 (2012).
25. D. Zipser, *Behav. Neurosci.* **99**, 1006-1018 (1985).
26. J. O'Keefe, N. Burgess, *Nature* **381**, 425-428 (1996).
27. M. Tsodyks, *Hippocampus* **9**, 481-489 (1999).
28. T. Hartley, N. Burgess, C. Lever, F. Cacucci, J. O'Keefe, *Hippocampus* **10**, 369-379 (2000).
29. T. Strösslín, D. Sheynikhovich, R. Chavarriaga, W. Gerstner, *Neural Netw.* **18**, 1125-1140 (2005).

30. J. J. Knierim, K. Zhang, *Annu. Rev. Neurosci.* **35**, 267-285 (2012).
31. R. Ben-Yishai, R. L. Bar-Or, H. Sompolinsky, *Proc. Natl. Acad. Sci. USA* **92**, 3844-3848 (1995).
32. A. Compte, N. Brunel, P. S. Goldman-Rakic, X. J. Wang, *Cereb. Cortex* **10**, 910-923 (2000).
33. K. Wimmer, D. Q. Nykamp, C. Constantinidis, A. Compte, *Nat. Neurosci.* **17**, 431-439 (2014).
34. D. Hansel, G. Mato, *J. Neurosci.* **33**, 133-149 (2013).
35. M. Y. Yim, L. A. Sadun, I. R. Fiete, T. Taillefumier, *bioRxiv*, 2019.12.19.881458 (2019).
36. H. Davoudi, D. J. Foster, *Nat. Neurosci.* **22**, 337-342 (2019).
37. S. Leutgeb, J. K. Leutgeb, A. Treves, M.-B. Moser, E. I. Moser, *Science* **305**, 1295-1298 (2004).
38. A. Treves, *Hippocampus* **14**, 539-556 (2004).
39. I. Lee, D. Yoganarasimha, G. Rao, J. J. Knierim, *Nature* **430**, 456-459 (2004).
40. K. Mizuseki, K. Diba, E. Pastalkova, G. Buzsáki, *Nat. Neurosci.* **14**, 1174-1181 (2011).
41. G. Buzsáki, K. Mizuseki, *Nat. Rev. Neurosci.* **15**, 264-278 (2014).
42. N. Schmitzer-Torbert, J. Jackson, D. Henze, K. Harris, A. D. Redish, *Neuroscience* **131**, 1-11 (2005).